Facile Synthesis Approaches for High Li^+ ion Conducting Garnet Structures

by

Pavan Pramod Badami

A Dissertation Presented in Partial Fulfillment
of the Requirements for the Degree
Doctor of Philosophy

Approved August 2021 by the
Graduate Supervisory Committee:

Arunachala Mada Kannan, Co-Chair
Candace Chan, Co-Chair
Kenan Song

ARIZONA STATE UNIVERSITY

December 2021

ABSTRACT

The current Li-ion batteries with organic liquid electrolytes are limited by their safety and energy density. Therefore, ceramic electrolytes are proposed in developing next-generation, energy-dense Li-metal batteries by replacing organic liquid electrolytes to improve safety and performance. Among numerous ceramic Li-ion conductors, garnet-based solid electrolyte c-$Li_7La_3Zr_2O_{12}$ (c-LLZO) is considered one of the most promising candidates to enable Li metal batteries due to its high ionic conductivity, chemical stability, and wide electrochemical stability window against Li metal. However, synthesis and processing of c-LLZO through conventional solid-sate reaction methods requires long periods of calcination (> 6 h) at high reaction temperatures (> 1000 °C). The need for high reaction temperature results to attain cubic-LLZO phase results in large aggerated LLZO particles and causes Li-loss from the garnet structure, making them unfavorable to process further as bulk pellets or thin films. To overcome processing challenges with solid-state reaction method, two novel facile synthesis approaches molten salt (flux growth method), and solution combustion are employed to produce submicron sized LLZO powders at low reaction temperatures (< 1000 °C) in a short time. In the first case, molten salt synthesis method with LiCl-KCl eutectic mixture is employed to produce sub-micron sized Ta-doped LLZO (LLZTO) powders at low temperatures (900 °C, 4 h). In addition, a detailed investigation on effect of sintering medium and sintering additives on the structural, microstructural, chemical, and Li-ion transport behavior of the LLZTO pellets are investigated. Sintered LLZTO pellets prepared using molten salt synthesis route exhibited high Li-ion conductivity up to 0.6 mS cm^{-1} and high relative density (> 95 %) using Pt-crucible. In the second case, a facile solution-combustion technique using an amide-based fuel source CH_6N_4O is utilized to produce submicron-sized Al-doped LLZO (Al-LLZO) powders at low reaction temperatures 600-800 °C in a short duration of 4 h. In addition, effect of fuel to oxidizer ratio on phase purity, particle growth size, and formation mechanism of conductive Al-LLZO are reported and discussed. The Al-LLZO pellets sintered at 1100 °C/ 6 h exhibited high Li-ion conductivity up to 0.45 mS cm^{-1} with relative densities (> 90 %).

DEDICATION

This work is dedicated to my parents Pramod Badami and Mamata Badami, for their unconditional love, sacrifices, support, and encouragement, which allowed me to pursue education in the United States without worrying about family responsibilities.

ACKNOWLEDGEMENTS

To begin with, I want to thank my advisor, Professor A. M. Kannan, for allowing me to carry M.S. and Ph.D. research in his lab at Arizona State University. I thank Dr. Kannan for his mentorship, patience, financial support, and non-judgmental attitude, which allowed me to conduct Ph.D. research without any peer stress. I also thank him, for giving me free hands to work and collaborate with other labs. It’s been a great pleasure to have known Prof. Kannan and work with him for the past seven years. I would also like to thank Mrs. Latha Kannan for her encouragement, hospitality, and efforts in hosting myriad lunches and dinners over the weekends at their home, despite her busy work schedule making us feel close to home. Finally, I wish Dr. Kannan's family success, happiness, and good health in the coming years.

Special thanks to my co-advisor, Professor Candace K. Chan, for introducing me to the synthesis of garnets and graciously accepting to mentor me as her student. I thank Prof. Chan for her guidance, extending her valuable time and resources, showing enormous patience towards me in refining my research abilities. Professor Chan's motivation, enthusiasm, and creative approach to handling research problems are truly unique and inspiring. I wish Prof. Chan all the happiness, a good health, and greater success in her academic and as well research career in the coming years.

I would also like to thank Professor Daniel Rettenwander and Professor Martin R. Wilkening for hosting me at Graz University of Technology, Austria. It’s been a great learning experience working with your groups. I thank Dr. Daniel Rettenwander for his mentorship and support; his hands-on approach working in the lab and breaking down the research problems are genuinely inspirational. I also thank him for introducing me to many

of his distinguished colleagues and providing me with all the required resources, without which my research would have been incomplete.

Thanks to Professor Ramaswamy Murugan, Pondicherry University, India, for insightful discussions and inputs on processing Li stuffed garnets.

Thank you, Professor Kenan Song, for being on my committee, for your valuable inputs and discussions. I wish Prof. Song great success at Arizona State University.

Thanks to Dr. Carole Mars and The Sustainability Consortium, AZ, for the financial support during my Ph.D. program.

I want to thank all present and past lab members (Dr. Jyothi Prakash, Mohit, Umesh, Xuan, and Gregoria) for their friendship and support during my stay at ASU.

I want to thank my batchmates, Mark Weller, Susheel, Sunny, and Saivimal for their friendship and support during my Ph.D. studies. Thanks to Bharat and Ishwar for their friendship and engaging me in hikes during the stressful times.

Thanks to my colleagues - Lukas, Florian, and Stefan, for their friendship and assisting me to gather data for my experiments during my stay in Europe. Thank you, Kiran, Koushik, and Spandana for your friendship and showing me around some beautiful places in Europe.

I want to acknowledge funding from Salt River Project, AZ, and The Polytechnic School-Arizona State University which supported my research work.

TABLE OF CONTENTS

Page

CHAPTER

APPENDIX Page

LIST OF TABLES

Table Page

LIST OF FIGURES

Figure Page

Figure Page

PREFACE

The presented Ph.D. dissertation document consists of a large portion of my published and a limited portion of unpublished research works conducted at Arizona State University, which are reproduced and edited to fit as a well-unified dissertation document. The **Chapters** in this dissertation are arranged as listed below:

Chapter 1 – Introduction to the field of solid-state batteries and promising inorganic solid-electrolytes for all-solid-state batteries.

Chapter 2 – Challenges associated with the garnet-type ($Li_7La_3Zr_2O_{12}$) Li-ion conductors.

Chapter 3 – Introduces the research problem statement, experimental methods, and characterization tools utilized to conduct research work.

Chapter 4 – This chapter consists of synthesizing highly conductive Ta-doped LLZO using novel molten salt (LiCl and KCl eutectic salts) and solid-state reaction method. The results presented in this chapter are published in **ACS *Applied Materials and Interfaces*** - Highly Conductive Garnet-Type Electrolytes: Access to $Li_{6.5}La_3Zr_{1.5}Ta_{0.5}O_{12}$ Prepared by Molten Salt and Solid-State Methods (https://dx.doi.org/10.1021/acsami.0c14056). Most of the contents in **Chapter 4** and **Appendix A** are reproduced from the published work followed by extended work reported in this thesis. The copyright permission attached in **Appendix A**.

Chapter 5 – This chapter presents work on the synthesis of Al-doped LLZO using facile solution- combustion synthesis approach published in **RSC *Materials Advances*** -Facile synthesis of Al-stabilized lithium garnets by a solution-combustion technique for all-solid-state batteries (DOI: 10.1039/D1MA00393C). Most of the contents in **Chapter 5** and **Appendix B** is reproduced from the published work along with additional results. Copyrights permission attached in **Appendix B**.

Chapter 6 – This chapter summarizes and concludes my research work presented in this document. In addition, some preliminary work on optimizing Li metal|| LLZO interface and symmetric cell cycling results and further recommendations are provided to overcome challenges associated with symmetric cell cycling. A list of peer-reviewed articles based on my contribution during Ph.D. studies are listed in **Appendix C**.

1.0 INTRODUCTION AND BACKGROUD

1.1 Lithium-Ion Batteries

Climate change is one of the most pressing issues to be solved. It requires collective global efforts to limit global temperature rise to 1.5 °C above pre-industrial levels by controlling emissions of greenhouse gases (GHGs).[1] CO_2 emission is the dominating source of global warming caused by burning fossil fuels to power homes and industries. Moreover, ground transportation sector accounts for about 29 % of the total U.S. GHGs, making them one the largest contributor to GHGs emissions. To limit the rise in global temperatures and GHGs, requires a rapid transition towards the electrification of vehicles.[2] The penetration rate of electric vehicles (EVs) in the market primarily depends on cost and technological advancements made in the electrochemical storage systems (ESS), followed by secondary factors such as federal incentives, manufacturing, and availability of charging infrastructures. Among the various ESS, Li-ion batteries (LiBs) offers high energy and power density, making them a robust technological candidate for vehicle electrification.[3]

Sony corporation in 1991 commercialized the first Li-ion batteries consisting of graphite host anode (LiC_6) and metal oxide cathode ($LiCoO_2$), based on the contributions of 2019 chemistry Nobel laureates- Professor John B. Goodenough, Professor M. Stanley Whittingham, and Dr. Akira Yoshino.[4,5] Since then, Li-ion batteries are transforming the transportation, portable electronics, and grid storage sectors. However, the present LiBs offer energy density ~ 250 Wh L^{-1} (refer to **Figure 1.1** (top)) are not expected to meet the energy density requirement goal set by the U.S. Department of Energy (DOE), *i.e.*, electric vehicle pack level goal of 500 Wh L^{-1}. To attain high pack level energy density requires replacing graphite anode with a Li metal anode; this results in 50 % increase in energy density and 35% increase in the specific capacity of the batteries.[6] Li metal anode, when coupled with the organic liquid electrolyte, poses a high risk of thermal runaway and explosion caused by short-circuits due to Li dendrites growths. One of the proposed strategies to enable Li-metal anode with increased safety includes use of inorganic solid electrolyte (S.E.) (**Figure 1.1)**.

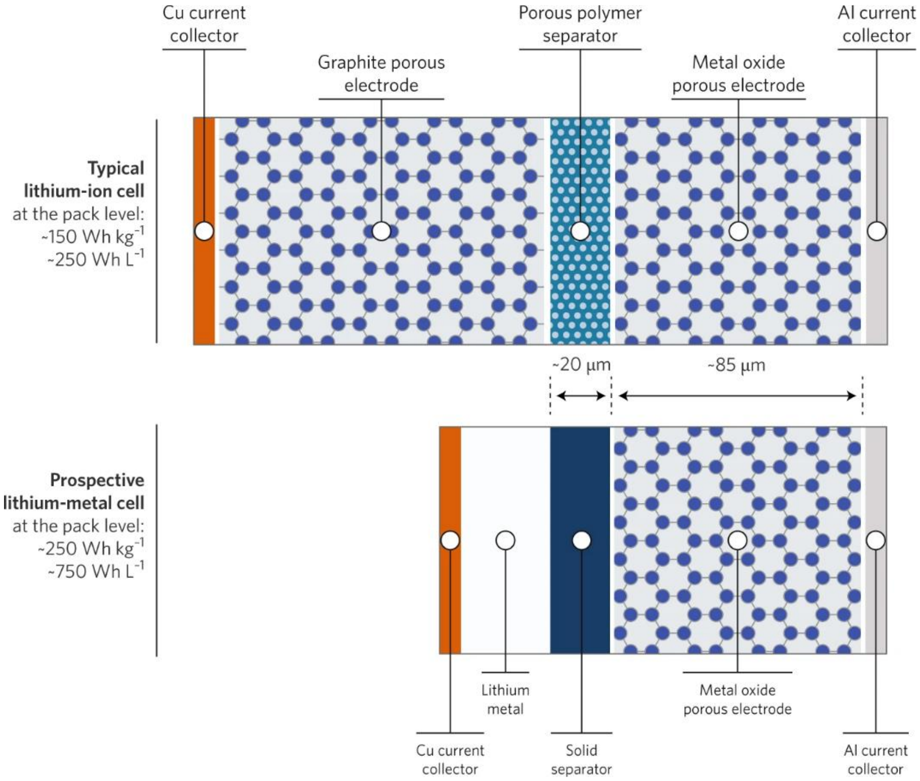

Figure 1. 1. A schematic representation of current LiBs (top) and all-solid-state batteries (bottom). The reduction in the form factor is observed by replacing graphite anode with Li metal anode using a solid electrolyte; leads to a 2x increase in specific energy and a 3x increase in energy density compared to LiBs. Reprinted from Ref.[6]

A compatible inorganic S.E. for Li metal anode has been investigated since the 1970s. Still, only a few qualify as promising candidates based on their chemical and structural compatibility with Li metal anode.[7] The following section introduces readers to promising the family of promising solid-ion conductors with desired properties to enable Li metal batteries.

1.2 Inorganic Solid Electrolytes for All-Solid-State Batteries

Inorganic solid electrolytes should meet several key properties to be employed in all-solid-state batteries (ASSBs):

1. Li-ion conductivity of SE should be comparable to that of organic liquid electrolytes
2. Negligible electronic conductivity
3. Lithium transference number (close to unity)
4. High electrochemical stability window > 5 V vs. Li metal
5. Good thermal and mechanical stability
6. Similar thermal expansion coefficient to those of metal oxide electrode materials
7. Inexpensive processing and manufacturing cost
8. Low charge transfer resistance at the electrode and electrolyte interface

A brief review on two potential classes of inorganic solid electrolytes (sulfides and oxides) meeting some of the aforementioned requirements are discussed in the following section.

1.2.1 Sulfide-Based Li-ion Conductors

1.2.1.1 Sulfide Glasses

The Li_2S-P_2S_5 based glass and glass-ceramic electrolytes possessing high Li^+ ion conductivity (in the order of 10^{-3} S cm^{-1}) at room temperature, with low activation energy, have attracted significant attention as promising solid electrolytes for ASSBs.[8] While, thio-LISICON electrolytes $Li_{4-x}Ge_{1-x}P_xS_4$ belong to sulfide family exhibits much higher ionic conductivities in 10^{-2} S cm^{-1} at room temperature compared to sulfide glasses.[9,10] The most notable composition of the LGPS family is $Li_{10}GeP_2S_{12}$, which shows the highest ionic conductivity of 12 mS cm^{-1} at room temperatures.[11] However, some drawbacks with LGPS based electrolytes include use of expensive precursors like Ge which have low compatibility with Li metal.[12] While, Murayama, and Bron successfully replaced germanium in $Li_{10}GeP_2S_{12}$ (LGPS) with Silicon (Si) and Tin (Sn), maintaining the same crystal structure but at the cost of low ionic conductivity.[13] Later, Kato *et al.* prepared a Li^+ ion conductor with a nominal composition of $Li_{9.54}Si_{1.74}P_{1.44}S_{11.7}Cl_{0.3}$ with a similar design to LGPS with very high ionic conductivity 25 mS cm^{-1} at room temperature.[11] One of the major drawbacks with the processing of sulfide based electrolytes involves release of H_2S gas on exposure to air.

1.2.2 Oxide-Based Li-ion Conductors

1.2.2.1 Perovskite-Type

The perovskites-type Li^+ ion conductors ($Li_{3x}La_{2/3-x}\square_{1/3-2x}TiO_3$, $0<x<0.16$, "LLTO," □ represents a vacancy) with a general formula of ABO_3 has a three-dimensional crystal structure consisting of sharing BO_6 octahedra, and the A ions reside in the middle of the cubic cell. In general, A sites are occupied by La, Li, and vacancies, while B sites are occupied by Ti atoms as seen in **Figure 1.2**. LLTO has attracted great attention in the last two decades because of its high Li^+ ion conducting values (> 10^{-3}S.cm^{-1}) at room temperatures, high modulus of elasticity (200 GPa), negligible electronic conductivity, and a wide electrochemical voltage window up to 8 V.[14] LLTO exhibits several phases: cubic, tetragonal, orthorhombic, and hexagonal depending on the lattice vacancies (□), Li contents, and synthesis conditions. The orthorhombic and hexagonal phases are only observed for $x < 0.06$ and $x = 0.167$, while tetragonal and cubic phase are observed for $0.06 < x < 0.167$. A detailed review on the properties of LLTO can be found elsewhere. [15,16] The main drawback with LLTOs are they readily get reduced from Ti^{4+} to Ti^{3+} in contact with metallic lithium, and a stable interaction of lithium metal and LLTO occurs at 1.7-1.8 V showing low electrolyte stability window making them not compatible.[17,18]

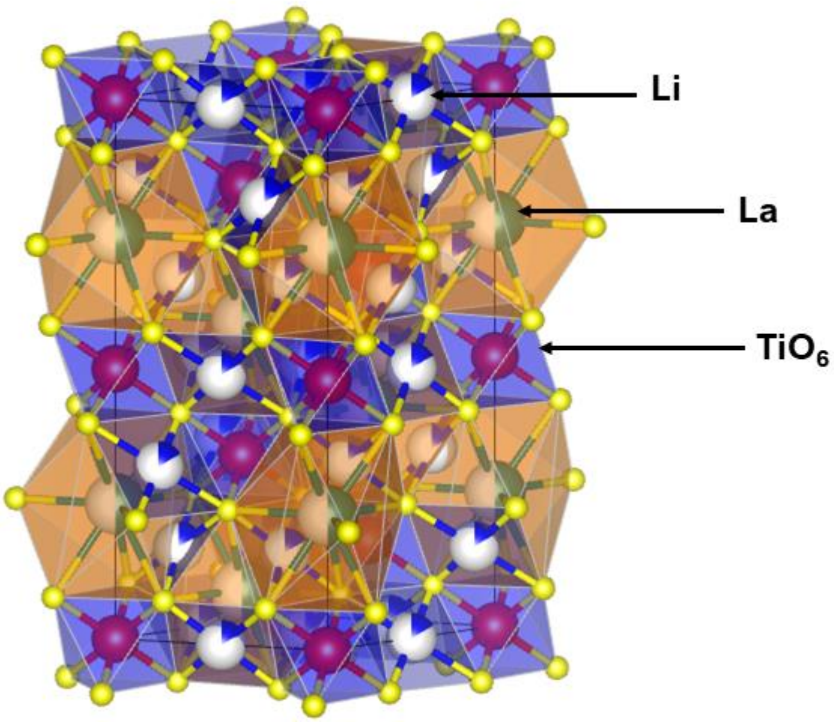

Figure 1. 2. A schematic representation of 3D LLTO crystal structure (perovskite), wherein Li, La and vacancies atoms occupy A-sites, while Ti-O atoms forms octahedra.

1.2.2.2 Anti-Perovskite-Type

Zhao *et al*. showed an inversion of perovskite (cubic, $Pm\overline{3}m$) structure to form anti-perovskites (A_3OX, A= Li, Na, and X= Cl^-, Br^-, I^-) where in X^- ions occupy the corner side of the cube, O^{2-} ions occupy the body-centered site of the cube, and Li^+ ions form octahedra around the oxygen as seen in **Figure 1.3**.[19] These solid electrolytes exhibit ionic conductivities greater than > 10^{-3} S cm^{-1} at room temperatures with activation energies in the range of 0.2 - 0.3 eV. The highest Li-ion conductivity (10^{-2} S cm^{-1}) is recorded for the composition $Cl_{0.5}Br_{0.5}OLi_3$ with extremely low electronic conductivity and a wide electrochemical stability window of greater than 5 V, making them highly desirable solid electrolyte for the practical applications.[19] Recently, fluorine-doped anti-perovskite electrolyte (Li_2-(O.H.$)_{1-x}F_xCl$) with cubic structure was found to offer exceptionally high electrochemical stability up to 9 V against Li metal.[20] Removal of H^+ ions was found to be beneficial in forming amorphous glassy phase displaying ionic conductivity higher than 10^{-2} S cm^{-1} as reported by Braga *et al.*[21], however these electrolytes are extremely hygroscopic in nature leading to inferior ionic conductivity.

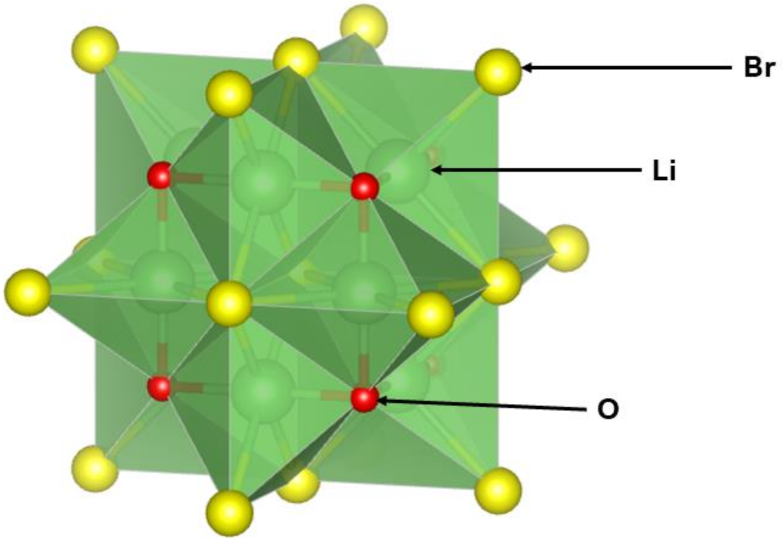

Figure 1. 3. A schematic representation of anti-perovskite structure consisting of Br atoms at the corner and $Li^{-}O$ atoms forming octahedral.

1.2.2.3 NASICON-Type

NASICON having a crystal structure $AM_2(PO_4)_3$ (space group: rhombohedral $R\bar{3}C$) with A site is occupied by Li and M site occupied by Ge, Ti, Zr, or Hf elements are widely studied as Li-ion conductors.[22,23] In this structure, two types of polyhedral, $[MO_6]$ octahedra and $[PO_4]$ tetrahedra are linked via corners to form the $[M_2(PO_{4)3}]^-$ rigid framework (refer **Figure 1.4**). In particular, NASICON type solid electrolytes with trivalent substitution of Al and Ge, ($Li_{1.3}Al_{0.3}Ti_{1.7}(PO_4)_3$, LATP) and ($Li_{1+x}Al_xGe_{2-x}(PO_4)_3$, LAGP) is found to enhance ionic conductivity at room temperatures and offer high thermal stability.[24,25,26] Although, these materials show high ionic conductivity, good moisture stability, and high modulus of elasticity 115 -125 GPa but facile reduction of Ti^{4+} ions at potentials below 2.5 V versus (Li^+/Li) prevent them from being utilized with Li metal anode.[18]

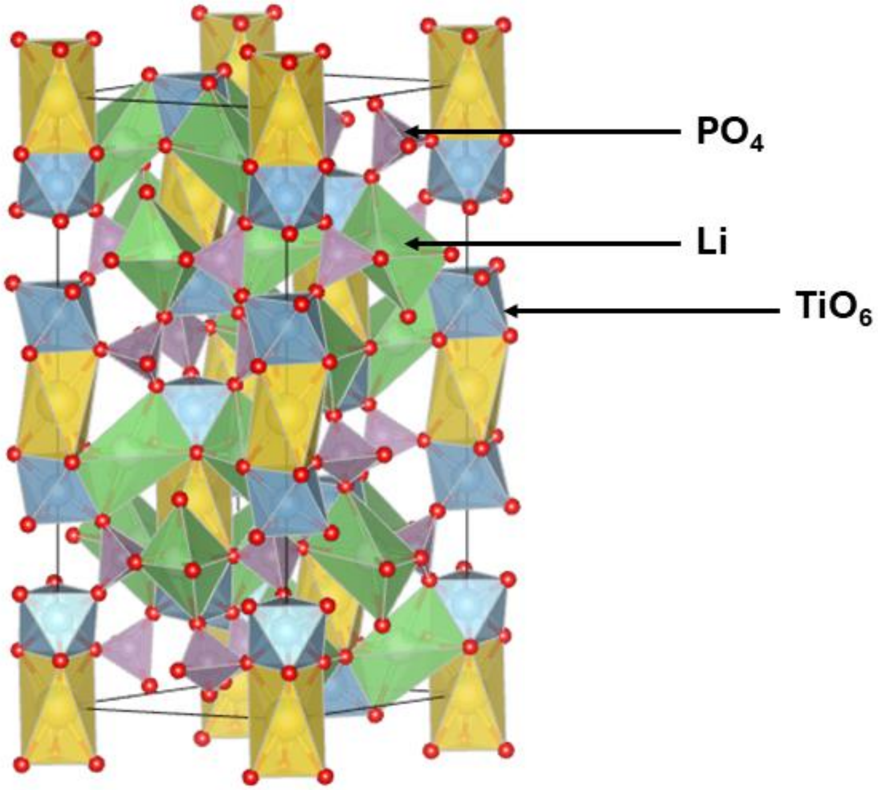

Figure 1. 4. A three-dimensional representation of NASICON-type structure (LATP) belonging to rhombohedral group, Li^+ ions are located between two TiO_6 octahedra.

1.2.2.4 Garnet-Type

Li-ion garnet conductors with the general formula ($Li_5La_3M_2O_{12}$, M= Nb, Ta) were first developed by Hyooma *et al*.[27] Later, Thangadurai *et al.* investigated ($Li_5La_3M_2O_{12}$, M= Nb, Ta) and reported ionic conductivity 10^{-6} S cm^{-1} at room temperature.[28] Soon after that, Murugan and co-workers demonstrated fast Li^+ ions conductions in garnet (10^{-4} S cm^{-1}), having a nominal composition of ($Li_7La_3Zr_2O_{12}$, LLZO) with low activation energy (0.3 eV) and a wide electrochemical stability window.[29] This generated great interest among the scientific community and led to extensive exploration to enable Li metal batteries with garnet-type solid electrolytes. A few years later, Awaka *et al.* discovered that LLZO exhibits two stable phases, namely a tetragonal phase (t-LLZO, sg: $I4_1/acd$) and a cubic phase (c-LLZO, sg: $Ia\bar{3}d$).[30] The tetragonal phase has Li^+ ion conductivity (10^{-6} S cm^{-1}) value, two orders of magnitude lower compared to its cubic phase (10^{-4} S cm^{-1}).[29] The tetragonal phase LLZO is composed of dodecahedral (LaO_8) and octahedral (ZrO_6), as seen in **Figure 1.5a**. The Li atoms occupy tetrahedral (8*a*), distorted octahedral (16*f* and 32*g)* interstitial sites. In contrast, the cubic phase LLZO structure (**Figure 1.5b)** is also composed of dodecahedral (LaO_8) and octahedral (ZrO_6) but the Li^+ ions occupy distorted octahedral sites (48g/ 96h) rather than confining only in the tetrahedral sites (24*d*) causing disordered three-dimensional network structure with short Li^+-Li^+ distances. High ionic conductivity in the cubic phase LLZO is attributed to the presence of excess Li^+ ions in the octahedral sites (48g/ 96h) and lower occupancy in the tetrahedral sites (*24d*).[7]

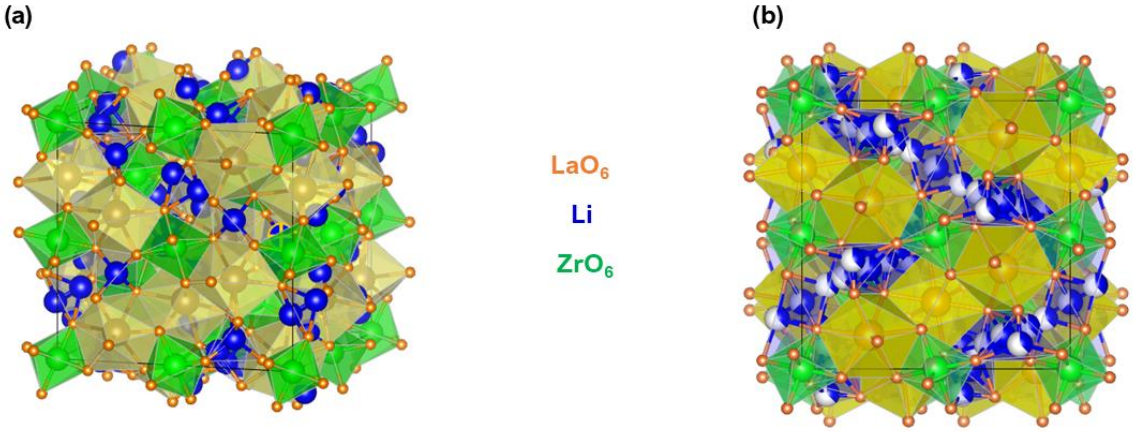

Figure 1. 5. (a) Crystal structure of tetragonal LLZO, Li atoms completely (blue spots) occupy the tetrahedral and distorted octahedral sites. (b) Crystal structure of cubic LLZO, Li atoms partially (blue-white spots) occupy tetrahedral sites and octahedral sites.

The c-LLZO are only stable at temperatures (above 700 °C) and transforms to a tetragonal phase at room temperatures. The first room-temperature stabilization of c-LLZO was carried by Al^{3+} substitution on the Li site; Al^{3+} was unintentionally incorporated into the garnet during the sintering process (from the Al_2O_3 crucible) resulting in Al-doped LLZO with chemical composition of $Li_{7-3x}Al_xLa_3Zr_2O_{12}$.[31] Later, several other aliovalent cations such as Ga^{3+} substitutions on Li and Ta^{5+}, W^{6+}, Nb^{5+} on La sites were extensively explored to stabilize conductive c-LLZO phase at room temperature and improve its ionic conductivity.[31,32,33,34,35,36] Among all the aliovalent dopants, Al and Ta doped-LLZO, are of great interest due to their wide electrochemical stability with the Li metal and high Li^+ ions conducting transport properties.[37] Furthermore, LLZO has sufficient shear modulus (60 GPa) to suppress Li dendrite growth, satisfying Monroe *et al.*[38] mathematical model preventing Li metal dendrite growth through LLZO.

Therefore, this dissertation focuses on the study of Al and Ta-doped LLZO garnet-type solid electrolytes for all-solid-state Li metal batteries. **Chapter** 2.0 of this dissertation introduces readers to the challenges associated with the LLZO electrolytes which are essential to be addressed before LLZO can be implemented with Li metal anode and manufacture all solid-state batteries at a commercial level.

2. 0 CHALLENGES WITH GARNET-TYPE SOLID ELECTROLYTES

Although LLZO is considered as one of the promising S.E. for the development of Li metal batteries, but there are several challenges which needs to be addressed (see **Figure 2.1**). For example, synthesizing LLZO typically requires high reaction temperatures (> 1000 °C) and long duration of annealing (> 10 h), such harsh synthesis conditions can lead to severe Li evaporation from the garnet framework and making them unfavorable to process further. Moreover, energy intensive milling steps required to process LLZO makes manufacturing cost intensive.[39,40] In addition, LLZO are prone to exchange Li^+/H^+ ions exchange in presence of moisture which affect total Li^+ conductivity and forms passivation layers causing poor interface contact between Li metal and LLZO surface.[41] Poor interface contacts between the cathode and anode cause poor cyclability and failure of cells at low current densities.[42]

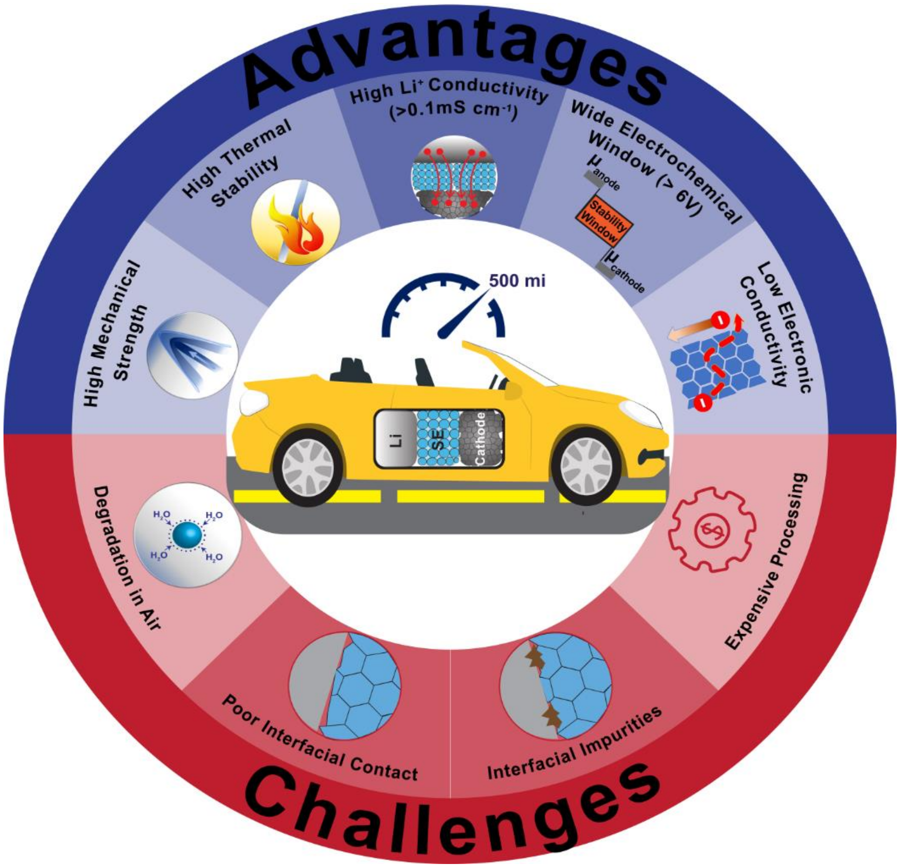

Figure 2. 1. An overview of advantages and challenges of garnet type solid electrolytes.

2.1 Processing Challenges

2.1.1 Solid-State Reaction Method

Synthesis of LLZO using solid-state reaction method (see **Figure 2.2 a**) typically requires use of carbonates and oxides-based precursors, followed by energy intensive grinding and milling of precursor powders to reduce the particle size and provide good intimate contact to drive the diffusion-reaction at high temperatures (above > 1000 ºC). In many cases, the slow kinetics of the reaction can cause impurity phases due to incomplete reaction and along with irregularly shaped LLZO particles. Often, additional milling and calcination steps are required to eliminate impurity phases or reduce the particle size of the final powder for better sinterability.[34,43,44] In some cases, the high temperature reaction is carried out by pressing pellets (consisting of starting precursors materials), followed by multiple calcination and grinding steps until desired conductive phase is attained.[45] Presence of undesired phases and inhomogeneity in the chemical composition due to slow kinetics of the reaction can lead to non-uniform Li^+ ions transport across the bulk and grain boundaries of the pellet, which can be the root cause for the growth of Li dendrites during cycling with Li metal.[46] A few recent studies showed reduction in the processing temperatures of LLZO using solid state reaction method (< 1000 ºC) by employing multiple milling utilizing organic-based solvents like ethanol, 2-propanol, however such solvents are expensive for large scale production.[43,47] Huang *et al.* demonstrated the synthesis of Ta-doped LLZO using water-based solvent; to prevent the Li^+/H^+ exchange, LiOH was incorporated into the water based solvent. Despite using an environmentally benign solvent to prepare Ta-doped LLZO, the final conductivity of the LLZO pellets were slightly inferior due to protonation.[48] In conclusion, there are significant drawbacks with the solid-state reaction route to produce LLZO. Therefore, an alternative synthesis approach to prepare nano-sized LLZO powders garnets using low-temperature facile route is of great importance.

2.1.2 Wet-Chemical Syntheses

Sol-gel technique has emerged to be an attractive route to synthesize inorganic oxides in wet-chemical syntheses approach. Sol-gel approach offers several advantages in preparing ternary or quaternary oxides using chemically homogenous metalorganic precursors and allowing atomic-level mixing of reagents in solvents to produce desired oxides at low temperature with significant control over the particle size. In brief, reactions in sol-gel synthesis (for a schematic representation of the process, see **Figure 2.2b**) proceeds via the following vital steps (a) hydrolysis, (b) polymerization, (c) gelation, and (d) drying and dehydration.[49,50] Sakomoto *et al.* synthesized highly conductive LLZO utilizing nitrate/alkoxide-based precursors with acetic acid as a chelator to form highly interconnected nano-sized gels with width < 10 nm. Using this approach, LLZO was synthesized at low temperatures (600-800 °C) but requires a long duration of ageing of gel and multiple calcination steps.[51]. Another side-branch of the sol-gel process is the chemical co-precipitation method, commonly involves dissolving nitrate-based precursors in a solvent, followed by drop-wise addition of precipitating agent until reaching the desired pH to stabilize the solution. For example, Shao and co-workers utilized co-precipitation route to synthesize LLZO, but prepared powders calcined at 800 °C showed a tetragonal phase and required additional calcination step high temperature (> 1000 °C) to attain cubic phase LLZO.[52]

In 1967, M. Pechini developed an innovative process to overcome disadvantages (expensive precursors and eliminating fast hydrolysis rate) associated with the traditional sol-gel process.[53] Pechini process involves utilizing chelating ligands to form homogenous solution of metal/citrate complexes, followed by conversion into a polymer network to entrap the metal ions, thereby prolonging thermal decomposition of the organic matrix, allowing controlled growth of ceramic oxides. Typically, metal salts are dissolved in water along with citric acid and ethylene glycol to form a homogenous precursor solution. The heating of the solution aids in poly-esterification network between the citric acid and ethylene glycol. The polymer network is later heated to combust the organic matrix and form desired ceramic product. Several more variations to this type of synthesis approach are available in the literature, while only abbreviated reports are mentioned here. Jin *et al.* were able to stabilize Al-doped LLZO at low reaction temperatures and in a relatively short duration 900 ºC, 6 h using citric acid and ethylene glycol as complexing agents.[54] Slater's group were able to synthesize Al-LLZO at much lower temperatures (~700 ºC) using agar-based biopolymer and nitrate-based precursors.[55]

The wet-solution synthesis technique can be expanded to a solution-based combustion method by incorporating organic-based fuels into the precursor solution. Fuel also behaves as a chelator, aids in attaining fine nanoparticles on pyrolysis of gel in the air. Typical synthesis requires metal nitrate salts mixed with citric acid, later resulting solution is heated to form a viscous gel and gel later auto ignites on exposure to heat (300-350 ºC) fluffy powders which can be in the amorphous or crystalline state. Amorphous powders can be converted to the desired crystalline product on annealing further. An exhaustive review on solution-combustion synthesis on the selection of fuel, fuel to oxidizer ratio, and other synthesis parameters can be found in here.[56,57] Dhivya *et al.* synthesized Al-doped LLZO using a glycine-nitrate mixture, but the desired conductive cubic was formed on calcining the gel above > 900 ºC for 12 h.[58] Afyon *et.al* were successful in synthesizing t-LLZO at low temperatures 600 ºC , transformation from t-LLZO to c-LLZO phase was carried out using Ga_2O_3 and annealing mixture at 600 ºC for 12 h. Weller *et al.* conducted synthesis of Ta-doped LLZO using a nonaqueous polymer combustion route using acetonate based precursors with polyvinylpyrrolidone as polymer matrix and fuel to form a combustible mixture. Although cubic phase Ta-doped LLZO was attained at 700 ºC on calcining for 4 h by employing expensive solvents and precursors.[59] **Chapter 5** of this dissertation introduce a facile synthesis of Al and Ga-doped LLZO using inexpensive precursors and water-soluble fuel, where in cubic-phase LLZO can be attained between 600 -800 °C in a short duration of 4 h.[60,61]

2.1.3 Molten Salt Syntheses

A flux melt (molten salt) method is an exciting technique to synthesize binary, ternary, and complex oxides and has drawn a significant amount of attention to synthesizing at low reaction temperatures. The flux melt method uses molten salt as a solvent medium to facilitate crystal growth with improved phase purity and particle homogeneity. The flux melt route uses inorganic salts, which are heated above their melting temperature to dissolve inorganic reagents and allow crystallization/growth. Crystallization in a molten flux media can be described in four steps i) reagent dissolution, ii) reactants diffusion through the molten fluxes, iii) nucleation, and iv) crystal growth. The flux solvent approach facilities the growth of the crystal below the melting points of the reagents.[62] A schematic representation of the molten salt process is shown in **Figure 2.2 c**.

Reddy *et al*. synthesized Ta-doped LLZO using a $LiNO_3$ and LiCl flux media with a low melting point of 280 ºC.[63] However, the synthesized powders (beyond 700 °C) showed high agglomeration and poor crystallinity, possibly due to evaporation of the flux media as $LiNO_3$, which decomposes at 600 ºC. Moreover, sintered pellets showed low ionic conductivity, possibly due to the washing step inducing protonation, causing low ionic conductivity (10^{-6} S cm). [64,65] Later, Weller *et al.* demonstrated the synthesis of Al and Ga-doped LLZO using chloride mixtures (LiCl and KCl). LLZO synthesized using chloride-based flux showed good ionic conductivity (~0.3 mS cm^{-1}) and but had slightly lower relative density (< 90 %), possibly due to some degree of protonation. This dissertation presents a detailed study on the preparation of highly dense (> 90 %) and conductive Ta-LLZO using a novel molten salt method with LiCl and KCl eutectic and solid-state reaction using pressure less sintering technique discussed in **Chapter 4.**

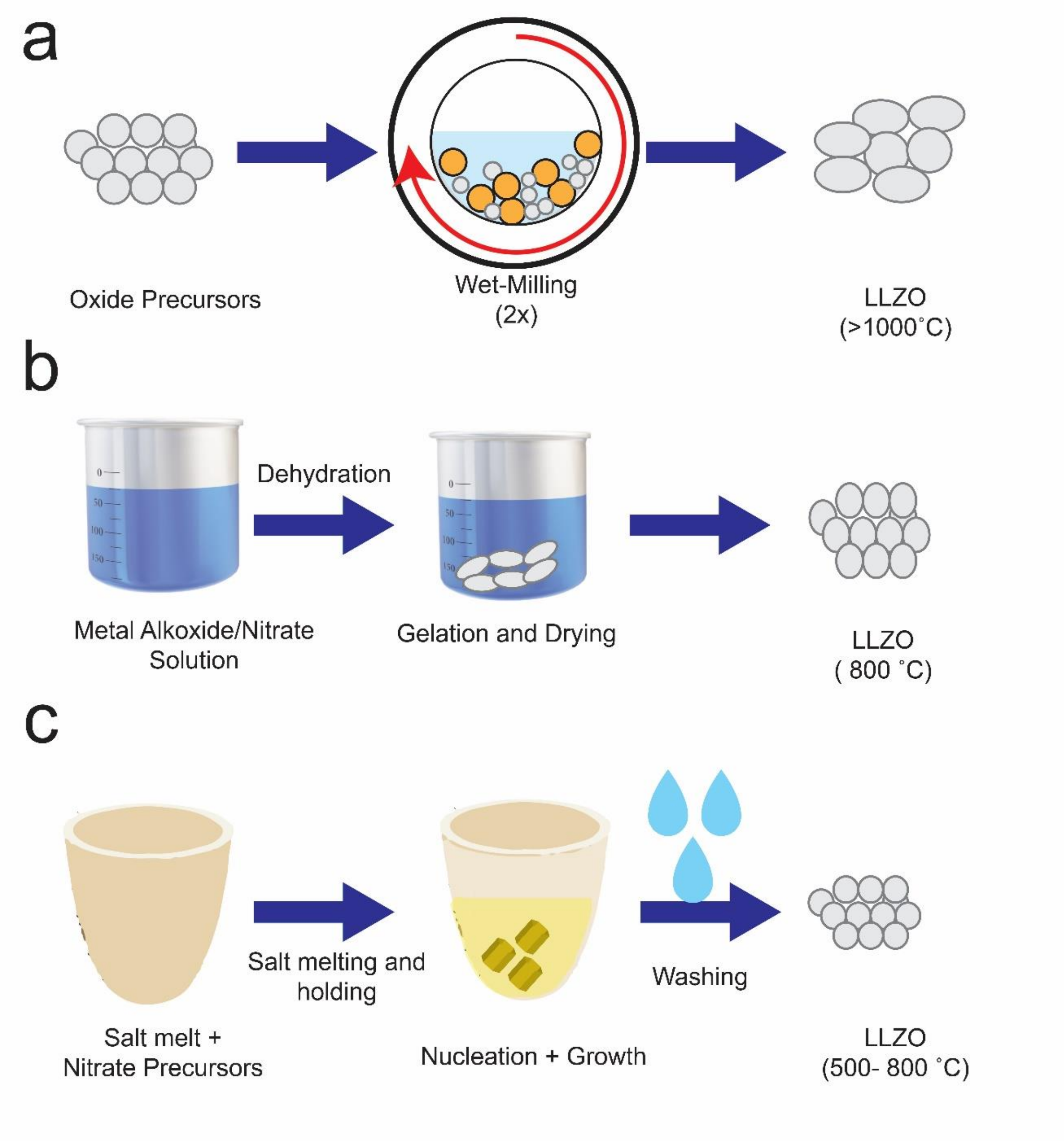

Figure 2. 2. Schematic representation of syntheses of LLZO using (a) solid-state reaction (b) wet-chemical method and (c) molten salt methods.

2.2 Protonation in LLZO

LLZO on exposure to air or any aqueous solutions, undergoes a spontaneous Li^+/ H^+ ions exchange reaction, followed by the formation of LiOH and Li_2CO_3 passivation layers.[64,66] The proton exchange reaction in LLZO induces the degradation of bulk ionic conductivity and further leads to poor sinterability of the pellets. On protonation, LLZO retains its original cubic structure but undergoes lattice expansion due to the replacement of strong Li-O bonds by weak hydrogen bonds O-H-O.[67] The passivation layers (LiOH and Li_2CO_3) formed on the garnet surface are also found to affect interfacial properties causing increase in the interface resistance with Li metal and leading to non-homogeneous lithium electrodeposition during cell cycling, causing Li shorts.[68]

Several studies in the past have focused to understand site occupancy of Li^+ and H^+ ions, structural changes, mobility of H^+ ions in the protonated garnets.[69,70,] Liu *et al.* revealed mobility and lattice occupancy of H^+ ions and Li^+ ions (in acidic medium) of protonated LLZO samples using neutron diffraction and electron spectroscopy techniques. They observed H^+ ions partially occupying 96*h* and 48*g* Li sites and also found that proton exchange up to 60 % did not alter the crystal structure LLZO; however, proton exchange beyond 75 % was found to induce structural change in LLZO, transforming the structure from $Ia\bar{3}d$ to $I\bar{4}3d$.[67] The H^+ ions were found to be immobile only below 400 K but increase in the temperature above 400 K showed strong H^+ ions diffusion affecting the total conductivity of the samples. Similarly, Hiebl *et al*. studied structural changes in single crystal Al-LLZO immersed in H_2O for a period of three years. They observed that occupancy of Li^+ ions in the 96*h* sites was significantly affected, causing low ionic conductivity by the presence of H^+ ions on Li sites. Furthermore, proton diffusion coefficient (D_o (H^+) – 2 x 10^{-17} m^2 s^{-1}) in AL-LLZO was high enough to corrode Li metal anode (100 nm thickness), causing type-II dendrite formation.[71] Reedhammer and co-workers extensively investigated structural changes induced in single crystal and polycrystal Ta-doped LLZO samples for the first time. LLZO samples were subjected to various aqueous environments to understand Li^+/H^+ exchange reactions using X-ray diffraction techniques.[65] They concluded that Li^+/ H^+ exchange preferably occurred at 24*d* sites compared to most commonly observed 96*h* sites, suggesting proton exchange is mainly dependent on the garnet composition and cannot be generalized. Interestingly, H^+ ions diffusion was more dominant at elevated temperatures than compared to room temperatures, concluding that H^+ ions in protonated LLZO can severely affect performance of the batteries.

Proton reversal exchange reaction in LLZO is essential to prevent the harmful effects of H^+ ions in the garnets, which can be mitigated in several different ways. Ma *et al.* carried out a proton exchange reversal reaction by immersing protonated LLZO sample in a 2 M LiOH solution; the Li content in the samples jumped nearly twice the initial value, suggesting an effective proton reversal reaction.[72] Liu *et al.* soaked protonated LLZO in a 5 M $LiNO_3$ at various temperatures and duration and observed proton exchange reversal reaction occurred efficiently at elevated temperatures in a highly basic media. Cheng *et al.* were able to overcome protonation in LLZO by heating the LLZO samples at 250 °C under an inert atmosphere (Ar), decomposing Li_2CO_3 layer to form a rich Li_2O atmosphere.[73] Similarly, Rosen *et al.* demonstrated the impact of proton exchange on ionic conductivity and cycling behavior of the cells taking place at the various levels of the manufacturing process in LLZO and recommended the use of inert atmosphere and reduced exposure to solvent to prevent reproducibility issues.[74]

2.3 Surface Impurity Affecting Interface Resistance in LLZO

The passivation layers such as LiOH and Li_2CO_3 formed on the LLZO surface can lead to poor wettability of Li metal on exposure to air.[75] The LiOH passivation layer formed on the garnet surface readily exchanges of H^+ ions from the air with Li^+ ion of the S.E. (**Equation**.**1**), and further LiOH reacts with atmospheric CO_2 to form Li_2CO_3 (**Equation**.**2**).

$$Li_7La_3Zr_2O_{12} + xH_2O \rightarrow Li_{7-x}La_3Zr_2O_{12-x} + x\ LiOH \qquad \textbf{(1)}$$

$$LiOH + \tfrac{1}{2}\ CO_2 \rightarrow \tfrac{1}{2}\ Li_2CO_3 + \tfrac{1}{2}\ H_2O \qquad \textbf{(2)}$$

Wet-polishing of LLZO pellet surface followed by heat treatment at 500 °C in the Ar atmosphere is found to reduce interfacial resistance between Li metal and LLZO from 400 to 2 $\Omega\ cm^{-2}$ by eliminating passivation layer. [76] Whereas, LLZO surface subjected to dry polishing showed greater tendency to form Li_2CO_3, which is difficult to eliminate completely with heat treatment due to high decomposition temperature of the carbonate.[76] Goodenough *et al*. carried out carbon treatment of LLZTO pellet at 700 °C in Ar atmosphere for 10 hours to decompose Li_2CO_3 layer and improved wettability of the Li metal on LLZO surface. [77] Use of LiF additives was found to improve air stability of LLZO as LiF forms strong ionic bond and its insolubility in water prevent diffusion of moisture and CO_2.[78] Guo *et al.* carried out annealing of LLZO pellets at 900 °C for 24 hours which in turn prevents Li_2CO_3 formation by turning the surface Li deficient.[79] The Li deficient surface was eliminated by mechanical polishing in an inert atmosphere preventing formation of Li_2CO_3 layer. Alternatively, mild-acid treatments of LLZO pellets with HCl was found to effectively eliminate surface carbonate layer decreasing interfacial resistance from 940 to 26 Ώ cm^{-2} without affecting bulk ionic conductivity.[80] Similarly, phosphoric acid [80], oxalic acid [81], and etching with HCl [82] reduced inactive area and promoted good Li wettability and cyclability compared to simple dry polishing technique. On the other hand, Duan *et al.* highlighted that the presence of intrinsic impurity layer on the Li metal surface such as Li_2O can also cause poor Li || LLZO contact.[83] Rub-coating of Li metal surface against LLZO aided in the removal of surface impurity of Li metal resulting in lower resistance of 6.95 Ώ cm^{-2} and improved cycling at high critical current density. Other approaches to minimize interface resistance rely on coating of thin Al_2O_3 on LLZO surface using atomic layer and pulse laser deposition methods, however such approaches are expensive for large scale applications.[84]

Sharafi *et al.* showed a drastic 10-fold drop in the interfacial resistance between Li||LLZO on applying a stack pressure of 350 kPa and cycling cells at elevated temperatures.[85] Interestingly, CCD values significantly increased from 50 to 20,000 μA cm^{-2} on cycling the symmetric cells from 30 to 160 °C, which is attributed to better interfacial contact at high temperatures. Sakamoto and co-workers,[86] also characterized the effect of stack pressure on the potential behavior, critical current density (CCD) values, and decoupled Li stripping and plating mechanism to understand void formation phenomena at the interface. A small change in the interfacial resistance is evident from the flat voltage response observed upon applying high stack pressure on the cell, contrary to the rise in the potential upon reducing stack pressure. To attain high CCD values, need use application of high pressure to stabilize the polarization. For example, measured stack pressure for cycling at 0.1, 0.2, and 0.4 mA cm^{-2} are 0.4, 1.2, and 2.0 MPa, respectively. Increase in the interfacial resistance during the cycling was attributed to formation of voids predominantly during Li stripping. Recently, use of facile interlayers such as graphite, Au, and Li-metal (Sn, Mg) alloys improve interface contact of Li metal with LLZO pellet.[87,42,88,89] Some of following these interlayers are incorporated to understand interface resistance and symmetric cycling of cells which would be discussed in **Chapter** 6.

3.0 RESEARCH OBJECTIVES AND EXPERIMENTAL

Li^+-ion conducting garnets (LLZO) are promising candidates to enable Li metal anode batteries; however, several challenges need to be addressed to enable LLZO as a solid electrolyte in all-solid-state batteries, as discussed in **Chapter 2**. The presented dissertation reports two facile novel synthesis techniques to produce conductive submicron sized LLZO powders at low reaction temperatures. First, **Chapter 4** introduces the molten salt method using chloride mixtures (LiCl and KCl) to produce nanosized unaggregated conductive Ta-doped LLZO powders with a nominal composition $Li_{6.5}La_3Zr_{1.5}Ta_{0.5}O_{12}$ (LLZTO) at low reaction temperatures (~ 800-900 °C). The LLZTO powders prepared using molten salt synthesis routes are characterized extensively compared with the conventional solid-state reaction method. Second, the proton exchange caused by the washing step during molten salt synthesis reaction is effectively reversed by utilizing excess mother powder during the sintering process to prevent poor sinterability and loss in the pellet's ionic conductivity. The effects of sintering medium and additives on sintered pellet's structural, electrochemical, and chemical composition are extensively characterized and reported.

In **Chapter 5**, a novel fuel assisted wet-chemical synthesis technique is employed to produce sub-micron sized Al-LLZO with a nominal composition of $Li_{6.28}Al_{0.24}$

$La_3Zr_2O_{12}$ at low temperatures (600-800 ºC) in a short duration of 4 h; which conventionally requires high reaction temperatures (> 1000 ºC) and a long period of annealing (> 12 h) through solid-state reaction method. The effect of fuel to oxidizer ratio and annealing conditions on the pellet's phase purity, particle size, and ionic conductivity are investigated in detail. Lastly, facile interlayers like graphite and Li_3PO_4 are used to negate high interface resistance between Li metal and LLZO. A galvanostatic cycling test on LLZTO pellets with graphite interlayer was performed to determine the natural critical current densities presented in **Chapter 6**.

3.1 Experimental Methods

3.1.1 Synthesis of Ta-doped LLZO using Solid State Reaction Method

Synthesis of cubic phase Ta-doped LLZO with a nominal composition of $Li_{6.5}La_3Zr_{1.5}Ta_{0.5}O_{12}$ was carried out as mentioned below. First, stoichiometric amounts of LiOH (Alfa Aesar, CAS No.1310-65-2), La_2O_3 (preheated at 900 ºC for 8 h, Alfa Aesar, CAS No.1312-81-8), Ta_2O_5 (Alfa Aesar, CAS No.1314-61-0), ZrO_2 (Millipore Sigma, CAS No.1314-23-4) were mixed using a mortar and pestle. Later, 10 wt. % excess LiOH was added to the mixture of starting materials to compensate Li loss during the preparative/ sintering steps.

Later, a high-energy planetary ball mill (MSE supplies, MSE-PMV1-0.4L) consisting of Zirconia jars (500 ml) and Zirconia beads was utilized to grind and homogenously mix precursors powders using 2-Propanol solvent (Sigma Aldrich CAS No.67-63-0). The quantity of solvent used was optimized to the amount of precursor utilized (1:1 volume (ml) by weight ratio (g)) to prevent evaporation of the solvent during the milling process.

The mixtures were milled for 6 h at 300 rpm (clockwise -30 mins, anti-clockwise-30 mins with a rest step of 15 mins between each sequence to prevent overheating of the jars). The slurry was allowed to dry at 60 ºC for 6 h to drive away solvent before calcination.

The dried precursor powders were transferred to a high-alumina crucible (50 ml, catalog number: 65540). The crucible with closed lids were placed inside a programable box furnace (Nabertherm, LHTCT 01/16) at calcined at 950 ºC for 6 h with a temperature ramp rate of 3°C min^{-1}. On cooling down, the calcined LLZTO powders were re-milled using milling as mentioned above for a duration of 6 h at 300 rpm before carrying out pelletization and sintering.

3.1.2 Powder Compaction and Sintering

The calcined powders were collected and cold-pressed into a pellet using a 10 mm stainless-steel die set (Precision Elements Ltd) at three tons of load for 5 mins. The fabricated green pellets were placed on the top bed of mother powder inside 10 ml crucibles (**Figure 3.1)**. Later, green pellets were covered with additional mother powder to prevent Li loss during sintering (**Figure 3.1**). A schematic representation of the powder compaction, sintering bed preparation, and sintering process is represented in **Figure 3.2**. The pressed green pellets were sintered at various temperatures and durations to attain high ionic conductivity and relative density, detailed in individual chapters based on the garnet synthesis route and composition. Note: Arriving at an optimum sintering condition takes a lot of effort without forming a non-conductive pyrochlore phase. The sintered pellets were separated from the mother powder and polished using 400, 600, 1200 grit size silicon carbide polish paper until mirror-finished sides were obtained. The density of the sintered pellets was determined by measuring the mass and geometric volume. The relative density of the pellets was determined by dividing the geometrical density (mass of the pellet/ volume of the pellet) to the theoretical density based on the garnet composition. (Al-LLZO- 5.17 g cm^{-3} and Ta-LLZO- 5.5 g cm^{-3}).[60]

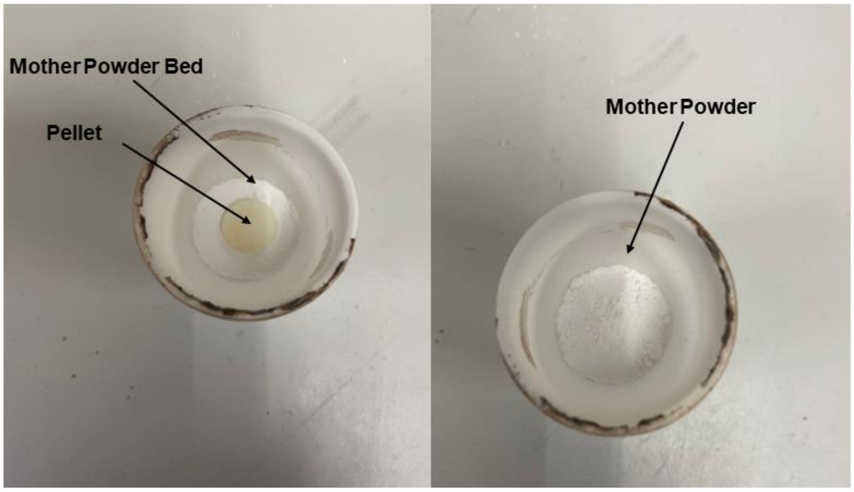

Figure 3. 1. Photographs (left) shows sintering arrangement using alumina crucible consisting of bed of mother powder and LLZO pellet, (right) embedding LLZO pellet with additional mother powder to prevent Li loss during sintering.

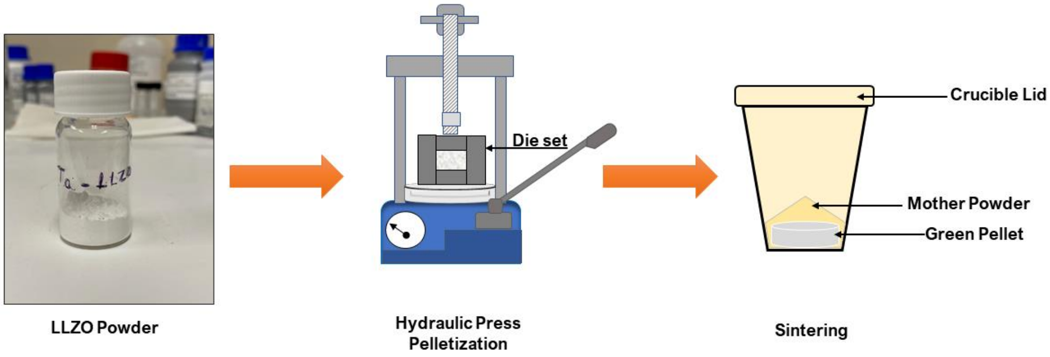

Figure 3. 2. A schematic representation of LLZO pellet compaction and processing.

3.2 Characterization Techniques

3.2.1 X-Ray Diffraction Technique

X-ray diffraction technique (XRD) was utilized to characterize the crystallinity and phase purity of the samples. Based on the principle explained by Braggs law, the scattering angle (θ) of the X-rays from a sample is a function of the wavelength (λ) emitted by the source, the interplanar spacing in the crystal (d), and n order of the reflection.

$$n\lambda = 2d\,\mathrm{Sin}(\theta)$$

To characterize the LLZO powders and pellets, a Bruker D-8 diffractometer with Cu Kα radiation (λ= 1.54 Å) were used to scan the samples from 10° to 60° with a step size of 0.02°. The phase identification and Rietveld refinement of XRD patterns were carried out using HighScore Plus software.[90]

3.2.2 Electron Microscopy Technique

Scanning Electron Microscopy (SEM) technique is widely used to analyze and characterize morphology (up to 50 nm resolution), the chemical composition of materials. A focused beam of high-energy electrons generated from a tungsten source is bombarded on the sample surface to generate a variety of signal (electron-sample) interactions.[91] LLZO samples were characterized using a Field Emission Scanning Electron Microscope (Hitachi S-4700, Eyring Materials Center, Arizona State University) operated at accelerating voltage 15 keV and emission current of 10 μA. Energy-dispersive X-ray analysis (EDX) of LLZO samples was carried out using a (JEOL JXA-8530F) Electron Microprobe Analyzer operated at 15kV and 50 nA emission current. High-Angle Annular

Dark-Field (HAADF) images of LLZO samples were acquired using a JEOL ARM 200F Scanning Transmission Electron Microscope operated at 200 kV.

3.2.3 Inductively Coupled Plasma Atomic Emission Spectroscopy (ICP-OES).

Ta and Al-doped LLZO samples elemental composition were characterized using liquid ICP-OES analysis developed by Smetaczek and co-authors.[92] An iCAP 6500 RAD (Thermo Fisher Scientific, USA) equipped with an echelle-type monochromator and a charge injection device detector was used for the analysis. Data acquisition was carried out using Qtegra software provided by the manufacturer of the instrument. Sample introduction was performed using an ASX-520 autosampler (CETAC Technologies, USA), PTFE tubing, and a sample introduction kit consisting of a quartz concentric nebulizer and a quartz cyclone spray chamber without ascension tube. Plasma torch containing a quartz injector tube of 1.5 mm inner diameter was utilized for the analysis Detailed information about the used instrumental settings is mentioned in **Table 3.1**. Sample digestion was performed using a borax fusion: 25 mg sample were mixed with 0.4 g borax and heated to 1000 °C for 5h. The solidified fusions were dissolved using a HCl/HF/H_2O mixture (10 wt% HCl, 0.8 wt% HF) at 70 °C.

Table 3. 1. Instrument settings for bulk analysis of LLZO samples using ICP-OES

Instrument Settings	
RF power	1200 W
Radial observation height	12 mm
Plasma gas flow	12 l min^{-1}
Nebulizer gas flow	0.8 l min^{-1}
Auxiliary gas flow	0.8 l min^{-1}
Integration time	5 s
Replicates per sample	5
Purge pump rate	1.6 ml min^{-1}
Analysis pump rate	0.8 ml min^{-1}
Analytical wavelengths ** used for quantification	Al 396.152 nm*, Eu 281.396 nm, Eu 381.967 nm, La 333.749 nm, La 412.323 nm*, Li 670.784 nm*, Ta 268.517 nm, Ta 240.063* nm, Zr 339.198 nm, Zr 343.823 nm*

3.2.4 Laser Particle Analyzer

A CILAS Alcatel laser particle analyzer was used to measure particle size distribution of as synthesized and milled powders prepared using molten salt and solid-state reaction method. This analysis technique is based on the diffraction and diffusion phenomena theory developed by Fraunhofer and Mie.[93] A beam of monochromatic laser source is target on the samples to obtain diffraction patterns consisting of concentric rings, the distance between the concentric rings is used to estimate particle sizes. Before carrying out any measurement, the instrument was auto rinsed to clear any residual particles present inside the tank. To characterize LLZO powders, approximately 2g of samples were weighed and dispersed in 50 ml DI water followed by 10 mins of ultrasonication. Later, carrier solution containing LLZO powders was introduced into the ultrasonic tank of the instrument. Instrument was operated in WET MODE selected using the Particle Expert Software during the data collection.

3.2.5 Electrochemical Impedance Spectroscopy

Electrochemical impedance spectroscopy (EIS) technique was utilized to characterize bulk and grain boundaries properties in solid ion conductors. Often a small amplitude of sinusoidal perturbation is applied on the system in the form of current or voltage, and its response is used to analyze various electrochemical process. EIS technique are widely used to study various processes in electrochemical storage devices such as ionic conductivity, electrical conductivity, interface resistance and mass/charge transfer process.[94,95] The response of the system (EIS data) is presented as a Nyquist plot consisting of real and imaginary part of the impedance on x-axis and y-axis respectively over a wide range of frequencies. In case of solid ion conductors, impedance spectra should show three distinct features attributed to bulk, grain boundary and a tail due to ion blocking electrode as represented in the **Figure 3.2.** In this work, sintered LLZO pellets were evaluated for bulk ionic conductivity, grain boundary conductivity and total ionic conductivity using an advanced broadband impedance analyzer (Novocontrol Concept 80) covering wide range of frequency from 10 MHz to 1 Hz. The QUATRO cryo-system attached to the broadband impedance analyzer enabled to record EIS measurements for a wide range of temperatures (-60 °C - 120°C) to understand Li^+ transport phenomena. Room temperature total ionic conductivity of the sintered pellets were carried out using a Bio-logic SP-200 Potentiostat from 7 MHz to 1 Hz. Before recording any impedance measurements, 20 nm of gold layer was sputtered on either side of the polished pellets as ion blocking electrodes.

The Z-view software was used to post-process EIS spectra's, to analyze bulk and grain boundary contributions using model developed by Irvine and co-workers.[116] Impedance spectra consisting of semicircle consist of reactive (capacitive) and resistive elements, both of which have to be estimated using Z-fit. Time constant, r, of each parallel *RC* elements is given by the product of *R* and *C* using **Equation 3.** In the frequency domain RC elements are separable at maximum frequency ω_{max} given by **Equation 4.** Based on the capacitance values process can be either assigned to bulk (10^{-12} F. cm^{-2}) or grain boundaries (10^{-9} F. cm^{-2}) contributions.

$$\acute{\Gamma} = RC \qquad \textbf{(3)}$$

$$\omega_{max} * RC = 1 \qquad \textbf{(4)}$$

To evaluate conductivities, each data set was normalized to the geometric dimensions as shown in **Equation 5,** where R_{total} is the resistance (Ω), A (cm^2) is area of the pellet, t (cm) is the thickness of the pellet and σ is conductivity of the pellet (S cm^{-1}).

$$\sigma_{total} = \frac{t}{Rtotal * A} \qquad \textbf{(5)}$$

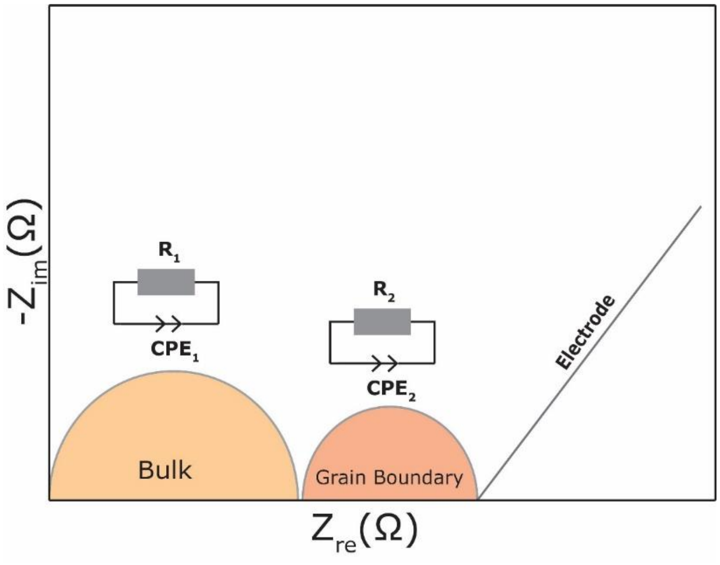

Figure 3. 2 Nyquist response plot of a solid ion conductor describing bulk, grain boundary and electrode processes with an equivalent circuit model.

4.0 SYNTHESIS AND PROPERTIES OF HIGHLY CONDUCTIVE $Li_{6.5}La_3Zr_{1.5}Ta_{0.5}O_{12}$ GARNETS BY MOLTEN SALT AND SOLID-STATE METHODS

4.1 Introduction

Synthesizing highly conductive c-LLZO using traditional solid state reaction method requires high reaction temperatures and long duration of calcination. Moreover, synthesized powders highly agglomerated in nature causing several manufacturability/ processing issues which are discussed at length in **Chapter 2.1**. While synthesis of LLZO using wet-chemical methods allows formation of c-LLZO phase at low-temperatures but requires use of expensive precursors, solvents, and multiple long duration calcination procedure making the process time intensive and less scalable.[96,97,98] Alternatively, molten salt method or flux synthetic method is used to produce several ceramic oxides in the past to overcome challenges associated with high-temperature solid state reaction method and non-scalable wet chemical routes . The molten salt method is an attractive route to produce nanocrystalline metal oxide powders using inorganic salts (flux) heated above its melting point in order to dissolve inorganic reagents and serve as a solvent system to for crystallization of metal-oxides at low temperatures.[99]

Reddy *et al*. carried out synthesis of Ta-doped LLZO using $LiNO_3$ and LiCl flux, however Ta-doped LLZO powders prepared using this route showed poor crystallinity, large agglomeration particles and inferior ionic conductivity (0.78×10^{-5} S cm^{-1}).[63] Poor ionic conductivity of Ta-doped LLZO powders can be attributed to aqueous washing step to remove the salts medium or due to improper selection of the fluxes (discussed in-depth **Chapter 2**). Later, Weller *et al*. synthesized Ga and Al doped LLZO nano-powders at low-temperatures (900 °C, 4 h) using LiCl and KCl flux.[100] Upon light milling of the as synthesized LLZO powder with LiOH, sintered pellets showed good ionic conductivity (0.2-0.3 mS cm^{-1}) but showed low relative density < 90 %. It is desired to have high relative pellet density to reduce grain boundary resistance and prolong short circuits in SE during symmetric cell cycling which would be discussed in **Chapter 6**.

Here in, a compatible eutectic mixture (LiCl:KCl) is employed for the first time to produce highly conductive sub-micron sized Ta-doped LLZO (LLZTO) at low temperatures (900 °C, 4 h) using inexpensive precursors. Furthermore, a detailed investigation on properties of Ta-doped LLZO (powders/pellets) prepared using novel molten salt method is compared with conventional solid-state reaction. This chapter also discusses in a great depth effect of sintering additives (LiOH, γ-Al2O3) and sintering medium (Platinum, Alumina) on structural, microstructural, chemical composition, and Li^+ transport behavior of pellets.

4.2 Experimental

4.2.1 Synthesis of Ta-doped LLZO using Molten Salt Method.

Garnets with nominal composition of $Li_{6.5}La_3Zr_{1.5}Ta_{0.5}O_{12}$ (LLZTO) were prepared using stoichiometric amounts of precursors: $LiNO_3$ (Alfa Aesar CAS No.7790-69-4), La $(NO_3)_3.6H_2O$ (Alfa Aesar CAS No. 10277-43-7), Ta_2O_5 (Millipore Sigma, CAS No. 1314-61-0), $ZrO(NO_3).xH_2O$ (Millipore Sigma, CAS No. 14985-18-3). Before mixing the precursors, $LiNO_3$ and La $(NO_3)_3.6H_2O$ were dried overnight in an oven held at 60°C under vacuum to drive away moisture from the salts. Later, precursors were weighed and mixed thoroughly using a mortar pestle with an additional amount 10 mol % $LiNO_3$ salt to compensate for Li^+ loss during the synthesis and sintering.

The eutectic salts mixture consisting of LiCl and KCl were weighed (45: 55 wt %) and added to precursors salts (1:1 ratio by weight) followed by homogenous mixing using a mortar and pestle. The salt mixture was transferred to a alumina crucible (50 ml, catalog number: 65540) covered with lid and placed inside furnace for calcination. Since the eutectic salt mixtures melts at 352 °C,[101] temperatures above eutectic melting point to were accessed to determine and optimize calcination conditions. Based on the optimization study, the mixture was held at 900 °C, 4 h (Nabertherm, LHTCT 01/16) with a slow heating rate of 3 °C min^{-1} to attain phase pure LLZTO. Post calcination and cooling of the crucible, ultrapure DI water was added to the mixture, and suspension was ultrasonicated (using a Cole-Parmer ultrasonic probe) for few mins. Followed by vacuum filtering using Whatman Grade filter (pore size- 0.7 μm) and washing of slurry with DI water (30 ml) and methanol solution (30 ml). Subsequently, collected LLZTO powders were dried in an oven set at 60°C before carrying out pelletization or any characterization.

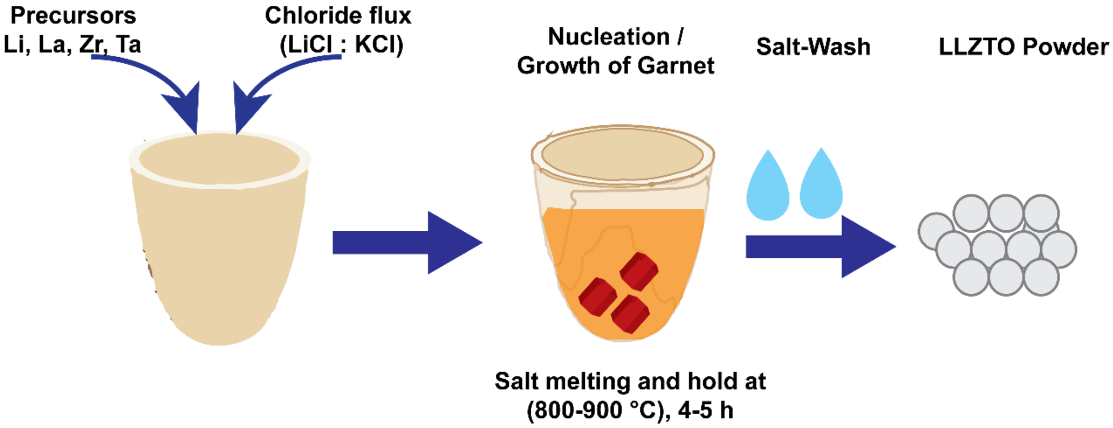

Figure 4. 1 Schematic illustration of molten salt synthesis using chloride (LiCl:KCl) flux to prepare LLZTO powders.

LLZTO powders were also synthesized using solid-state reaction method following the procedure mentioned in **Chapter 3 section 1.1** to contrast and understand properties of LLZTO prepared using molten salt method.

4.2.2 Pellet Preparation and Sintering

LLZO powders prepared using solid state method and molten salt method were compacted (Manual hydraulic press) into pellets applying 3 tons of load on a 10 mm stainless steel die set shown in **Figure 3.1**. Later, green pellets were placed inside Alumina crucible with bed of mother powder and covered with additional mother powder to prevent loss of lithium during sintering. All green pellets were sintered between 1100- 1200 °C between 10-16 h and optimized until the dense highly conductive pellets were attained. The density and ionic conductivity of pellets were determined using the procedure mentioned in **Chapter 3 section 3.1.**

4.2.3 Materials Characterizations

X-ray diffraction of the pellets and powders were carried out using a Bruker D-8 diffractometer with CuKα radiation with wavelength 1.54Å from 10 to 60° (2θ) at 5° min^{-1}. High Score plus software was utilized for phase identification. The sample morphology and microstructure of the samples were examined using Field Emission Electron Microscope Hitachi S-4700 or Zeiss Ultra Plus field-emission scanning electron microscope (SEM). Identification of elements on the pellet samples was carried out using energy dispersive X-ray spectroscopy (Oxford Instrument X-MAX 50 mm^2 SDD) coupled to the SEM. Point and mapping analyses were performed at 20 kV with a working distance of 9 mm. The EDX spectral integration time for point analysis was chosen as 30 sec and the elemental mappings were carried out using a total integration time of 30 min per image. The particle size distribution of the LLZTO powders prepared either by SSR or MSS methods before and after milling was measured with a CILAS ALCATEL laser particle size analyzer.

Inductively coupled plasma optical emission spectroscopy (ICP-OES, A Thermo Scientific iCAP 6500 Radial equipped with an echelle-type monochromator and a charge injection detector with Qtegra^{TM} Intelligent Scientific Data Solution Software) was employed for compositional analysis of the LLZTO samples. To prepare the samples, 25 mg of the sintered pellet was ground and digested with 0.4 g borax in a Pt crucible and heated to 1000 °C for 5 h in a Carbolite furnace; the solidified mass was then dissolved in a HCl-HF mixture (10 and 0.8 %) in DI water at 70 °C.

4.2.4 Ionic Conductivity Measurements

The sintered pellets were polished using SiC grinding paper with different grit sizes (#400, #600, and #1200) to attain flat mirror surface and remove impurities. Later, 200 nm of thin gold layers were deposited on top and bottom side of the pellets as blocking electrodes. The EIS-measurement were carried out using, an Alpha-A broadband impedance analyzer (Novocontrol Technolgies, Germany) from frequency range 10 MHz to 1 Hz. The QUATRO cryo-system attached to the broadband impedance analyzer enabled to record EIS measurements for a wide range of temperatures (-60 °C – 120 °C) to characterize bulk and grain Li^+ transport phenomena of sintered pellets and activation energies. The Z-view software was utilized to analyze and fit EIS spectra, detailed procedure and resources to fit the spectra can be found in here.[102]

4.3 Results and Discussions

4.3.1 Formation Mechanism and Properties of LLZTO Powders

The XRD patterns of the LLZTO powders prepared using either SSR or via the MSS method are shown in **Figure 4.2**. Both as-synthesized powders displayed reflections that could be indexed to the cubic garnet phase (PDF #04-019-2935); no other impurities or the pyrochlore ($La_2Zr_2O_7$) phase were observed. LLZTO prepared by MSS showed a lattice parameter of 12.94 Å, which was comparable to that prepared by SSR (12.91 Å). The formation of the cubic phase was found to occur at somewhat lower temperature and shorter duration through MSS (900 ^oC, 5 h) compared to that by SSR (950 ^oC, 6 h).

In the case of MSS, the eutectic mixture of LiCl-KCl (45:55 wt %) melts at ca. 352 ^oC and the nitrate-based precursors share the advantage of low decomposition temperature and better solubility in the eutectic medium producing oxides at low reaction temperatures due to faster and controlled kinetics. The MSS method was optimized by accessing wide range of temperatures between (500, 800 and 900 ^oC); the corresponding XRD patterns are shown in **Figure 4.3**. Lanthanum oxychloride (LaOCl) was the only crystalline phase formed at 500 ^oC; LaOCl completely dissolved to form lanthanum oxide (La_2O_3) and the lanthanum zirconium oxide $La_2Zr_2O_7$ at 800 ^oC. At 900 ^oC, the La/Zr species from $La_2Zr_2O_7$ and La_2O_3 re-dissolved in the eutectic medium to form phase pure c-LLZTO.

On the other hand, the SSR route typically requires high reaction temperatures (> 1000 ^oC) and longer synthesis periods because of slower solid-state kinetics. Ren *et al.* showed that the formation of impurity phases such as La_2O_3 and $La_2Zr_2O_7$, when using Li_2CO_3 as Li source, originates from the incomplete reaction at 900 ^oC (6 h). Both the source of Li and the duration of milling play a critical role in forming c-LLZO according to the SSR method.[103]

The SEM images of the LLZTO powders prepared by molten salt and solid-state reaction method before and after ball milling are shown in **Figure 4.4** together with information on the corresponding particle size distributions measured with a laser particle analyzer. **Figure 4.4a** presents an SEM image of the as-synthesized LLZTO powder prepared by SSR, which consisted of irregularly shaped and agglomerated particles. For comparison, the as-synthesized LLZTO powder prepared by MSS revealed spherical morphology with a lesser extent of agglomeration (**Figure 4.4c**). For the as-synthesized LLZTO powders by SSR particle sizes range from 10 to 30 µm (**Figure 4.4e**), while the MSS synthesis led to a bi-modal distribution (**Figure 4.4g**) with finer particles (1 to 20 µm). LLZTO prepared by SSR was milled for 6 h at 400 rpm to obtain a homogenous grain structure and to ensure uniform grain growth during the sintering step. As shown in **Figure 4.4f**, milling of the polycrystalline LLZTO ceramics prepared by SSR led to a uniform crushing of the large agglomerates resulting in almost spherical particles (**Figure 4.4b**) with an average diameter of approximately 2 µm and a rather narrow distribution width. To allow a comparison with the LLZTO samples prepared via MSS, the corresponding as-synthesized LLZTO powders of this preparation route were milled for 2 h at 400 rpm. Milling of the as-synthesized MSS powders reveals that the mean particle diameter finally takes values ranging from 10 to 5 µm (see **Figure 4.4 h**) with the spherical morphology being retained (**Figure 4.4 d**)

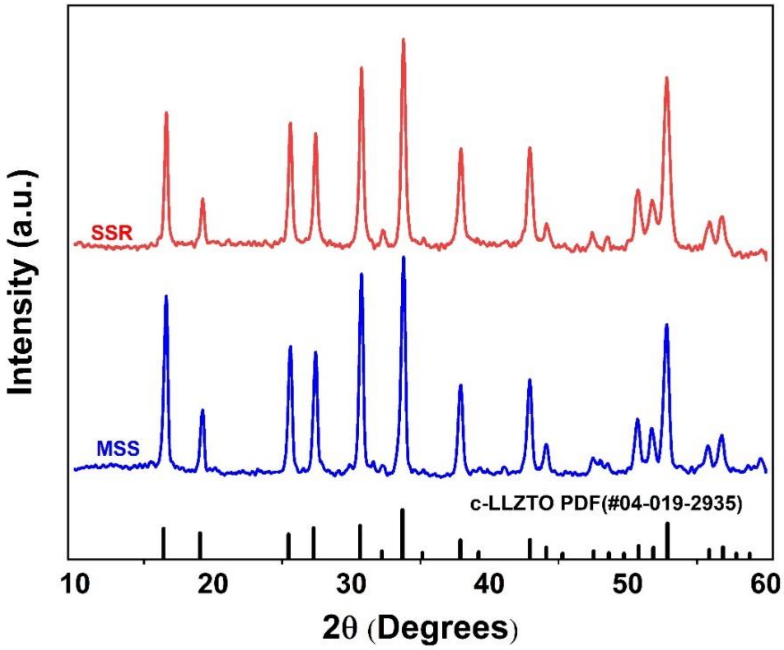

Figure 4. 2. XRD patterns of LLZTO powders prepared by the solid-state reaction method and molten-salt synthesis method.

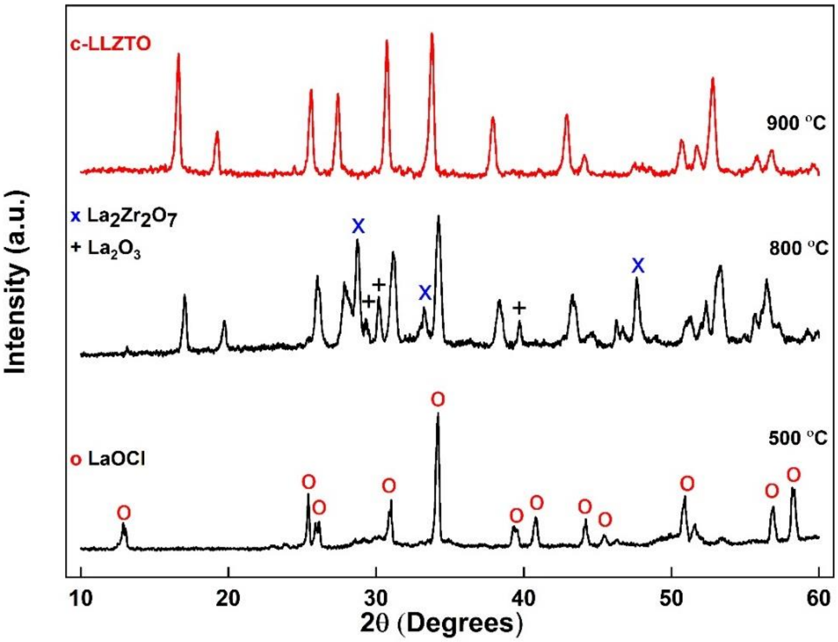

Figure 4. 3. XRD patterns corresponding to various reaction temperatures (duration 5 h) until the formation of c-LLZTO phase using MSS route.

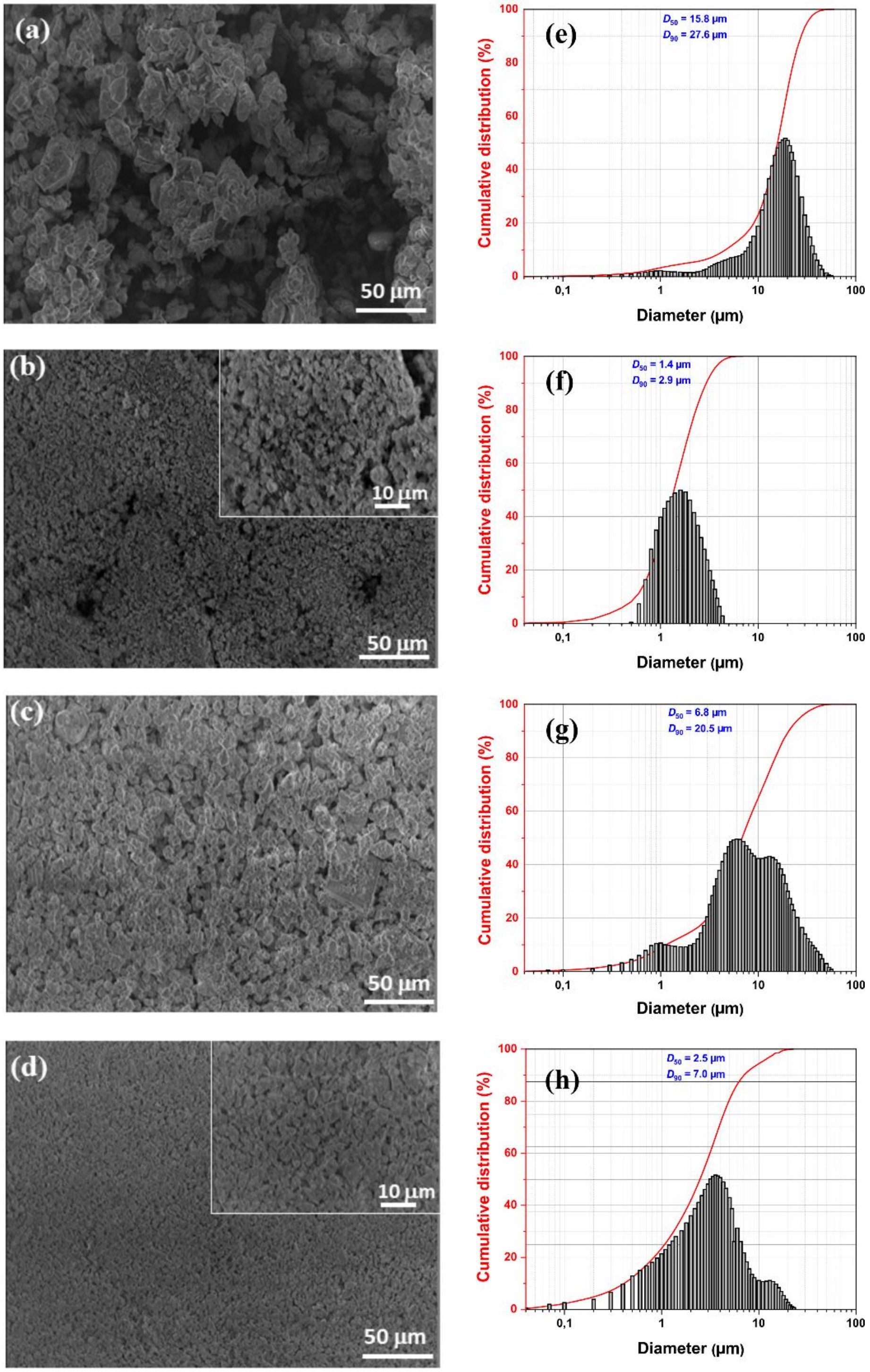

Figure 4. 4. SEM images and particle size distribution of the LLZTO samples prepared either by SSR (a, e: as-synthesized, b, f: after the milling step for 6 h) or by MSS (c, g: as-synthesized, d, f: after milling for 2 h).

4.3.2 Effects of Sintering Additives and Medium on Structural and Microstructural Properties of the Pellets

The LLZTO powders prepared via the two preparation routes sintered either in Pt or alumina crucibles. Initially, optimization of sintering conditions (duration and time) for the pellets prepared using molten salt and solid-state reaction method to attain high theoretical density and ionic conductivity was carried out using alumina crucibles for a wide range of temperatures and duration as listed in **Table A1**. It was observed that highest density of LLZTO pellets prepared via solid-state reaction method using alumina crucible was attained on sintering at 1140 °C /16 h and the MSS pellets similar densities were attained on sintering at 1200 °C/ 16 h without losing its cubic LLZTO phase. On further increasing sintering temperature and duration led to transformation to non-Li-conducting pyrochlore phases ($La_2Zr_2O_7$).[104] As it is desired to have high relative density of the pellets (> 95 %) to prevent Li dendrite growth pathway during cell cycling, grain boundary modification study was carried out using small amount of (5-10 wt.%) LiOH and (1wt.%) γ-Al_2O_3 as sintering additives.[105,106] LLZTO pellets sintered using 5- 10 wt. % LiOH and 1 wt. % γ-Al_2O_3 additives showed inferior microstructures due to presence of large pores (**Figure A1(a-d))** caused by low melting point of LiOH ~ 462 °C and formation of Li-Al-O eutectic causing accelerated grain growth caused by liquid phase sintering at 1055 °C.[107] Pellets having 10 wt.% of LiOH as sintering additives showed poor theoretical density compared to pellets having 5 wt.% of LiOH as sintering additives. Therefore, LiOH was no more utilized as sintering additives for rest of the experimental runs.

Later, The LLZTO pellets were sintered at various temperatures for several durations with and without additives γ-Al_2O_3 using different crucible to optimize their relative densities (> 90%), as summarized in Table S1. The pellets derived from SSR powders were named SSR-X while those from MSS powders were identified as MSS-X, with X = A indicating sintering in a Pt crucible, and B indicating that sintering took place in an alumina crucible; C means that an alumina crucible was used with additional γ-Al_2O_3 added as sintering aide, see **Table 4.1**.

Table 4. 1. Crystal structure, lattice parameter, ionic conductivities, and relative density values for the LLZTO pellets, prepared by SSR and MSS methods and sintered either in Pt crucibles or in alumina crucibles, prepared by SSR and MSS methods.

LLZTO synthesis method	Pellet name	Crucible	Additive	Phase(s)	Lattice parameter (Å)	Relative density (%)	Ionic conductivity (mS cm^{-1})
SSR	SSR-A	Pt	None	c-LLZTO	12.93	96	0.50
	SSR-B	Al_2O_3	None	c-LLZTO	12.90	94	0.36
	SSR-C	Al_2O_3	1 wt.% γ-Al_2O_3	c-LLZTO[a]		90	0.12
MSS	MSS-A	Pt	None	c-LLZTO	12.92	97	0.61
	MSS-B	Al_2O_3	None	c-LLZTO	12.91	93	0.34
	MSS-C[b]	Al_2O_3	1 wt.% γ-Al_2O_3	c-LLZTO[a], $LaAlO_3$		90	0.10

As seen from the XRD pattern in **Figure 4.5**, the pellets sintered in Pt crucibles, SSR-A and MSS-A, showed reflections originating only from the cubic LLZTO phase; the amount of impurities and secondary phases remained negligible. On the other hand, pellets sintered in alumina crucibles, of the stronger Li-O bond by the weaker O-H bonds[70,108] the observed lattice parameters indicate that proton exchange was either reversed or even absent for the LLZTO pellets after sintering.

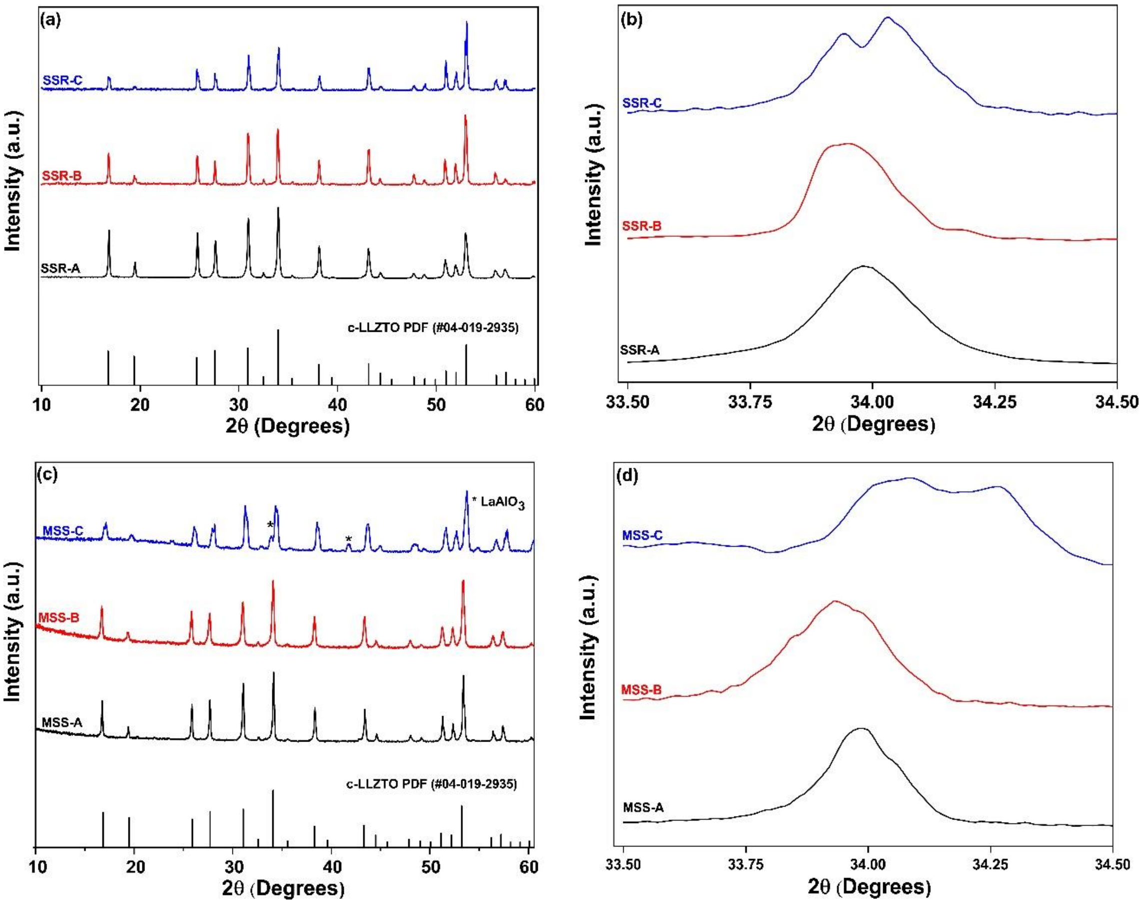

Figure 4. 5. XRD patterns of sintered LLZTO pellets prepared from SSR (a and b) and following the MSS route (c and d).

The ICP-OES analysis of the pellets sintered in alumina crucibles confirmed incorporation of Al in the LLZTO (see **Table 4.2**). The pellet derived from MSS powder (MSS-B) showed a slightly higher concentration of Al (0.31 moles per unit formula) compared to that from SSR powder (SSR-B) (0.26 moles per unit formula). The higher concentration of Al in MSS-B can be attributed to the higher sintering temperature (1200 ^{o}C) compared to that used for the SSR-B pellet (1140 ^{o}C). We assume that at higher temperature, incorporation of Al into the garnet framework takes place more effectively.

Additionally, the pellets sintered in alumina crucibles with 1 wt. % γ-Al_2O_3 sintering aide (SSR-C and MSS-C) showed a splitting of the reflections at $2\theta = 33.9^\circ$, as seen in **Figures 4.5b and 4.5d.** This splitting can be attributed to the presence of multiple cubic garnet phases[109] or, alternatively, to very high concentrations of Al. At such high concentrations one might assume site disorder also involving the La and Zr sites, see Düvel *et al*.[110] In the case of pellet MSS-C, an additional impurity phase, $LaAlO_3$, was observed in the XRD pattern suggesting that the Al content (0.498 moles) exceeded the solubility limit of Al in the garnet, which would be in line with the results by ICP-OES analysis (**Table 4.2**)

Table 4. 2. Elemental composition of LLZTO pellets sintered in Pt crucible, alumina crucible with and without additive, prepared by SSR and MSS methods.

Elements		SSR-A	SSR-B	SSR-C	MSS-A	MSS-B	MSS-C
Wt.%	**Al**	-	0.94 ± 0.06	1.11 ± 0.07	-	0.97 ± 0.06	1.60 ±0.10
	La	45.3 ± 0.7	54.9 ± 1.4	47.6 ± 1.2	44.3 ± 0.2	48.5 ± 1.3	49.7 ± 1.3
	Li	4.56 ± 0.01	5.20 ± 0.13	4.24 ± 0.11	4.70 ± 0.02	4.56 ± 0.12	3.79 ±0.10
	Zr	14.1 ± 0.2	15.0 ± 0.3	11.5 ± 0.2	16.0 ± 0.1	14.1 ± 0.2	11.5 ± 0.2
	Ta	11.9 ± 0.3	10.0 ± 0.4	10.1 ± 0.5	10.9 ± 0.1	10.3 ± 0.5	10.7 ± 0.5
Atomic ratio	**Al/La**	-	0.089 ±0.008	0.120 ± 0.011	-	0.103 ± 0.009	0.166 ±0.015
	Li/La	2.03 ± 0.03	1.90 ±0.09	1.78 ± 0.09	2.13 ± 0.01	1.88 ± 0.09	1.52 ± 0.07
	Zr/La	0.475 ±0.005	0.417 ± 0.011	0.367 ± 0.010	0.548 ± 0.005	0.443 ± 0.012	0.351±0.009
	Ta/La	0.202 ±0.002	0.140 ± 0.005	0.163 ± 0.006	0.189 ± 0.002	0.163 ± 0.006	0.166 ±0.006
Formula		$Li_6La_3Zr_{1.42}Ta_{0.64}O_{11.94}$	$Li_{5.69}Al_{0.269}La_3Zr_{1.25}Ta_{0.42}O_{11.3}$	$Li_{5.34}Al_{0.361}La_3Zr_{1.10}Ta_{0.49}O_{11.1}$	$Li_{6.4}La_3Zr_{1.64}Ta_{0.56}O_{12.4}$	$Li_{5.64}Al_{0.310}La_3Zr_{1.33}Ta_{0.49}O_{11.7}$	$Li_{4.57}Al_{0.498}La_3Zr_{1.05}Ta_{0.50}O_{10.9}$

Rangasamy *et al.*[44] showed that $LaAlO_3$ forms as a side phase when LLZO pellets are sintered above 1000 ˚C; $LaAlO_3$ is formed according to the reaction $La_2O_3 + Al_2O_3 \rightarrow 2\ LaAlO_3$ provided the Al content in the garnet is higher than 0.38 moles. The latter situation agrees with the present results.

Figure 4.6 shows cross-sectional SEM images of the fractured SSR and MSS pellets. As seen in **Figure 4.6a** and **4.6d**, the pellets (SSR-A and MSS-A) sintered in Pt crucible exhibited transgranular fracture[111] and an extremely dense microstructure and few pores. The relative density of the pellets was > 96% and EDX mapping confirmed that there was no Al (**Figure 4.7a** and **4.7d**) or Pt (**Figure A2**) along the grain boundaries.

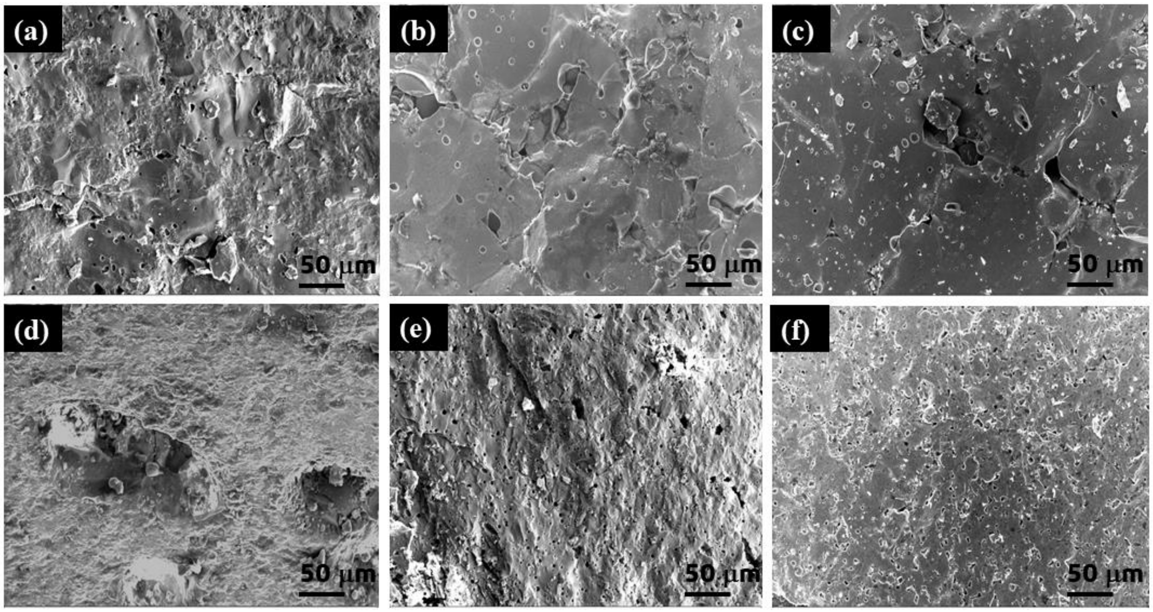

Figure 4. 6. Cross-sectional images of fracture surfaces for the sintered pellets (a) SSR-A, (b) SSR-B, (c) SSR-C, (d) MSS-A, (e) MSS-B, and (f) MSS-C.

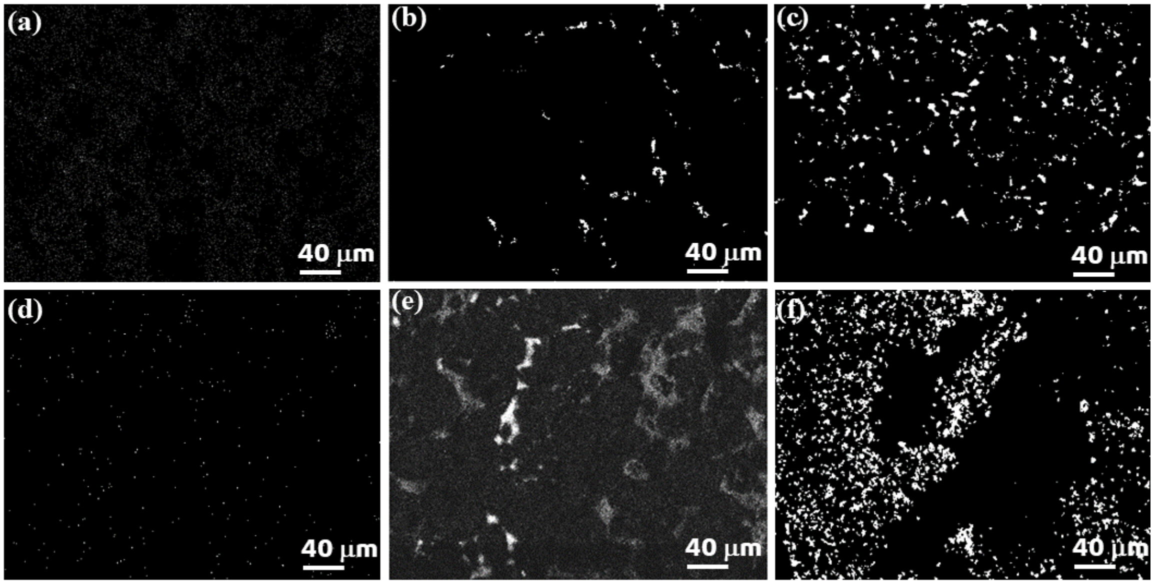

Figure 4. 7 EDX mapping of Al (a), (b), (c) LLZTO-SSR pellets and (d), (e), (f) LLZTO-MSS pellets. Pellets sintered in (a, d) Pt crucible and (b, c, e, and f) alumina crucible; (e, f) with Al_2O_3 additive

On the other hand, the pellets (SSR-B and MSS-B) sintered in alumina crucibles showed non-uniform grains with a mean pore size smaller than 5 µm and relative densities in the order of approximately 94% (**Figure 4.6b** and **4e**). EDX mapping (see **Figure 4.7b** and **4.7e**) suggested abnormally large grain growth, most likely caused by the presence of Al near the grain boundary regions. The reaction between Li with Al components can form intergranular liquid phases like Li_5AlO_4, $LiAl_5O_8$ and $LiAlO_2$, at temperatures as high as 1055 ^oC, which could accelerate abnormal grain growth through mass transport leading to pore formation.[112,113] In contrast, the Li_2O vapor is chemically inert with Pt crucibles[114] and thus, the right Li^+ vapor pressure seemed to be maintained, which resulted in pellets with fewer pores and higher density. Furthermore, ICP-OES results (**Table 4.2**) point towards garnet samples with higher Li content when sintered in Pt-crucible. For comparison, the pellets sintered together with 1 wt.% γ-Al_2O_3, that is, the samples called SSR-C and MSS-

C, had uniformly large grains with many pores (relative density of ca. 90%) as seen in **Figure 4.6c** and **4.6f**, respectively. EDX mapping of the pellets confirmed that Al distributes across the grains (**Figure 4.7c** and **4.7f**); this finding correlates with a decrease in Li content in agreement with ICP-OES data (**Table 4.2**)

4.3.3 Solid-State Impedance Spectroscopy

Representative Nyquist plots of the LLZTO samples recorded at – 60 °C and at 25 °C are shown in **Figure 4.8** and **Figure 4.9**, respectively. Common to all samples is the existence of a more or less complete high frequency semiarc that can be described by a resistor (R) connected in parallel to a constant phase element (R||CPE). The electrical relaxation process seen in the high frequency regime is followed by a strong increase of the imaginary part of the complex impedance toward low frequencies; these tails are almost characterized by a constant angle in the complex plane plot. The low frequency impedance feature is attributed to electrode effects and can fitted by an additional R_e||CPE$_e$ element connected in series. This equivalent circuit helps in analyzing the sample-specific high frequency features but does not imply any mechanistic information. In general, the overall resistance of samples studied herein are dominated either by the bulk response or by the grain boundary contribution.[115] The response dominating the contribution is determined by analyzing the associated capacitances (C_i, with i = b, gb) that were calculated according to $C_\mathrm{i} = (R^{1-n}\,\mathrm{CPE}_i)^{1/n}$, with n as a fitting parameter describing the deviation from ideal, that is, Debye response (n = 1). The high frequency semi arcs are to be characterized by capacitance values in the order of 10^{-12} F as typically seen for intragrain processes; in contrast, values ranging from 10^{-11} to 10^{-9} F characterize grain boundary processes (see **Table 4.3**).[116] The total conductivities (σ_total) were determined from the high frequency intercept of this semicircle with the real axis. Capacitances, the values obtained for *n*, total conductivities (σ_{total}) and resistivities (ρ) are summarized in **Table 4.3**.

Evidently, LLZTO sintered in Pt crucibles (SSR-A and MSS-A) shows two times lower total resistivity values compared to samples sintered in alumina crucibles (SSR-B and MSS-B). The lower values of total resistivities could be related to low grain boundary resistance as these pellets showed higher density.[117] In addition, the higher resistance of samples sintered in aluminum crucibles seems to be related to the incorporation of Al into the garnet structure during high temperature sintering. The incorporation of Al into the garnet lattice leads to (i) a lowering of the Li content (see **Table 4.2**) that decreases the occupational and positional disordering of Li^+ and to (ii) a blockade of the Li-diffusion pathways in the Li-ion sublattice. Both effects are disadvantageous for long-range Li-ion transport. [118] The pellets sintered with 1 wt.% γ-Al_2O_3 (SSR-C and MSS-C) show lower Li-ion conductivities (0.1 mS cm^{-1} at room temperature) compared to the samples sintered without a sintering aid (see **Figure 4.9**). Likely, the lower conductivity observed is related to the segregation of $LaAlO_3$ in the grain boundary regions causing high grain boundary resistances. Nyquist plots of the MSS-C pellet recorded at − 60 °C (**Figure A3**) confirmed the presence of a highly resistive mid frequency arc. This arc, most likely, originates from the impurity phase ($LaAlO_3$) located at the grain boundary regions of the sample MSS-C.

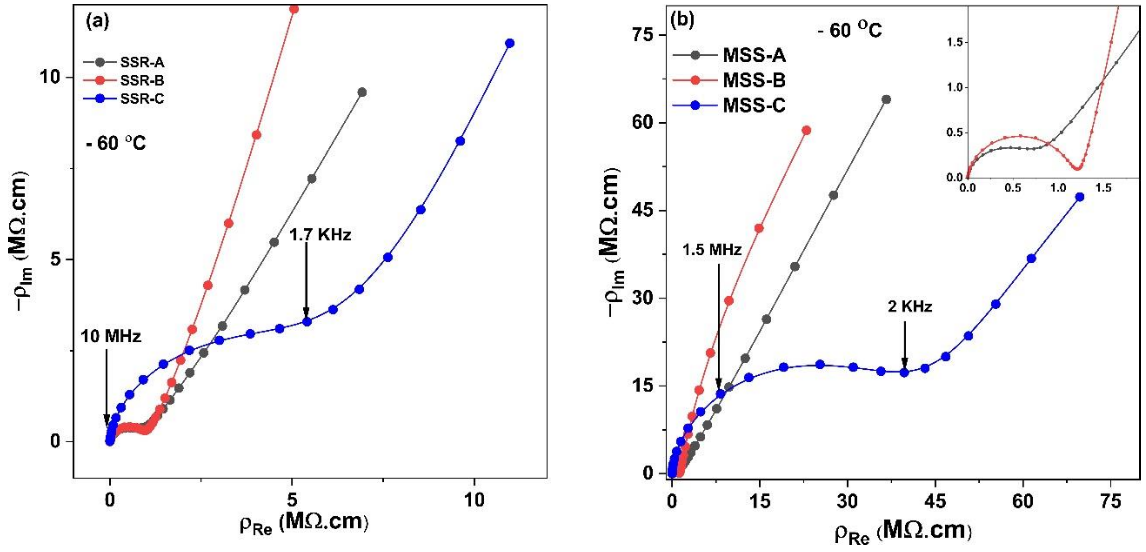

Figure 4. 8. Complex plane plots of impedance data recorded at − 60 °C for the sintered pellets obtained by (a) SSR, and (b) MSS routes.

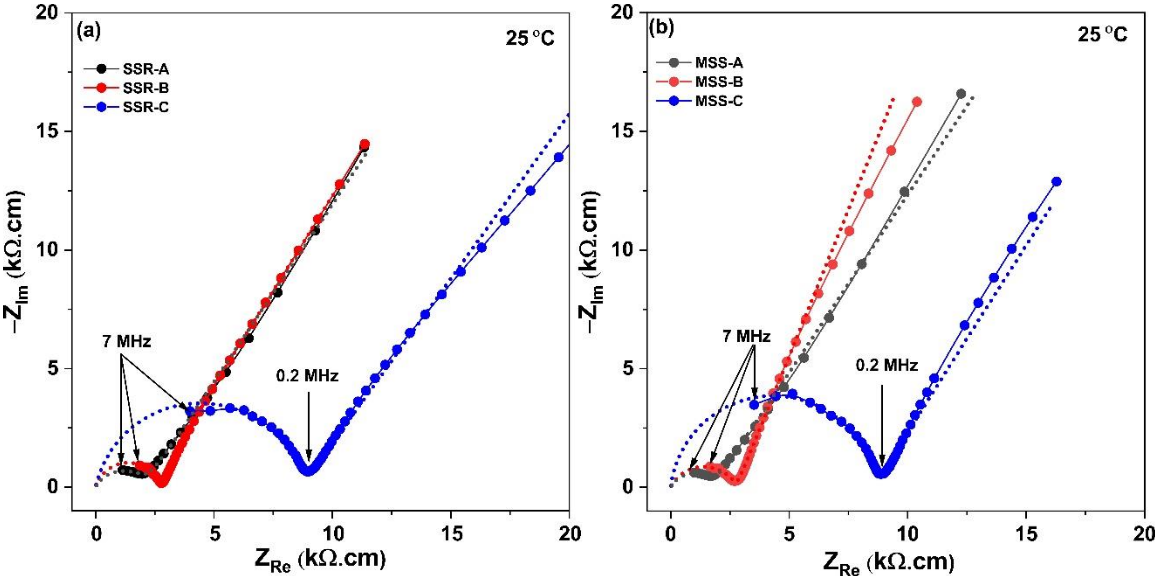

Figure 4. 9. Complex plane plots of impedance data (25 °C) of sintered LLZTO pellets prepared either by the SSR method (a) or via the MSS route (b).

Table 4. 3. Equivalent circuit parameters, the corresponding activation energies (E_a) and total conductivities as estimated from the EIS measurements at 25 °C for the LLZTO pellets prepared by the SSR route and the MSS method.

Pellets	ρ (Ω cm)	$C_{b,gb\ (= total)}$	$n_{b\ (= total)}$	E_a (eV)	σ_{total} ($mS\ cm^{-1}$)
SSR-A	1998	0.17 nF ^{gb}	0.70	0.38	0.50
SSR-B	2776	1.78 nF ^{gb}	0.81	0.39	0.36
SSR-C	8683	9.8 nF^{gb}	0.86	0.41	0.12
MSS-A	1666	0.12 nF^{gb}	0.79	0.37	0.61
MSS-B	2901	1.95 nF^{gb}	0.61	0.40	0.34
MSS-C[a]	8757	15.5 nF^{gb}	0.90	0.52	0.10

The temperature behavior of the ionic conductivity of the various LLZTO samples is shown in **Figure 4.10**. We analyzed conductivity properties at temperatures ranging from − 60 to 120 °C. The activation energy (E_a) was determined according to $\sigma_{(total)}T = A^{\prime} \exp(-E_a/k_BT)$. $A^{\prime}$ is the pre-exponential factor, k_B denotes the Boltzmann's constant and T is the absolute temperature. The activation energies determined using linear regression are given in Table 3. Overall, the activation energies for the LLZTO samples are very similar (E_a = 0.39(2)) and in good agreement with values commonly presented in the literature.[105] The only exception can be found for MSS-C showing a distinctly higher value. We assume that the MSS route leads to a preferred segregation of a passivating Al-compounds that hinders the Li-ion transport across the grain boundary regions (see above).[119]

In conclusion, excess Al decreases the total conductivity because of three important reasons. First, it changes the charge carrier concentration in the garnet structure, second it seems to block the Li-ion diffusion pathways, and third, it assists in forming highly resistive layers at the grain boundaries. These conclusions are strongly supported by XRD, EDS cross-sectional mapping analyses, and ICP OES (see above) giving clear evidence for the presence of Al^{3+} inside the grains and at grain boundaries as well as a reduced Li content of samples sintered in aluminum crucibles.

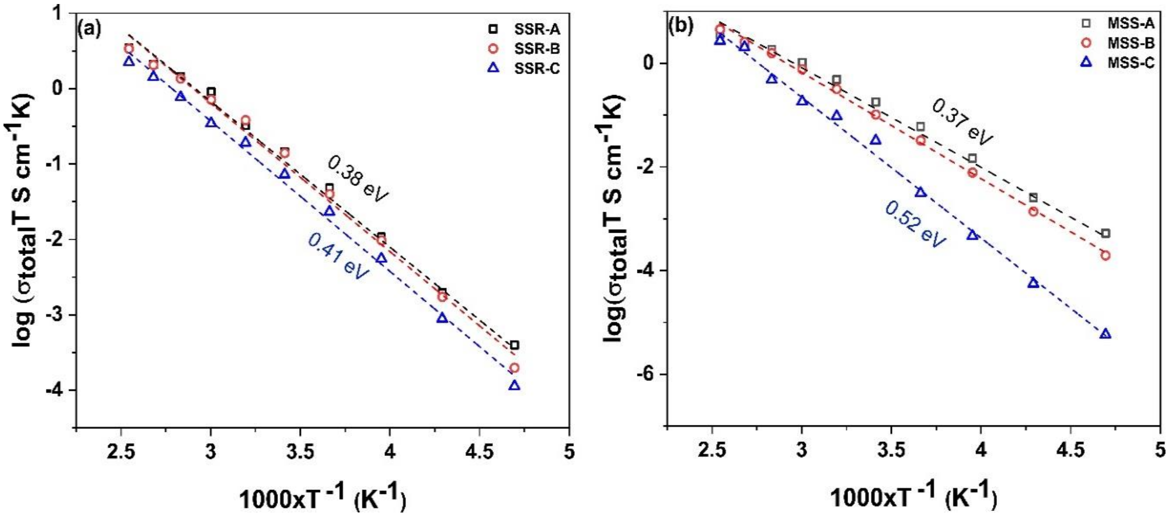

Figure 4. 10. Arrhenius plot of the (total) ionic conductivity of garnet-type LLZTO prepared by the SSR route (a) and by the MSS approach (b)

Additionally, **Table 4.4** compares the relative density and the total conductivity values of the LLZTO pellets prepared by SSR and MSS routes along with selected data presented in the literature using various sintering conditions and crucibles. It is evident that LLZTO can be prepared at lower temperature with better control of the morphology of particles when taking advantage of the MSS synthesis route. The LLZTO pellets showed better transport and microstructural properties when sintered in Pt crucible, as compared to expensive sintering techniques such as SPS or hot pressing. Furthermore, **Table 4.4** compares the relative density and the total conductivity values of the LLZTO pellets prepared by SSR and MSS routes along with selected data presented in the literature using various sintering conditions and crucibles. It is evident that LLZTO can be prepared at lower temperature with better control of the morphology of particles when taking advantage of the MSS synthesis route. The LLZTO pellets showed better transport and microstructural properties when sintered in Pt crucible, as compared to expensive sintering techniques such as SPS or hot pressing.

Table 4. 4. Comparison of density and conductivity values of LLZTO pellets with the literature. [a] spark plasma sintering, [b] hot pressing, [b*] hot pressing under Ar atmosphere

LLZTO Synthesis Method	Sintering Conditions	Additive/Crucible	Relative Density (%)	Ionic Conductivity (mS cm $^{-1}$)	Reference
SSR	1100 °C, 24 h	Al_2O_3 / Magnesia	94	0.32	Wang *et al.*[120]
	1000 °C, 10 min[a]	None / Graphite	95	0.69	Yamada *et al.*[121]
	1150 °C, 1 h[b*]	None / Carbon die	99	1.6	Du *et al.*[119]
	1140 °C, 16 h	None / Pt	96	0.5	Present work
MSS	900 °C, 24 h	None / Alumina	-	0.0078	Reddy *et al.*[63]
	1200 °C, 16 h	None / Pt	97	0.6	Present work
Co-precipitation	1050 °C, 1 h[b]	None / Graphite	97	0.8	Thompson *et al.*[122]

4.4 Conclusions

In the present study, the microstructure, phase composition, densification, and Li-ion transport properties of LLZTO powders prepared by both the molten salt synthesis route and conventional solid-state reaction were investigated. With the MSS approach, the cubic phase of LLZTO ($Ia\bar{3}d$) was attained at slightly lower process temperature and duration (900 ^{o}C for 5 h) compared to SSR synthesis (950 ^{o}C for 6 h). The as-synthesized LLZTO powder by MSS exhibited relatively small particle sizes with spherical morphology compared to the larger and aggregated particles observed with the SSR method. In addition, shorter duration of milling of the MSS powders led to sufficiently denser pellets, compared to that with the MSS powders. The ICP and EDX examination confirmed incorporation of excess Al (from the alumina crucible) on the Li sites and in grain boundary regions, leading to lower total Li ion transport. The use of γ-Al_2O_3 as sintering additive led to the formation of multiple cubic garnet phases, accompanied by the formation of $LaAlO_3$ that is located at the grain boundaries regions, with lower Li^+ ion conductivities. However, LLZTO pellets sintered in Pt crucible exhibited higher conductivities (0.5 to 0.6 mS cm^{-1}) with higher relative densities as compared to those sintered in alumina crucibles. It is evident that the MSS route seems to be a viable alternate method to the traditional synthesis procedures for LLZTO with high ionic conductivities. Based on the observation made by two competitive synthesis routes, the following parameters are very critical for getting highly conductive and dense pellets: (a) particle sizes of the synthesized powders under 2.5 µm; and (b) non-reactive sintering crucibles with optimum sintering conditions to retain Li content in the pellets above 6 pfu.

5.0 SYNTHESIS OF $Li_{6.28}Al_{0.24}La_3Zr_2O_{12}$ LITHIUM GARNETS BY SOLUTION-COMBUSTION TECHNIQUE FOR ALL SOLID-STATE BATTERIES

5.1 Introduction

High reaction temperatures and long duration of annealing involved in synthesizing LLZO through conventional solid state reaction route has motivated many researchers to look into low- temperatures wet-chemical routes. Although, wet-chemical routes like sol-gel, co-precipitation and Pechini method offers formation nanosized LLZO powders at low temperatures, however, wet chemical syntheses require use of expensive precursors, solvents, and time-consuming steps to attain final desired product as discussed in **Chapter 2 section 2.1**. To overcome challenges associated with classical wet-chemical route, motivated to explore synthesis of LLZO using solution-combustion method. The solution combustion method is a versatile method to prepare several nano-sized ceramics oxide in a short duration, and liquid-fuel precursor mixture can be easily adopted to liquid fed Flame Aerosol Combustion Synthesis to produce oxides in large quantities.[123,124,125] Herein, a water soluble fuel and inexpensive metal nitrates precursors are employed to synthesize sub-micron sized Al-doped LLZO in a short duration of 4 h without involving time consuming process typically observed in with other wet-chemical routes or solid state reaction. Al-doped LLZO green pellet consolidated from the solution combustion method on sintering at 1100 °C for a short duration of 6 h demonstrated high relative densities (> 92 %) and high ionic conductivity up to 0.45 mS cm^{-1}.

5.2 Experimental

Synthesis of Al doped LLZO ($Li_{6.28}Al_{0.24}La_3Zr_2O_{12}$) was synthesized using process as described in the flow chart shown in **Figure 5.1.** Aforementioned synthesis route can be easily applied to produce single phase cubic Ga-LLZO ($Li_{6.4}Ga_{0.2}La_3Zr_2O_{12}$) see **Figure. B1** for x-ray diffraction patterns. Stoichiometric amounts of $LiNO_3$ (Alfa Aesar, CAS No.7790-69-4, 5-10 wt.% excess Li source was added to compensate Li loss during the combustion reaction or sintering), La $(NO_3)_3{\cdot}6H_2O$ (Alfa Aesar, CAS No.10277-43-7), Al $(NO_3)_3{\cdot}9H_2O$ (Millipore Sigma, CAS No.7784-27-2), $Ga(NO_3)_3\ {\cdot}xH_2O$ (Millipore Sigma, CAS No. 69365-72-6) and $ZrO(NO_3){\cdot}xH_2O$ (Millipore Sigma, CAS No. 14985-18-3) were dissolved in minimum amount of ultra-pure DI water at 80 ºC. Later, carbohydrazide (CH_6N_4O) fuel (Millipore Sigma, CAS No. 497-18-7) was dissolved in ultra-pure DI water and subsequently mixed/ stirred with the precursor solution at 80 ºC for about 10 mins until gelation occurred. The molar concertation of the fuel was determined based on the total oxidizing and reducing valences as described by Jain *et al*.[126] and the detailed calculations and synthesis procedure is provided in the **APPENDIX B**. The dehydrated gel was introduced into a preheated muffle furnace at 500 ºC to trigger combustion and the self-sustained ignition led to voluminous fine foamy product. The as-burnt foamy powder (**Figure. B2)** was collected, lightly ground, and calcined in MgO crucible (Tateho Ozark Technical Ceramics) between 600 and 900 ºC until cubic phase Al-LLZO was obtained.

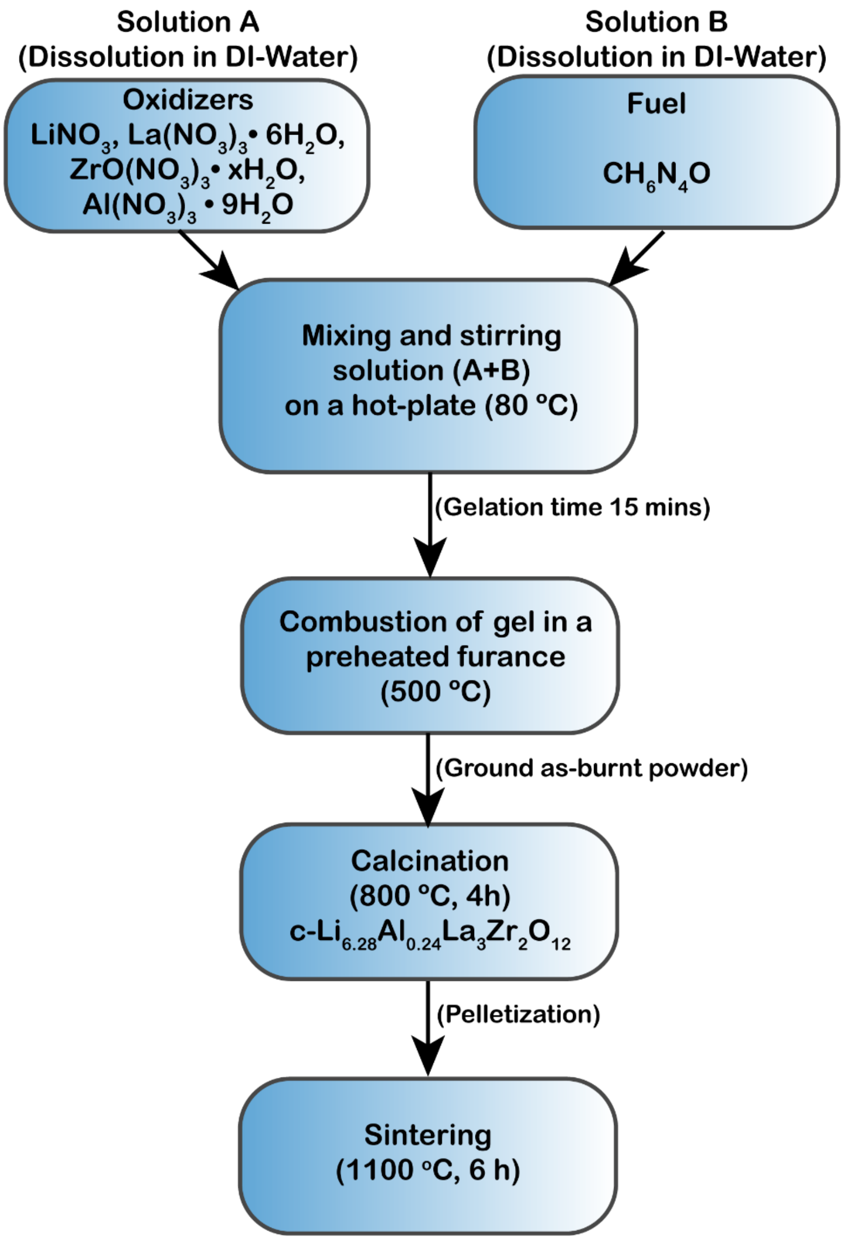

Figure 5. 1. Schematic representation of solution combustion synthesis process to prepare Al-doped LLZO using solution combustion technique.

5.3 Materials Characterization

X-ray diffraction (XRD) was conducted for the powder and pellet samples using a Bruker D8 ADVANCE diffractometer (Ni filtered Cu radiation with wavelength $\lambda_{K\alpha 1}$ =

1.54 Å, 40 kV/50 mA) from 10 to 60° (2θ) at 5° min $^{-1}$ in 0.02° increments. The phase detection of the crystal structure and refinements were carried out using High Score Plus. The surface morphology of the LLZO samples was examined using a FE-SEM Hitachi S-4700 operated at 15 kV and 10 μA emission current. High-angle annular dark-field (HAADF) images were recorded using a JEOL ARM 200 Scanning Transmission Electron Microscope (STEM) at 200 kV. Energy dispersive X-ray (EDS) elemental mapping was acquired with an AZtec 100 mm^2 windowless detector from Oxford Instruments. The Al-LLZO powder samples were sonicated for 10 min in methanol and the suspended particles were drop cast on lacey-carbon grid. The surface morphology and elemental mapping of the fractured pellets were analyzed using a SEM Electron Microprobe Analyzer (JEOL JAX-8530F) operated at 15 kV and 50 nA emission current. Thermogravimetric/differential thermal analysis of the as combusted powders was carried out using a Labsys Evo in air up to 900 ºC with 5 ºC min^{-1} using a Pt-crucible (10 ml).

Compositional analysis of the Al-LLZO samples was performed using inductively coupled plasma optical emission spectroscopy (ICP-OES). An iCAP 6500 RAD (Thermo Fisher Scientific, USA) and Qtegra software provided by the manufacturer of the instrument was used for all measurements. Detailed information about the used instrumental settings is listed in **Table 3.1**. For sample digestion, borax fusion was used: 50 mg sample (crushed and ground using an agate mortar to ensure homogeneity) were mixed with 0.8 g borax and heated to 1000 °C for 5 h. A HCl/HF/H_2O mixture (10 m% HCl, 0.8 m% HF) at 70 °C was used to dissolve the solidified fusions. For signal quantification, conventional external calibration using aqueous standards prepared from certified single element ICP-standard solutions was used. Internal standardization (0.2 mg

kg^{-1} Europium) was applied to correct instrumental drifts and variations in sample introduction.

5.3.1 Pellet Compaction and Sintering

The Al-LLZO green pellets were consolidated via cold-pressing using a 9 mm diameter die set at 3-ton load for 5 min. The green pellets were kept covered with the sacrificial mother powder (to prevent loss of Li) in MgO crucible with lid covering during sintering**.** The pellets were held first at 950 °C for 1 h for removing any contamination layers such as LiOH or Li_2CO_3, followed by sintering between 1000 °C and 1100 °C for 6 h. The theoretical density of the Al-LLZO pellet was considered as 5.1 g cm^{-3} [100] and the r elative density of sintered pellets was calculated based on the volume and weight after sintering.

5.3.2 Ionic Conductivity Measurements

The sintered Al-LLZO pellets were polished using SiC paper (800, 1000 and 1200 grit sizes) to obtain mirror finish surface followed by gold sputtering (thickness 100 nm). Electrochemical Impedance measurements were carried out from 0 to 60 ºC with 20 ºC steps using a Biologic SP-200 Potentiostat/Galvanostat/FRA from 7 MHz to 1 Hz for estimating conductivity and activation energy. Impedance spectra analysis carried out using ZView software. Prior to each impedance measurements, the pellets were stabilized at the set temperature for ~30 min using a ESQEC thermal chamber.

5.4 Results and Discussions

The nature of the combustion reaction is largely governed by the type of fuel and fuel to oxidizer ratio (F/O), which in-turn defines the microstructure, crystallinity, and phase purity of combusted product.[127] In the present study, a water-soluble fuel *i.e.*, carbohydrazide (CH_6N_4O) having low melting point: ~ 154 °C and high combustion index was utilized for synthesizing Al-substituted LLZO. Previously, carbohydrazide based fuels have been utilized to synthesize various high purity nanostructured ceramics and spinel aluminates.[128,129] In addition, hydrazine-based fuels act as a chelator forming bidentate ligands with metal cations to prevent selective precipitation on dehydration of water promoting homogenous combustion.[130,131,132] To understand formation mechanism of cubic Al-LLZO, F/O ratio was systematically varied from fuel-lean zone (F/O = 0.5) to fuel-rich zone (F/O = 4.0), followed by a calcination step of as-burnt powders at 900 ºC for a duration of 4 h (see **Table B3** for nature of the combustion). The calcined powder samples were characterized by XRD and SEM for optimizing the molar concentration of the fuel to control phase purity and morphology of the Al-LLZO powders.

The XRD patterns (see **Figure 5.2**) of calcined powders showed reflections from the cubic phase of Al-LLZO for all values of F/O ratios on calcining at 900 ºC for 4 h with varied intensity of flame on combustion. In general, fuel lean conditions (F/O = < 1) produce sluggish combustion reactions, while fuel rich conditions (F/O = >1) produce smolder type reactions. Whereas stoichiometric fuel conditions (F/O =1) led to high intensity flame type reactions following the similar trend observed elsewhere.[133] On calcining the as-burnt powders, the presence of a minor intermediate phase of $Li_{0.5}La_2Al_{0.5}O_4$ (JCPD 04-1167) was observed for F/O ratios between 0.5 to 2, in-addition to cubic Al-LLZO as a major phase. The formation of $Li_{0.5}La_2Al_{0.5}O_4$ as an intermediate phase is commonly observed with the both high temperature synthesis routes and wet synthesis routes due to the reaction between $LaAlO_3$ and excess Li source which forms at sufficiently low temperatures (~600 °C) compared to the conductive cubic-LLZO phase.[44,54] However, on increasing F/O value to 4 led to complete transformation of precursors to cubic phase without any intermediated or impurity phases such $Li_{0.5}La_2Al_{0.5}O_4$, $La_2Zr_2O_7$, $LaAlO_3$ and γ-Al_2O_3, which are common in the case solid-state reaction methods.[134,110] Absence of impurity phases can be attributed to high enthalpy and flame temperatures caused by increasing molar concentration of the fuel.[135]

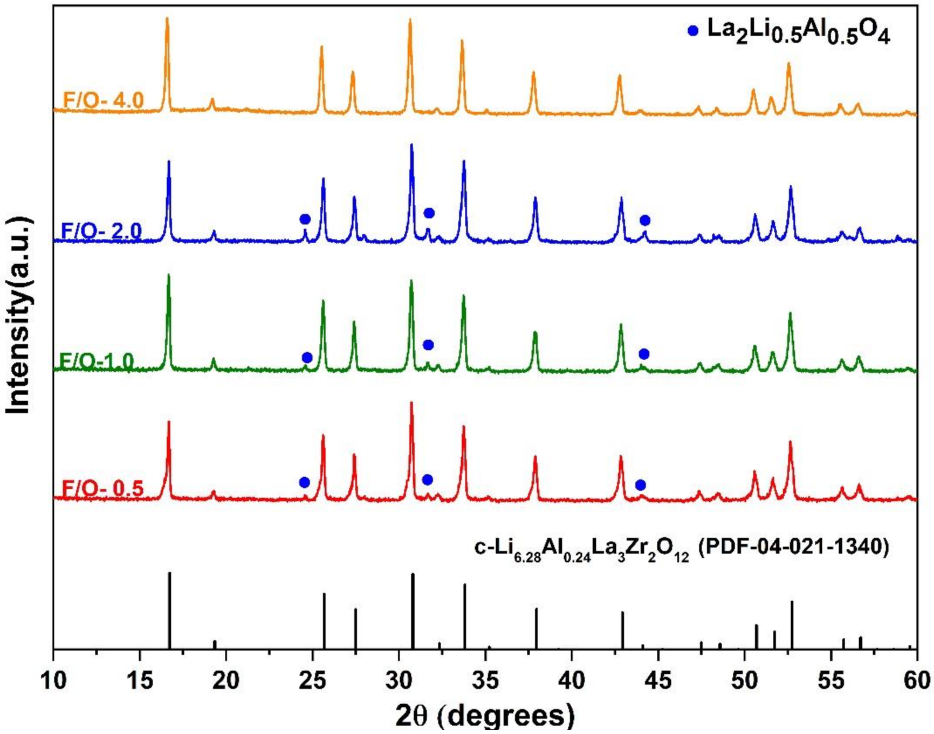

Figure 5. 2. XRD patterns of Al-LLZO samples calcined at 900 °C/ 4 h with various fuel to oxidizer (F/O) ratios.

Figure 5.3 (a-h) shows the representative scanning electron micrographs of Al-LLZO powders with varying F/O ratios. At F/O ratio of 0.5 (*i.e.*, fuel-lean condition), the Al-LLZO sample showed mixed morphologies of spherical shape (0.5 to 1.0 µm) and ligamented structures as observed in the **Figure 5.3a** and **5.3b**. On increasing F/O ratio value to 1 (*i.e.*, stoichiometric condition) led to growth in particle size with reduction in the porosity and the morphology exhibited well-sintered ligamental type growth (**Figure 5.3c** and **3d**). Under the fuel-rich conditions (F/O = 2, 4), the particle morphology observed was predominantly taking near uniform ligament structures having width of ~2 µm with limited porosity (**Figure 5.3(e)** to **5.3(h)**). In general, lower F/O ratios produce near spherical particles, preventing necking and growth in the particle sizes due to lower enthalpy of the reactions, while the higher F/O ratios cause interparticle grain growth with increase in the combustion flame temperatures and limited CO_2 and NO_2 evolutions.[136, 133]

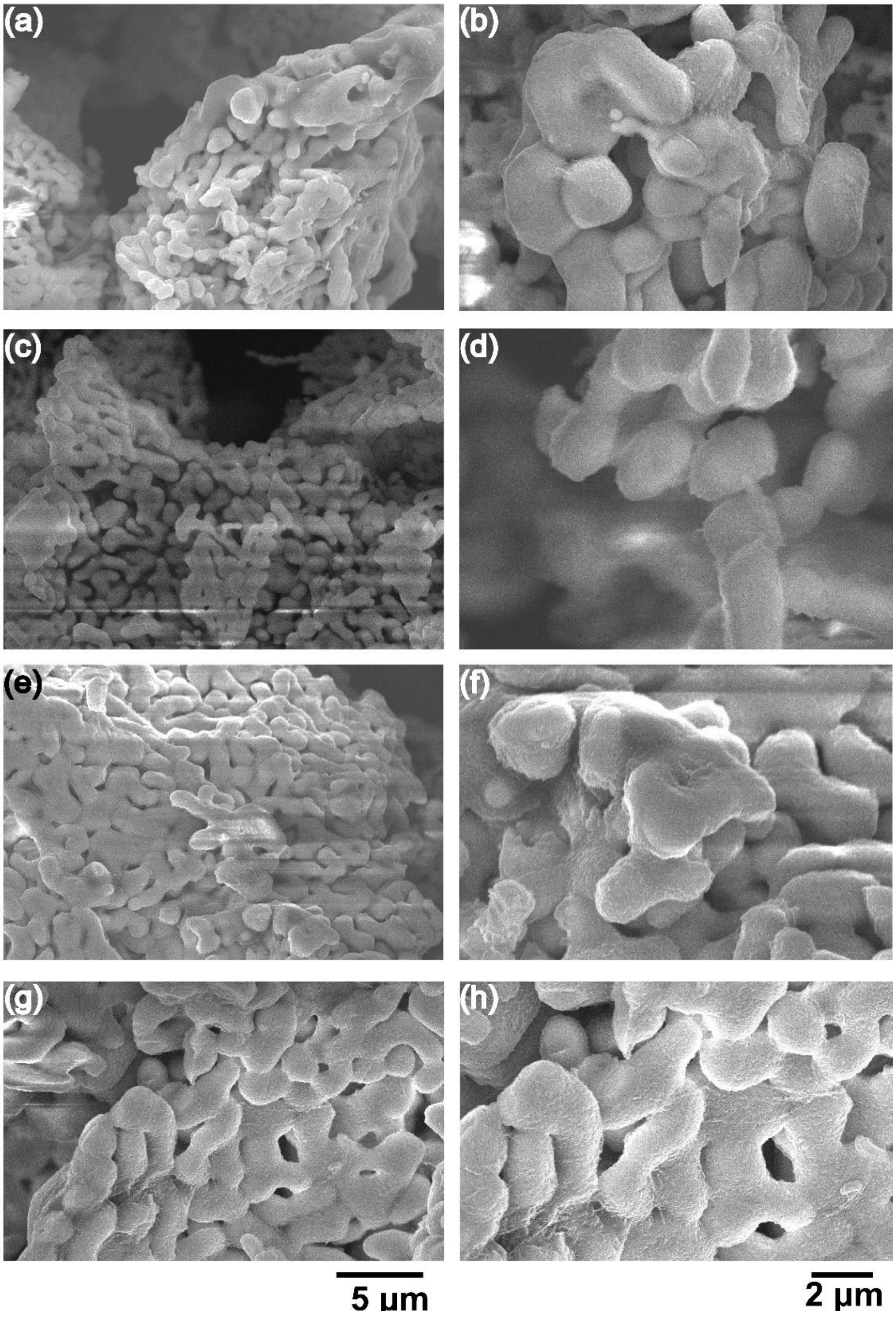

Figure 5. 3. Representative SEM images Al-LLZO powders synthesized by combustion method with various fuel to oxidizer (F/O) ratios of (a,b) 0.5, (c,d) 1.0, (e,f) 2.0 and (g,h) 4.0 at two different magnifications.

On setting F/O ratio to 4, calcination temperatures were optimized between 600-900 °C to attain cubic Al-LLZO phase. The XRD pattern for Al-LLZO sample before calcination revealed the presence of nanocrystalline $La_2Zr_2O_7$ pyrochlore phase (**Figure 5.4**), which are observed with sol-gel and other synthesis methods.[51,104] A STEM and EDS mapping analysis carried out on the as-burnt powder confirmed homogenous distribution of Al dopant (**Figure 5.5**) eliminating possibility of forming unfavorable, less conductive t-LLZO or mixed c-LLZO/ t-LLZO phases. By calcining the as-burnt powder above 600 ºC for 4 h, formation of c-LLZO phase was observed (**Figure 5.4**) along with minor phases of $Li_{0.5}La_2Al_{0.5}O_4$ up to 700 ˚C. However, calcination at 800 ºC led to complete formation to c-LLZO without any intermediate phases with lattice constant of 12.98 Å (see **Table B4**), which agrees with that by the solid-state reaction methods.[137] The calcined powders at 800 ºC showed particle size of approximately 200 nm with homogenous distribution of Al along the grains as seen in the **Figure 5.6**. The ICP-OES analysis of the Al-LLZO powders calcined at 800 °C revealed powder having composition of $Li_{6.58}Al_{0.22}La_{2.91}Zr_2O_{12}$ (refer to **Table B5**) which is very near to the targeted synthesis composition.

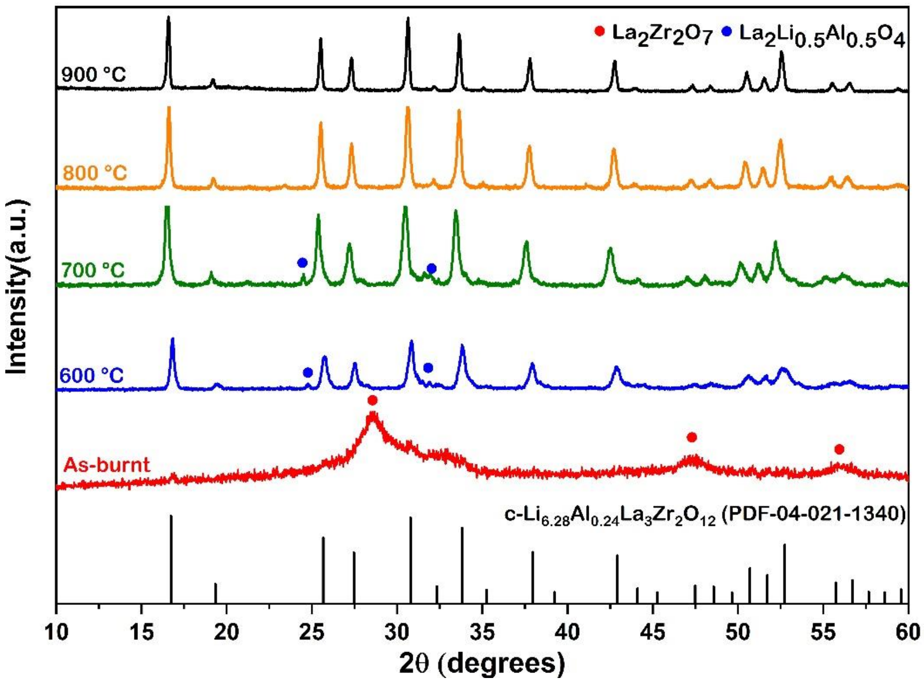

Figure 5. 4. XRD patterns of as-burnt and Al-LLZO powders calcined between (600-900 ºC) for 4 h at F/O ratio 4.

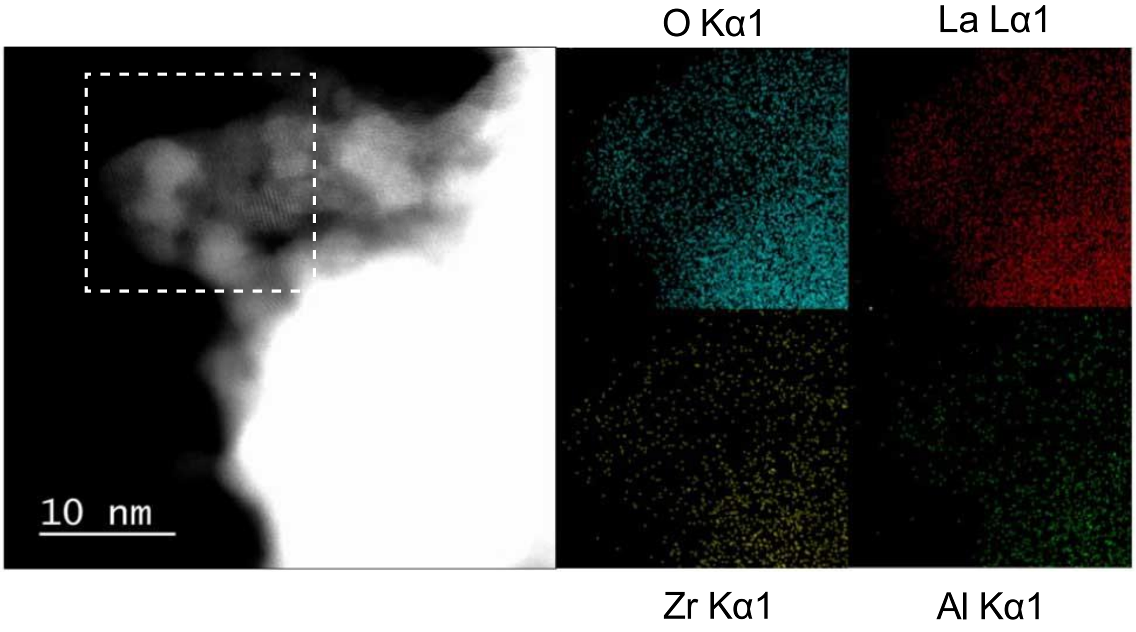

Figure 5. 5 STEM-EDS elemental map of as-combusted powders showing elemental distribution for (O, La, Zr, Al).

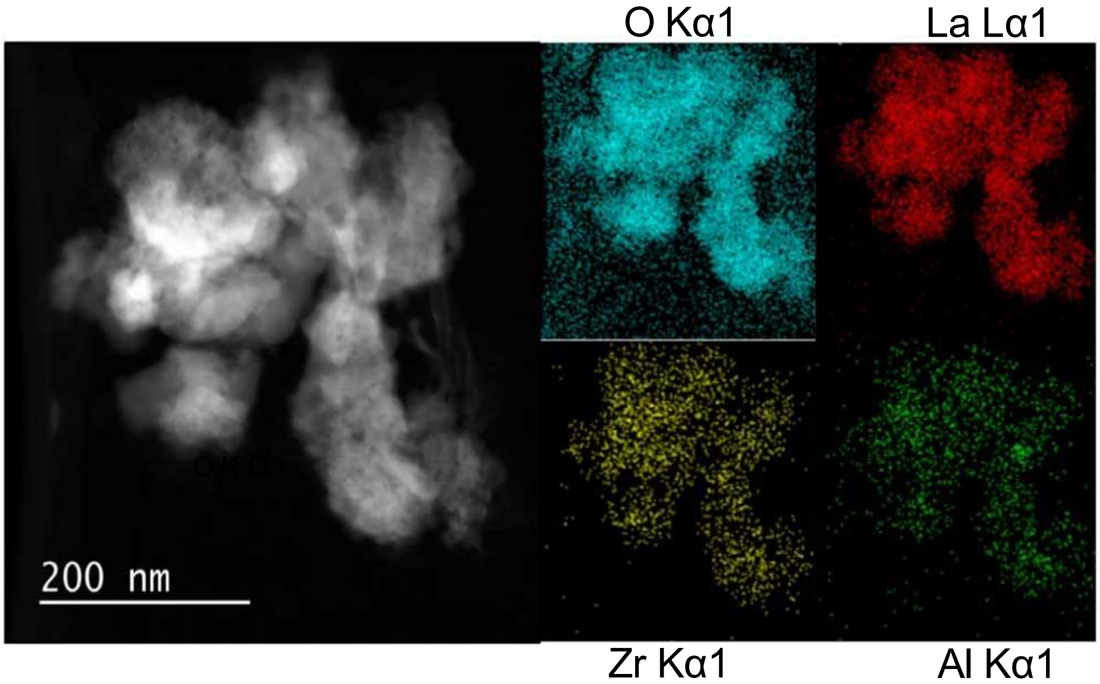

Figure 5. 6. STEM-EDS elemental map of Al-LLZO powders calcined at 800°C for 4 h showing homogenous elemental distribution for (O, La, Zr, Al).

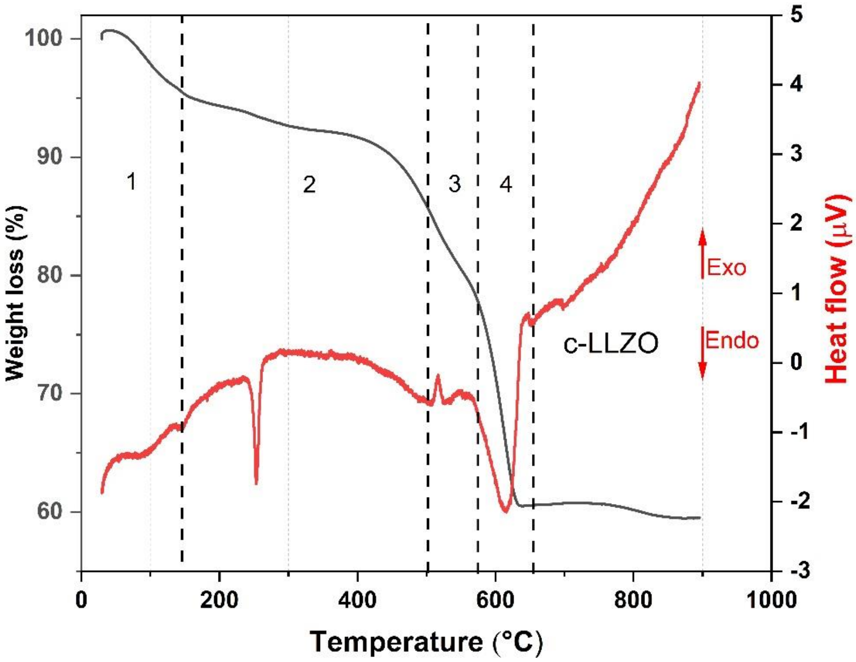

Figure 5. 7. TGA-DTA analysis of as-combusted powders from room temperature until crystallization of c-LLZO phase (up to 900 ºC).

5.4.1 Effect of Sintering Temperatures on Microstructures and Ionic conductivity

The Al-LLZO powders calcined at 800 °C, 4 h were selected for fabricating green pellets followed by sintering between 900 and 1200 °C for 6 h to evaluate the microstructural and Li^+ transport properties. The sintering duration of 6 h was selected throughout the experiments to avoid excess Li loss from the garnets. The pellets sintered at 900 ºC for 6 h exhibited low relative density of only ~ 75%, featuring large open pores with intergranular fractures as seen in **Figure 5.8a.** Incomplete densification of pellet led to poor Li^+ conductivity (as seen in the Nyquist plot, **Figure B3**). On sintering pellets at 1000 ºC for 6 h led to increase in relative density reaching up to ~ 86 % and improved Li^+ ionic conductivity to 0.2 mS cm $^{-1}$. However, fractured SEM images of the pellets showed presence of uniformly distributed pores as seen in **Figure 5.8b**. The presence of open pores seen in the Figure 5b is likely caused by liquid phase sintering of Li-Al-O eutectic mixture, which occurs at ~ 1055 °C leading to partial or incomplete accelerated grain growth leaving behind pores.[138] The XRD scan of the sintered pellet revealed cubic Al-LLZO as a major phase along with minor traces of Li_2ZrO_3. The Li_2ZrO_3 are commonly reported during the sintering of Al-LLZO, which are formed as an intermediate phase due to reaction between excess Li and Zr source in the garnet or in some cases observed as a surface contamination on exposure to air and found to disappear during polishing of the pellet surface.[138,139] On ramping up sintering temperature to 1100 ºC, pellets retained c-LLZO as the main phase showing high relative density of 92 % and high Li^+ conductivity of 0.45 mS cm^{-1}. The fractured surface SEM image (in **Figure 5.8c**) showed a flat surface indicating transgranular fracture with high grain boundary strength and limited pores compared to pellet sintered at 1000 °C for 6 h. Presence of tiny, closed pores can be attributed to several factors such as Li_2O loss during sintering process or due to smaller particles of as-synthesized powders, which may prevent full densification caused by poor necking.[139,140] Interestingly, pellet sintered at 1100 °C did not exhibit Li_2ZrO_3 minor phases (**Figure 5.8d**) in absence of excess Li source and as well no Al- rich secondary phases such as $LaAlO_3$ were observed leading to resistive grain-boundary transport.[141] A minor peak of $La_2Zr_2O_7$ detected at $2\theta \sim 29°$ on the surface of the pellet but did not show any severe impact on the Li^+ ion conductivity. The ICP-OES analysis confirmed a slight loss in the Li content of pellet sintered at 1100 °C ($Li_{6.24}Al_{0.20}La_{2.89}$ $Zr_2O_{11.8}$, refer **Table B5**) compared to the starting composition of the powder ($Li_{6.58}Al_{0.22}La_{2.91}Zr_2O_{12}$). However, Li and Al mole concentration of the pellet was found to be in the optimum stoichiometric range to form fast conductive cubic Al-LLZO phase preventing formation of t-LLZO phase caused by either excess Li concentration (> 6.24 moles) or low Al concentration (< 0.20 moles).[44] EDS mapping carried out on the cross-section of the pellets confirms no presence of Al-rich phases at the grain boundaries (**Figure B4**). Pellets sintered at 1200 ºC / 6 h, showed prominent non-conductive $La_2Zr_2O_7$ pyrochlore phase (**Figure B5**) causing drop in Li-ion conductivity below < 0.1 mS cm^{-1}, but had superior theoretical density up to 95% as $La_2Zr_2O_7$ (6.04 g cm^{-3}) phase has high density compared to cubic Al-LLZO phase (5.10 g cm^{-3})

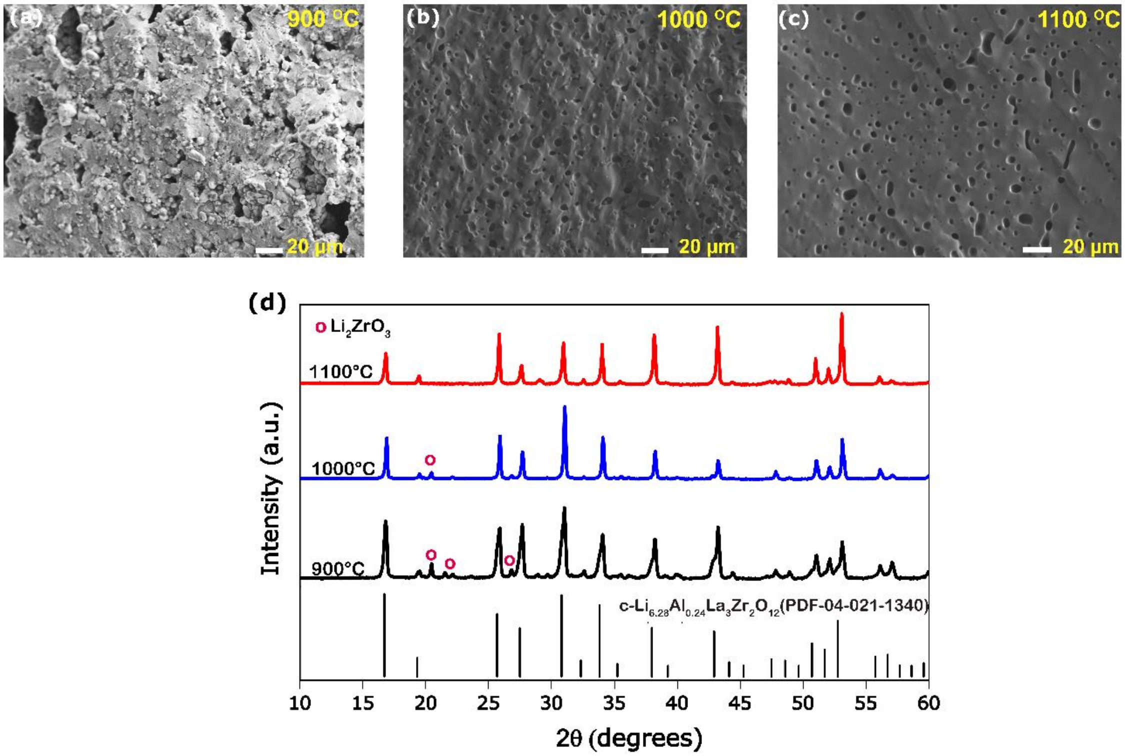

Figure 5. 8. SEM fractured surface images of Al-LLZO pellets sintered at (a) 900 ºC, (b) 1000 ºC, and (c) 1100 ºC, and (d) XRD patterns of the conductive pellets sintered at 900 °C, 1000 °C, and 1100 °C for 6 h (c-$Li_{6.28}Al_{0.24}La_3Zr_2O_{12}$ phase # PDF: 04-021-1340, Li_2ZrO_3 phase PDF # 016-0263 and $La_2Zr_2O_7$ phase # 01-070-5602).

The complex plane impedance patterns of the Al-LLZO pellets sintered under optimal condition (1100 °C, 6 h) recorded from 0 to 60 °C are shown in Figure 6a. At lower temperatures (0 and 20 °C), the impedance spectra show a high-frequency arc representing a resistor connected in parallel to a constant phase element (R || CPE), followed by a strong increase of the imaginary part of the complex impedance towards lower frequencies which is attributed to the ideal ionically blocking electrodes represented by R_e || CPE_e connected in series. In general, the total ionic conductivity in a ceramic conductor is a function of both bulk and grain boundary contributions represented by a distinctive high and mid frequency arc.[116] Based on the capacitance value, $C_i = (R^{1-n} CPE_i)^{1/n}$, where n is a fitting parameter describing deviation from the ideal that is Debye response (n=1), the high frequency arc is assigned to grain boundary processes indicating that the long-range Li^+ transport is dominated by grain boundaries (**Table 5.1**).

Table 5. 1 Equivalent Circuit Fit Parameters, Corresponding Total Conductivities Values at Various Temperatures

Temperatures (°C)	ρ (Ω.cm)	$C_{b,gb(=total)}$ (nF)	$n_{b=total}$	σ_{total} (mS cm^{-1})
0	5215	3.23	0.80	0.2
20	2147	2.2	0.80	0.45
40	1150	0.11	0.73	0.86
60	682	0.10	0.72	1.46

As seen in the **Figure 5.9a**, the arcs shift towards higher frequencies with increasing temperature according to $\omega=1/RC$, where ω is the resonance frequency, due to decreasing resistance. The temperature dependence total Li^+ conductivity ($\sigma_{total} = \sigma_{gb}$) of Al-LLZO pellet sintered at 1100 °C recorded between 0-60 °C is shown using Arrhenius plot in Figure S4. The activation energy E_a for the linear behavior was calculated using $\sigma_{total}T = \sigma_0 \exp(-E_a/(k_B T))$, where k_B is Boltzmann's constant and σ_0 the pre-factor. The activation energy of the Al-LLZO pellet prepared by solution-combustion method was found 0.29 eV, which is lower compared to that by solid-state reaction method and comparable to samples prepared by wet-chemical routes (refer **Table 5.2**). Low values of the activation energy (calculated in the given temperature range) could be attributed to superior grain boundary contacts and excellent sinterability of Al-LLZO powders prepared by solution combustion route.[142,104]

Table 5.2 contains a comparison of the relative density, Li^+ conductivity and activation energy for Al-doped LLZO pellets prepared by various methods in the literature along with the present method. Evidently, carbohydrazide-nitrate solution-combustion is a facile method with a third of the duration necessitated by solid-state reaction method and eliminates elaborated process like multiple calcination /drying steps involved with the wet chemical routes. The pellet densification is also faster without any milling or long sintering durations (>10 h) (see **Table 5.2** for comparisons).

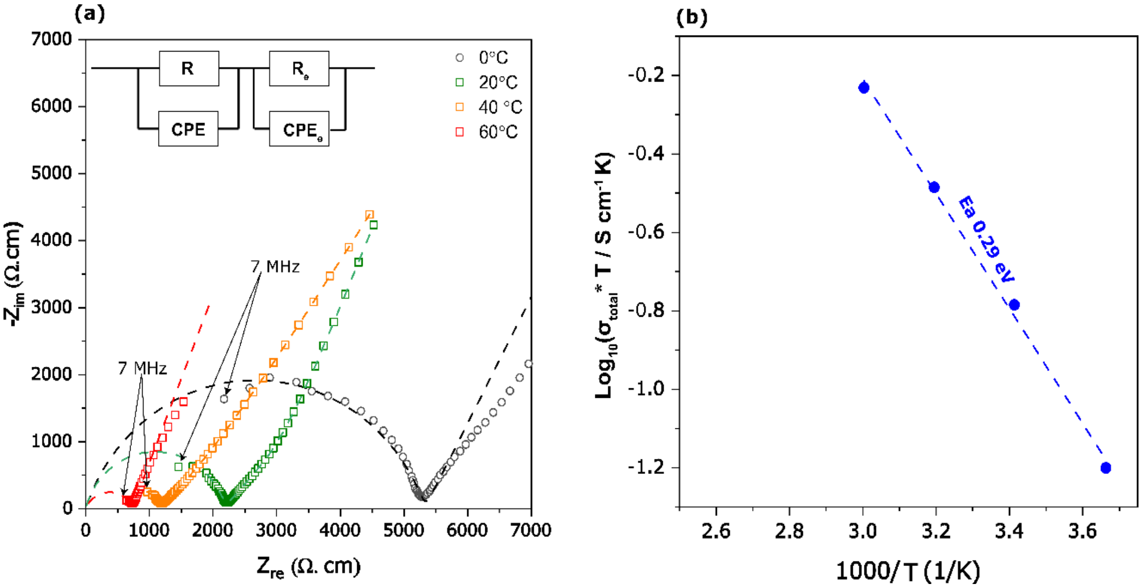

Figure 5. 9. Complex plane temperature-dependent impedance plots (symbols) measured from

(0 to 60 °C) of sintered Al-LLZO pellets along fitted equivalent circuit (dotted lines). *Table*

Table 5. 2 Comparison of Synthesis/Sintering conditions and Properties of the Al-LLZO Prepared by Solution-Combustion Method with the Literature.

Synthesis	Processing conditions	Temperature (°C)	Duration (h)	Relative Density (%)	σ_{total} (mS cm^{-1})	Ea (eV)	Ref
Solid-state[a]	milling (16 h)	900	10	90	0.18	0.41	143
Solid-state[a]	milling (0.5 h)	1000	12	94	0.5	0.29	138
Solid-state[a]	milling (9 h)	600, 800	12, 12	NA	0.14	0.33	144
Modified solid-state	milling (2 h)	70, 100, 200, 750	2, 0.5, 1, 3	91	0.16	0.36	40
Solid-state[a]	milling (12 h)	900	12	96	0.44	0.37	137
Hybrid sol-gel[b]		550-600, 900*	NA, 1	NA	0.3	0.28	142
Pechini		900	6	NA	0.2	NA	54
Pechini[c]		700	2	93	0.18	0.24	145
Sol-gel[c]	gel drying (48 h)	450, 600	4, 4	96	0.4	0.26	51
Co-precipitation	gel ageing (12 h)	600-900	6	96	0.33	0.32	146
Molten salt		900	4	84	0.23	NA	100
Glycine-combustion		950	24	95	0.5	0.29	58
Carbohydrazide - combustion		800	4	92	0.45	0.29	This work
				86	0.2	-	
				75	-	-	

5.5 Conclusions

In summary, submicron sized cubic $Li_{6.28}Al_{0.24}La_3Zr_2O_{12}$ (Al-LLZO) was synthesized by solution-combustion method using carbohydrazide-nitrate mixtures. The presented synthesis route eliminates long ageing/ drying steps, multiple calcination steps usually involved with the wet-chemical route, produces cubic Al-LLZO powders through a single low-temperature calcination step (800 °C, 4 h). The synthesis parameters such as fuel to oxidizer ratio, and calcination temperatures were studied and optimized to produce single-phase cubic Al-LLZO powders without any intermediated phases. The pellets sintered at 1100 ºC for 6 h with 92 % relative density exhibited Li^+ conductivity up to 0.45 mS cm^{-1} at room temperature. The Al-LLZO pellets sintered at 1100 °C showed activation energies of 0.29 eV in the temperature range between (0-60 °C), which were lower compared to those prepared by the solid-state reaction method (0.37 eV) or similar to the values attained by wet-chemical routes. Evidently, the carbohydrazide-nitrate based solution-combustion can be a potential viable method for commercially producing Al-LLZO powders at low temperatures, utilizing inexpensive precursors and less time intensive processing conditions. In addition, access to submicron sized powders using a facile route would provide opportunities for preparing composite high voltage cathodes through co-sintering at lower temperatures and could be used as a low-cost nanoscale LLZO filler for polymer-ceramic composite membranes.

6.0 SUMMARY AND FUTURE WORK

6.1 Summary

The key objective of this work was to develop facile low-temperature synthesis approaches to produce submicron-sized conductive cubic-LLZO powders and improve their processability, microstructure, and Li^+ transport properties. This goal was achieved through molten salt and the solution combustion method. The submicron-sized LLZO powders prepared through molten salt and combustion routes can be widely applied in preparing dense bulk pellets at low sintering temperatures, can also be utilized as inorganic nano-fillers into the polymer matrix to enhance the ionic conductivity of polymer-based electrolytes at room temperatures.

Ta-doped LLZO garnets prepared using the molten salt method at low reaction temperatures (900°C, 5 h) exhibits high Li-ion conductivity (> 0.5 mS cm^{-1}) and relative density (> 96 %) compared to the solid-state reaction method, which requires high reaction temperatures and energy-intensive milling steps to produce conductive garnets. Facile solution combustion synthesis approach was developed to make submicron-sized cubic phase Al-doped LLZO powders at low reaction temperatures of 600 °C for a short duration of 4 h. Sintered pellets exhibited high ionic conductivities (0.45 mS cm^{-1} and relative densities (> 90 %), making them attractive to mass-produce LLZO at a lower cost than the solid-state reaction method.

6.2 Li metal and LLZO Interface Study

6.2.1 Introduction

High interfacial impedance and side reaction at the cathode (metal oxides) and anode (Li) causes poor cyclability and Li metal dendrite growth leading to failure of cells at extremely low current density.[147,148] High Interfacial resistance between LLZO and Li metal is attributed to spontaneous Li^+/ H^+ ions exchange in air and aqueous medium to form Li_2CO_3 passivation, causing poor wettability of Li metal with LLZO surface. Therefore, to mitigate poor contact issues, several promising surface modification strategies are applied, for example, heat treatment (~ 500 °C) of LLZO in an inert atmosphere,[76] use of inexpensive buffer/ interlayers like Au,[105] Graphite,[83] and Sn [88] or even mild acid treatment of LLZO surface with H_3PO_4, HCl. [82,149] improves Li metal and LLZO contacts. Although all the strategies above drastically improve interface contacts and suppress the formation of Li dendrites below (< 0.3 mA cm^{-2}). However, attaining high critical current densities values beyond > 10 mA cm^{-2} using LLZO solid electrolyte remains a challenge. To achieve high CCD values, it is essential to have a homogenous interface to prevent the formation of Li voids at the interface.[150, 151] This chapter provides a baseline or preliminary results on interface resistance between Li metal and LLZTO pellets prepared using the molten salt method along with electrochemical cycling data.

6.2.2 Experimental

Ta-doped LLZO with a nominal composition of $Li_{6.5}La_3Zr_{1.5}Ta_{0.5}O_{12}$ was prepared using the molten salt method as discussed in **Chapter 4**. First, the pellets were sintered until they attain relative density above > 94% using the conventional pressure-less sintering technique. Then, to eliminate any passivation layer formed on the LLZO surface during the pellet's, sintered pellets were transferred into an argon-filled glovebox (H_2O < 1 ppm and O_2 < 1 ppm) for surface treatment. Later, sintered pellets were heat-treated to 250 °C for 30 min using a small box furnace placed inside the glovebox. On cooling, pellets were mechanically polished using 400 grits SiC sandpaper inside the glovebox to remove residual contamination layers. Then, Li metal disc electrodes were punched out from Li ribbon (Millipore Sigma, CAS Number: 7439-93-2) using a 5mm punch set. Finally, the Li metal disc's surface was cleaned using a surgical scalpel until the surface was shiny.

Before assembling Li||LLZO||Li symmetric cell, two different interlayers (a) graphite and (b) Li_3PO_4, were utilized to form good interface contacts. First, a graphite interlayer[83] was introduced on the LLZO surface by mechanical hand drawing using a 2B pencil. Later, Li metal discs were placed on graphite interlayer of the LLZO pellet heated up to 250 °C (beyond the melting point of Li metal) for 30 mins until Li metal was firmly attached to the LLZO surface, as seen in **Figure 6.1**. Similar, Li_3PO_4 layer was formed on treating LLZO pellets with phosphoric acid, as described here.[88] Later, LLZO pellet with Li metal were assembled in a Swelogk cell inside glovebox (see **Figure 6.2**).

Fabricated cells were subjected to EIS measurements using a Biologic SP-200 Potentiostat from 1 MHz to 1 Hz using 10 mV voltage amplitude to ensure ASR values were low enough to carry out DC cycling. Later, cell was cycled at constant current (0.02 mA) test protocol for a duration of 10 h to determine cell stability at room temperatures. To determine CCD values, cells were cycled at starting current density of 0.02 mA cm^{-2} for 60 min, and later current density was increased in steps of 0.03 mA cm^{-2} until the occurrence of a short circuit.

Figure 6. 1. Li metal reacting with graphite interlayer to form Li-C based interface.

Figure 6. 2. In-house fabricated Swagelok type cell for Li||LLZO||Li cycling.

6.2.3 Results and Discussions

EIS measurements carried on the cell consisting of Li metal with the LLZTO pellet without any surface modification) revealed presence of strong semi arc with area specific resistance value of 20,000 Ω.cm^2 as seen in **Figure 6.3** demonstrating poor wettability of Li metal with LLZO surface. In contrast, EIS measurement conducted on LLZO pellet with graphite interlayer (see **Figure 6.4**) showed presence with two separate semi arcs in high frequency and mid frequency region which can be assigned to grain boundaries interface resistance respectively. A significant decrease in the interfacial impedance from 10,000 to 40 Ω.cm^2 was observed on introducing a graphite layer on the surface of LLZO pellets. Improvement in the interface resistance is attributed to formation of LiC_6 layer caused by spontaneous reaction between Li metal and graphite interlayer at 250 °C ($Li + C_6 \rightarrow LiC_6$).[83] On the other hand, LLZO pellets with Li_3PO_4 interlayer also showed lower area specific resistance (77 Ω.cm^2) compared to the cell without any modification as seen in **Figure 6.5**, but higher interface resistance compared to the graphite interlayer. Increase in interface resistance with Li_3PO_4 interlayer could be due to degradation of LLZO surface caused by acid etching and needs further process optimization to attain low interface resistance values as reported in here.[149]

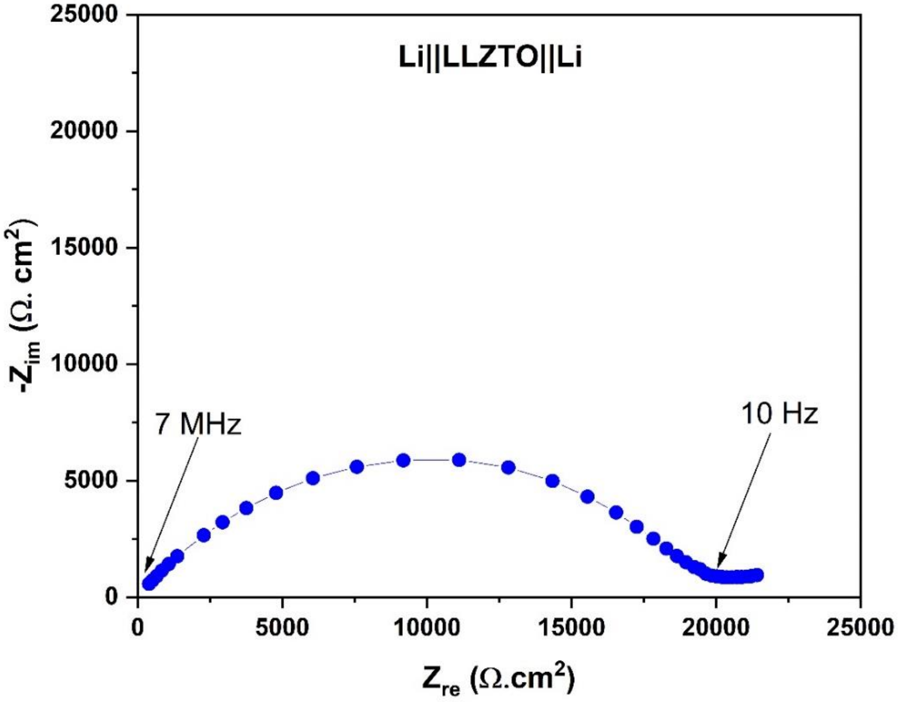

Figure 6. 3. Complex plane plot of the symmetrical Li||LLZTO||Li cell without any interlayer.

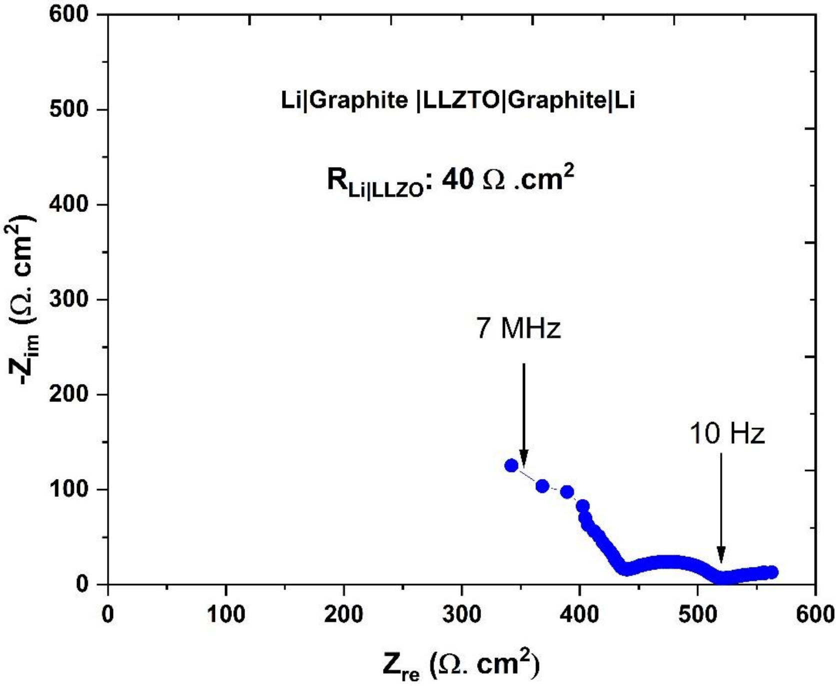

Figure 6. 4. Complex plane plot of the symmetrical Li||LLZTO||Li cell with graphite interlayer.

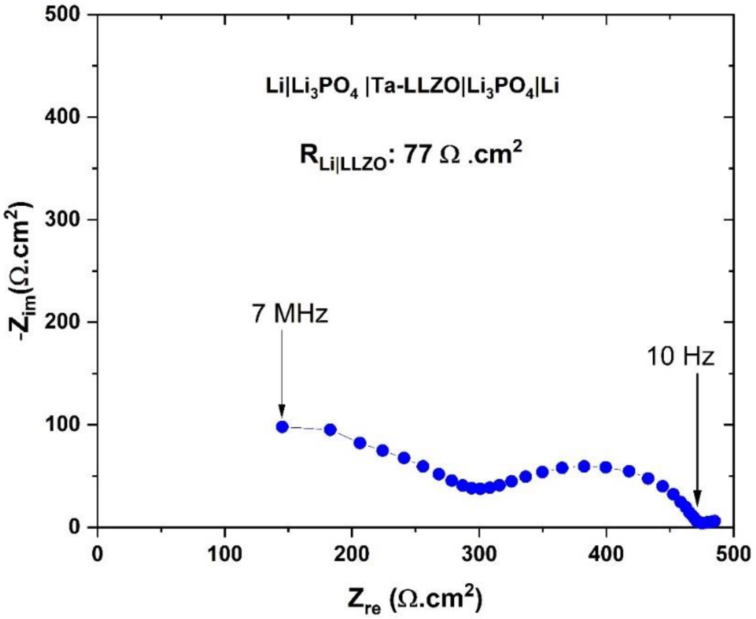

Figure 6. 5. Complex plane plot of the symmetrical Li||LLZTO||Li cell with Li_3PO_4 interlayer.

LLZTO pellets with graphite interlayer were subjected to galvanostatic cycling experiments to evaluated stability and Li-ion transport properties at the interface. As seen in **Figure 6.6,** the plating and stripping of Li at 0.02 mA was quite stable for the first few cycles. A slight deviation in the ohimic behavior was marked by increase in cell voltage response during the 4th and 6th platting and stripping cycles followed by a sudden drop in the cell potential (**Figure 6.6**). Drop in cell voltage 0 V is attributed to soft shorts. [147,150] Later, cells were subjected to critical current density measurements, as they are important to determine endurance level of LLZO electrolyte on Li metal penetration at high current density. Cells were cycled at current densities varying from 0.02 to 0.1 mA.cm^{-2} with 0.03 mA cm^{-2} step increase in current density for every 5 h and each platting/stripping process was maintained for 30 mins (**Figure 6.7**). At low current density values (< 0.05 mA cm^{-2}) near ohmic behavior of voltage response was observed, however on stepping up current density value to 0.1 mA cm^{-2} a strong deviation from the ohmic behavior was seen suggesting current densities exceeds the diffusion limit of Li metal caused by void formation at the interface. The void formation at the interface can lead to localized increase in the current densities, finally sharp drop in voltage to 0 V caused by Li metal dendrite growth through the electrolyte.[152] The natural current density of LLZTO pellet was approximately 0.1 mA cm^{-2} and needs to be further improved by lowering in the interface resistance or by applying some external pressure as demonstrated by other researchers.[153,87]

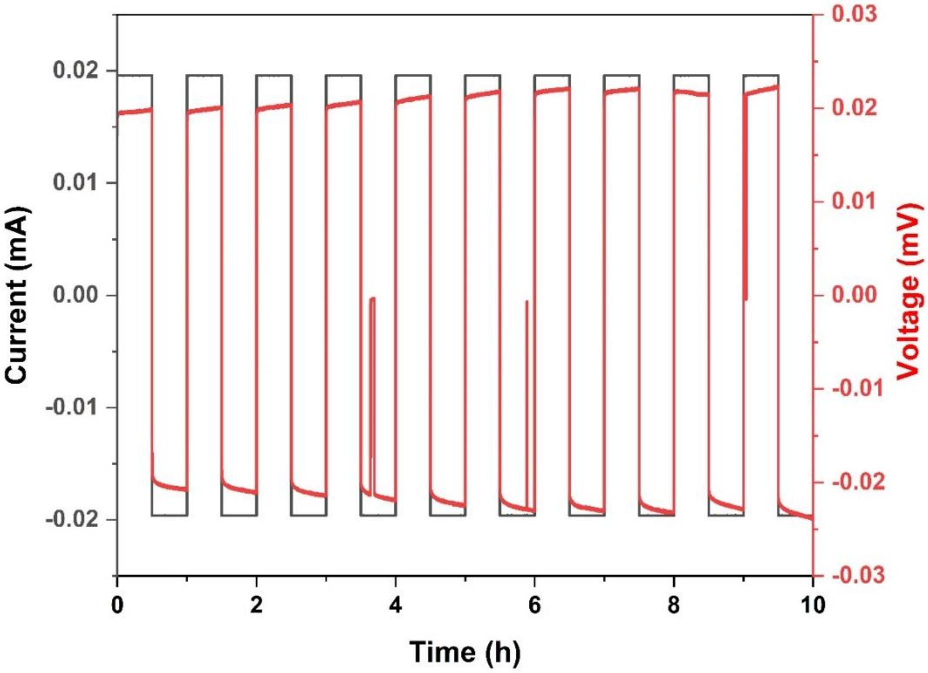

Figure 6.6. Galvanostatic cycling of symmetric Li||LLZTO|| Li cell with graphite interlayer at current of 100 μA cm^{-2}.

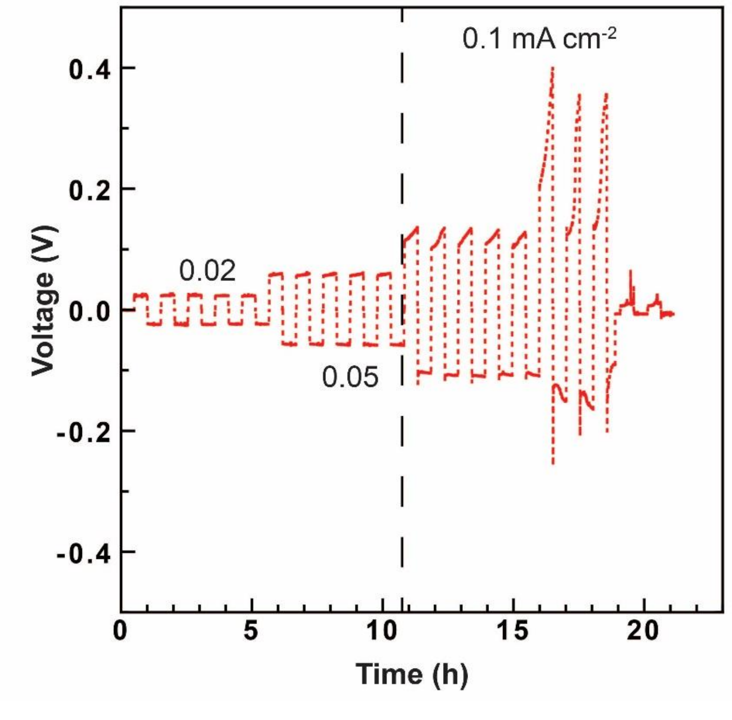

Figure 6.7. Critical current density measurement of Li||LLZTO||Li cell with graphite interlayer cycled at various current densties at room temperature.

6.2.4 Future Work

Based on the extensive synthesis studies and promising results presented in this thesis, it can be concluded that LLZO can be mass-produced at low temperatures with sub-micron particle sizes. There are still many more opportunities to produce LLZO at much low temperatures through pyrochlores ($La_2Zr_2O_7$) and fluorite type (La_3TaO_7) precursors-based approach. Use of pyrochlores or fluorite type precursors have demonstrated lowering formation temperatures (400 – 500 °C) of LLZO through modified solid-state reaction method, molten salt method, or solution combustion method very recently.[154,155,156] On the interface modification side , achieving low interface resistance ($< 20\ \Omega.\ cm^2$) and high critical current densities ($> 5\ mA.cm^{-2}$) for long hours of cycling using a stable interlayer are crucial to implementing LLZO with Li metal anode. The in-situ (operando) characterizations and advanced electrochemical studies using microelectrodes would be essential in answering questions related to non-uniform distribution of current densities and determination of hot spots during the failures of symmetric cells.

REFERENCES

(1) Masson-Delmotte, V.; Zhai, P.; Pörtner, H.-O.; Roberts, D.; Skea, J.; Shukla, P. R.; Pirani, A. *Global Warming of 1.5°C- IPCC Report*; 2018; Vol. 2.

(2) Carbon Pollution from Transportation | US EPA https://www.epa.gov/transportation-air-pollution-and-climate-change/carbon-pollution-transportation#transportation (accessed Jul 18, 2021).

(3) Opitz, A.; Badami, P.; Shen, L.; Vignarooban, K.; Kannan, A. M. Can Li-Ion Batteries Be the Panacea for Automotive Applications? *Renew. Sustain. Energy Rev.* **2017**, *68*.

(4) M. Thackeray, M.; Christopher Wolverton; D. Isaacs, E. Electrical Energy Storage for Transportation—Approaching the Limits of, and Going beyond, Lithium-Ion Batteries. *Energy Environ. Sci.* **2012**, *5*, 7854–7863.

(5) The Electrochemical Society Interface FEATURES And the 2019 Nobel Prize in Chemistry Goes To…. **1901**..

(6) Albertus, P.; Babinec, S.; Litzelman, S.; Newman, A. Status and Challenges in Enabling the Lithium Metal Electrode for High-Energy and Low-Cost Rechargeable Batteries. *Nat. Energy* **2018**, *3*, 16–21.

(7) Wang, C.; Fu, K.; Kammampata, S. P.; McOwen, D. W.; Samson, A. J.; Zhang, L.; Hitz, G. T.; Nolan, A. M.; Wachsman, E. D.; Mo, Y.; Thangadurai, V.; Hu, L. Garnet-Type Solid-State Electrolytes: Materials, Interfaces, and Batteries. *Chem. Rev.* **2020**, 20, 4257-430

(8) Tatsumisago, M.; Hayashi, A. Sulfide Glass-Ceramic Electrolytes for All-Solid-State Lithium and Sodium Batteries. *Int. J. Appl. Glas. Sci.* **2014**, *5*, 226–235.

(9) Kanno, R.; Hata, T.; Kawamoto, Y.; Irie, M. Synthesis of a New Lithium Ionic Conductor, Thio-LISICON-Lithium Germanium Sulfide System. *Solid State Ionics* **2000**, *130*, 97–104.

(10) Kanno, R.; Murayama, M. Lithium Ionic Conductor Thio-LISICON: The Li_2S -GeS_2 - P_2S_5 System. *J. Electrochem. Soc.* **2001**, *148*, A742.

(11) Kato, Y.; Hori, S.; Saito, T.; Suzuki, K.; Hirayama, M.; Mitsui, A.; Yonemura, M.; Iba, H.; Kanno, R. High-Power All-Solid-State Batteries Using Sulfide Superionic Conductors. *Nat. Energy* **2016**, *1*, 16030.

(12) Liu, D.; Zhu, W.; Feng, Z.; Guerfi, A.; Vijh, A.; Zaghib, K. Recent Progress in Sulfide-Based Solid Electrolytes for Li-Ion Batteries. *Mater. Sci. Eng. B Solid-State Mater. Adv. Technol.* **2016**, *213*, 169–176.

(13) Bron, P.; Johansson, S.; Zick, K.; Schmedt auf der Günne, J.; Dehnen, S.; Roling, B. $Li_{10}SnP_2S_{12}$: An Affordable Lithium Superionic Conductor. *J. Am. Chem. Soc.* **2013**, *135*, 15694–15697.

(14) Adachi, G.; Imanaka, N.; Tamura, S. Ionic Conducting Lanthanide Oxides. *Chem. Rev.* **2002**, *102*, 2405–2430.

(15) Ren, Y.; Chen, K.; Chen, R.; Liu, T.; Zhang, Y.; Nan, C. W. Oxide Electrolytes for Lithium Batteries. *J. Am. Ceram. Soc.* **2015**, *98*, 3603–3623.

(16) Lu, J.; Li, Y. Perovskite-type Li-ion Solid Electrolytes: A Review. *Journal of Materials Science: Materials in Electronics*. **2021**, 9736–9754.

(17) Zhu, Y.; He, X.; Mo, Y. Origin of Outstanding Stability in the Lithium Solid Electrolyte Materials: Insights from Thermodynamic Analyses Based on First-Principles Calculations. *ACS Appl. Mater. Interfaces* **2015**, *7*, 23685–23693.

(18) Wolfenstine, J.; Allen, J. L.; Sakamoto, J.; Siegel, D. J.; Choe, H. Mechanical Behavior of Li-Ion-Conducting Crystalline Oxide-Based Solid Electrolytes : A Brief Review. **2018**, 1271–1276.

(19) Zhao, Y.; Daemen, L. L. Superionic Conductivity in Lithium-Rich Anti-Perovskites. *J. Am. Chem. Soc.* **2012**, *134*, 15042–15047.

(20) Li, Y.; Zhou, W.; Xin, S.; Li, S.; Zhu, J.; Lü, X.; Cui, Z.; Jia, Q.; Zhou, J.; Zhao, Y.; Goodenough, J. B. Fluorine-Doped Antiperovskite Electrolyte for All-Solid-State Lithium-Ion Batteries. *Angew. Chemie Int. Ed.* **2016**, *55*, 9965–9968.

(21) Braga, M. H.; Ferreira, J. A.; Stockhausen, V.; Oliveira, J. E.; El-Azab, A. Novel Li_3ClO Based Glasses with Superionic Properties for Lithium Batteries. *J. Mater. Chem. A* **2014**, *2*, 5470–5480.

(22) Hagman, L.-O.; Kierkegaard, P.; Karvonen, P.; Virtanen, A. I.; Paasivirta, J. The Crystal Structure of $NaM_2IV(PO_4)_3$; MeIV = Ge, Ti, Zr. *Acta Chem. Scand.* **1968**, *22*, 1822–1832.

(23) Hong, H. .-P. Crystal Structures and Crystal Chemistry in the System $Na_{1+x}Zr_2Si_xP_{3-x}O_{12}$. *Mater. Res. Bull.* **1976**, *11*, 173–182.

(24) Aono, H.; Sugimoto, E.; Sadaoka, Y.; Imanaka, N.; Adachi, G. Ionic Conductivity of Solid Electrolytes Based on Lithium Titanium Phosphate. *J. Electrochem. Soc.* **1990**, *137*, 1023–1027.

(25) Aono, H.; Sugimoto, E.; Sadaoka, Y.; Imanaka, N.; Adachi, G. Electrical Properties and Sinterability for Lithium Germanium Phosphate $Li_{1+x}M_xGe_{2-x}(PO_4)_3$, M = Al, Cr, Ga, Fe, Sc, and In Systems. *Bull. Chem. Soc. Jpn.* **1992**, *65*, 2200–2204.

(26) Fu, J. Superionic Conductivity of Glass-Ceramics in the System Li_2O-Al_2O_3-TiO_2-P_2O_5. *Solid State Ionics* **1997**, *96*, 195–200.

(27) Hyooma, H.; Hayashi, K. Crystal Structures of $La_3Li_5M_2O_{12}$ (M=Nb, Ta). *Mater. Res. Bull.* **1988**, *23*, 1399–1407.

(28) Thangadurai, V.; Kaack, H.; Weppner, W. J. F. Novel Fast Lithium Ion Conduction in Garnet-Type $Li_5La_3M_2O_{12}$ (M: Nb, Ta). *ChemInform* **2003**, *34* ,

437–440.

(29) Murugan, R.; Thangadurai, V.; Weppner, W. Fast Lithium Ion Conduction in Garnet-Type $Li_7La_3Zr_2O_{12}$. *Angew. Chemie Int. Ed.* **2007**, *46*, 7778–7781.

(30) Awaka, J.; Kijima, N.; Hayakawa, H.; Akimoto, J. Synthesis and Structure Analysis of Tetragonal $Li_7La_3Zr_2O_{12}$ with the Garnet-Related Type Structure. *J. Solid State Chem.* **2009**, *182*, 2046–2052.

(31) Buschmann, H.; Dölle, J.; Berendts, S.; Kuhn, A.; Bottke, P.; Wilkening, M.; Heitjans, P.; Senyshyn, A.; Ehrenberg, H.; Lotnyk, A.; Duppel, V.; Kienle, L.; Janek, J. Structure and Dynamics of the Fast Lithium Ion Conductor "Li $_7La_3Zr_2O_{12}$." *Phys. Chem. Chem. Phys.* **2011**, *13*, 19378–19392.

(32) Rettenwander, D.; Geiger, C. A.; Tribus, M.; Tropper, P.; Amthauer, G. A Synthesis and Crystal Chemical Study of the Fast Ion Conductor $Li_{7-3x}Ga_xLa_3$ Zr_2O_{12} with x = 0.08 to 0.84. *Inorg. Chem.* **2014**, *53*, 6264–6269.

(33) Geiger, C. A.; Alekseev, E.; Lazic, B.; Fisch, M.; Armbruster, T.; Langner, R.; Fechtelkord, M.; Kim, N.; Pettke, T.; Weppner, W. Crystal Chemistry and Stability of "$Li_7La_3Zr_2O_{12}$" Garnet: A Fast Lithium-Ion Conductor. *Inorg. Chem.* **2011**, *50*, 1089–1097.

(34) Li, Y.; Han, J. T.; Wang, C. A.; Xie, H.; Goodenough, J. B. Optimizing Li^+ Conductivity in a Garnet Framework. *J. Mater. Chem.* **2012**, *22*, 15357–15361.

(35) Ohta, S.; Kobayashi, T.; Asaoka, T. High Lithium Ionic Conductivity in the Garnet-Type Oxide Li_{7-X} $La_3(Zr_{2-X}$, $Nb_X)O_{12}$ (X=0–2). *J. Power Sources* **2011**, *196*, 3342–3345.

(36) Li, Y.; Wang, Z.; Cao, Y.; Du, F.; Chen, C.; Cui, Z.; Guo, X. W-Doped $Li_7La_3Zr_2O_{12}$ Ceramic Electrolytes for Solid State Li-Ion Batteries. *Electrochim. Acta* **2015**, *180*, 37–42.

(37) Zhu, Y.; Connell, J. G.; Tepavcevic, S.; Zapol, P.; Garcia-Mendez, R.; Taylor, N. J.; Sakamoto, J.; Ingram, B. J.; Curtiss, L. A.; Freeland, J. W.; Fong, D. D.; Markovic, N. M. Dopant-Dependent Stability of Garnet Solid Electrolyte Interfaces with Lithium Metal. *Adv. Energy Mater.* **2019**, *9*, 1803440.

(38) Monroe, C.; Newman, J. The Impact of Elastic Deformation on Deposition Kinetics at Lithium/Polymer Interfaces. *J. Electrochem. Soc.* **2005**, *152*, A396.

(39) Hu, Z.; Liu, H.; Ruan, H.; Hu, R.; Su, Y.; Zhang, L. High Li-Ion Conductivity of Al-Doped $Li_7La_3Zr_2O_{12}$ Synthesized by Solid-State Reaction. *Ceram. Int.* **2016**, *42*, 12156–12160.

(40) Kumar, P. J.; Nishimura, K.; Senna, M.; Düvel, A.; Heitjans, P.; Kawaguchi, T.; Sakamoto, N.; Wakiya, N.; Suzuki, H. A Novel Low-Temperature Solid-State Route for Nanostructured Cubic Garnet $Li_7La_3Zr_2O_{12}$ and Its Application to Li-Ion Battery. *RSC Adv.* **2016**, *6*, 62656–62667.

(41) Thangadurai, V.; Narayanan, S.; Pinzaru, D. Garnet-Type Solid-State Fast Li Ion

Conductors for Li Batteries: Critical Review. *Chem. Soc. Rev.* **2014**, *43*, 4714–4727.

(42) Tsai, C. L.; Ma, Q.; Dellen, C.; Lobe, S.; Vondahlen, F.; Windmüller, A.; Grüner, D.; Zheng, H.; Uhlenbruck, S.; Finsterbusch, M.; Tietz, F.; Fattakhova-Rohlfing, D.; Buchkremer, H. P.; Guillon, O.; Chih-Long Tsai; Qianli Ma; Christian Dellen; Sandra Lobe; Frank Vondahlen; Anna Windmüller; Daniel Grüner; Hao Zheng; Sven Uhlenbruck; Martin Finsterbusch; Frank Tietz; Dina Fattakhova-Rohlfing; Peter Buchkremer, H.; Olivier Guillon. A Garnet Structure-Based All-Solid-State Li Battery without Interface Modification: Resolving Incompatibility Issues on Positive Electrodes. *Sustain. Energy Fuels* **2019**, *3*, 280–291.

(43) Han, J.; Kim, J. C. A Solid-State Route to Stabilize Cubic $Li_7La_3Zr_2O_{12}$ at Low Temperature for All-Solid-State-Battery Applications. *Chem. Commun.* **2020**, *56*, 15197–15200.

(44) Rangasamy, E.; Wolfenstine, J.; Sakamoto, J. The Role of Al and Li Concentration on the Formation of Cubic Garnet Solid Electrolyte of Nominal Composition $Li_7La_3Zr_2O_{12}$. *Solid State Ionics* **2012**, *206*, 28–32.

(45) Rettenwander, D.; Geiger, C. A.; Amthauer, G. Synthesis and Crystal Chemistry of the Fast Li-Ion Conductor $Li_7La_3Zr_2O_{12}$ Doped with Fe. *Inorg. Chem.* **2013**, *52*, 8005–8009.

(46) Barai, P.; Ngo, A. T.; Narayanan, B.; Higa, K.; Curtiss, L. A.; Srinivasan, V. The Role of Local Inhomogeneities on Dendrite Growth in LLZO-Based Solid Electrolytes. *J. Electrochem. Soc.* **2020**, *167*, 100537.

(47) Huang, X.; Su, J.; Song, Z.; Xiu, T.; Jin, J.; Badding, M. E.; Wen, Z. Synthesis of Ga-Doped $Li_7La_3Zr_2O_{12}$ Solid Electrolyte with High Li^+ Ion Conductivity. *Ceram. Int.* **2021**, *47*, 2123–2130.

(48) Huang, X.; Lu, Y.; Jin, J.; Gu, S.; Xiu, T.; Song, Z.; Badding, M. E.; Wen, Z. Method Using Water-Based Solvent to Prepare $Li_7La_3Zr_2 O_{12}$ Solid Electrolytes. *ACS Appl. Mater. Interfaces*, **2018**, 10, 17147-17155

(49) Livage, J. The Gel Route to Transition Metal Oxides. *J. Solid State Chem.* **1986**, *64*, 322–330.

(50) Danks, A. E.; Hall, S. R.; Schnepp, Z. The Evolution of 'Sol–Gel' Chemistry as a Technique for Materials Synthesis. *Mater. Horizons* **2016**, *3*, 91–112.

(51) Sakamoto, J.; Rangasamy, E.; Kim, H.; Kim, Y.; Wolfenstine, J. Synthesis of Nano-Scale Fast Ion Conducting Cubic $Li_7La_3Zr_2O_{12}$. *Nanotechnology* **2013**, *24* (42).

(52) Shao, C.; Liu, H.; Yu, Z.; Zheng, Z.; Sun, N.; Diao, C. Structure and Ionic Conductivity of Cubic $Li_7La_3Zr_2O_{12}$ Solid Electrolyte Prepared by Chemical Co-Precipitation Method. *Solid State Ionics* **2016**, *287*, 13–16.

(53) Pechini, M. P. Method of Preparing Lead and Alkaline Earth Titanates and Niobates and Coating Method Using the Same to Form a Capacitor. US3330697A,

1967.

(54) Jin, Y.; McGinn, P. J. Al-Doped $Li_7La_3Zr_2O_{12}$ Synthesized by a Polymerized Complex Method. *J. Power Sources* **2011**, *196*, 8683–8687.

(55) Dong, B.; Driscoll, L. L.; Stockham, M. P.; Kendrick, E.; Slater, P. R. Low Temperature Synthesis of Garnet Solid State Electrolytes: Implications on Aluminium Incorporation in $Li_7La_3Zr_2O_{12}$. *Solid State Ionics* **2020**, *350*, 115317.

(56) Rao, C. N. R. Chemical Synthesis of Solid Inorganic Materials. *Mater. Sci. Eng. B* **1993**, *18*, 1–21.

(57) Deganello, F.; Tyagi, A. K. Solution Combustion Synthesis, Energy and Environment: Best Parameters for Better Materials. *Prog. Cryst. Growth Charact. Mater.* **2018**, *64*, 23–61.

(58) Dhivya, L.; Karthik, K.; Ramakumar, S.; Murugan, R. Facile Synthesis of High Lithium Ion Conductive Cubic Phase Lithium Garnets for Electrochemical Energy Storage Devices. *RSC Adv.* **2015**, *5*, 96042–96051. https://doi.org/10.1039/c5ra18543b.

(59) Weller, J. M.; Whetten, J. A.; Chan, C. K. Non-Aqueous Polymer Combustion Synthesis of Cubic $Li_7La_3Zr_2O_{12}$ Nanopowders. *ACS Appl. Mater. Interfaces* **2019**, 953–962.

(60) Badami, P; Smetaczek, S; Limbeck, A; Rettenwander, D; Chan, C. K.; Kannan, A. N Facile Synthesis of Al-Stabilized Lithium Garnets by a Solution-Combustion Technique for All Solid-State Batteries. *Mater. Adv*. **2021**.

(61) Badami, P. P.; Arif, M. Z.; Rettenwander, D.; Chan, C. K.; Kannan, A. M. Synthesis of $Li_7La_3Zr_2O_{12}$ Li-Ion Conducting Electrolytes By a Rapid Solution-Combustion Method. *ECS Meet. Abstr.* **2020**, *MA2020-02* (5), 941.

(62) Boltersdorf, J; King, N; Maggard, P.A.Flux-Mediated Crystal Growth of Metal Oxides: Synthetic Tunability of Particle Morphologies, Sizes, and Surface Features for Photocatalysis Research. *CrystEngComm*, **2015,** 17, 2225-2241

(63) Reddy, M. V; Adams, S. Molten Salt Synthesis and Characterization of Fast Ion Conductor. Journal of Solid State Electrochemistry, **2017**, 21, 2921-2928.

(64) Larraz, G.; Orera, A.; Sanjuán, M. L. Cubic Phases of Garnet-Type $Li_7La_3Zr_2O_{12}$: The Role of Hydration. *J. Mater. Chem. A* **2013**, *1*, 11419–11428.

(65) Redhammer, G. J.; Badami, P.; Meven, M.; Ganschow, S.; Berendts, S.; Tippelt, G.; Rettenwander, D. Wet-Environment-Induced Structural Alterations in Single- And Polycrystalline LLZTO Solid Electrolytes Studied by Diffraction Techniques. *ACS Appl. Mater. Interfaces* **2021,** 13, 350-359.

(66) Brugge, R. H.; Hekselman, A. K. O.; Cavallaro, A.; Pesci, F. M.; Chater, R. J.; Kilner, J. A.; Aguadero, A. Garnet Electrolytes for Solid State Batteries: Visualization of Moisture-Induced Chemical Degradation and Revealing Its Impact on the Li-Ion Dynamics. *Chem. Mater.* **2018**, *30*, 3704–3713.

(67) Liu, X.; Chen, Y.; Hood, Z. D.; Ma, C.; Yu, S.; Sharafi, A.; Wang, H.; An, K.; Sakamoto, J.; Siegel, D. J.; Cheng, Y.; Jalarvo, N. H.; Chi, M. Elucidating the Mobility of H^+ and Li^+ Ions in $(Li_{6.25-X}H_xAl_{0.25})La_3Zr_2O_{12}$ via Correlative Neutron and Electron Spectroscopy. *Energy Environ. Sci.* **2019**, *12*, 945–951.

(68) Grissa, R.; Payandeh, S.; Heinz, M.; Battaglia, C. Impact of Protonation on the Electrochemical Performance of $Li_7La_3Zr_2O_{12}$ Garnets. *ACS Appl. Mater. Interfaces* **2021**, *13*, 14700–14709.

(69) Cheng, M.; Rangasamy, E.; Liang, C.; Sakamoto, J.; More, K. L.; Chi, M. Excellent Stability of a Lithium-Ion-Conducting Solid Electrolyte upon Reversible Li^+/H^+ Exchange in Aqueous Solutions. *Angew. Chemie - Int. Ed.* **2015**, *54*, 129–133.

(70) Galven, C.; Fourquet, J. L.; Crosnier-Lopez, M. P.; Le Berre, F. Instability of the Lithium Garnet $Li_7La_3Sn_2O_{12}$: Li^+ /H^+ Exchange and Structural Study. *Chem. Mater.* **2011**, *23*, 1892–1900.

(71) Hiebl, C.; Young, D.; Wagner, R.; Wilkening, H. M. R.; Redhammer, G. J.; Rettenwander, D. Proton Bulk Diffusion in Cubic $Li_7La_3Zr_2O_{12}$ Garnets as Probed by Single X-Ray Diffraction. *J. Phys. Chem. C* **2019**, *123*, 1094–1098.

(72) Cheng, M.; Rangasamy, E.; Liang, C.; Sakamoto, J.; More, K. L.; Chi, M.; Ma, C.; Rangasamy, E.; Liang, C.; Sakamoto, J.; More, K. L.; Chi, M. Excellent Stability of a Lithium-Ion-Conducting Solid Electrolyte upon Reversible Li^+/H^+ Exchange in Aqueous Solutions. *Angew. Chemie - Int. Ed.* **2015**, *54*, 129–133.

(73) Cheng, L.; Liu, M.; Mehta, A.; Xin, H.; Lin, F.; Persson, K.; Chen, G.; Crumlin, E. J.; Doeff, M. Garnet Electrolyte Surface Degradation and Recovery. *ACS Applied Energy Materials*, **2018**, 1,7244-7252.

(74) Rosen, M.; Ye, R.; Mann, M.; Lobe, S.; Finsterbusch, M.; Guillon, O.; Fattakhova-Rohlfing, D. Controlling the Lithium Proton Exchange of LLZO to Enable Reproducible Processing and Performance Optimization *Journal of Materials Chemistry A*, **2021**, 8, 4831-4840.

(75) Huo, H.; Luo, J.; Thangadurai, V.; Guo, X.; Nan, C.-W.; Sun, X. Li_2CO_3 : A Critical Issue for Developing Solid Garnet Batteries. *ACS Energy Lett.* **2020**, *5*, 252–262.

(76) Sharafi, A.; Kazyak, E.; Davis, A. L.; Yu, S.; Thompson, T.; Siegel, D. J.; Dasgupta, N. P.; Sakamoto, J. Surface Chemistry Mechanism of Ultra-Low Interfacial Resistance in the Solid-State Electrolyte $Li_7La_3Zr_2O_{12}$. *Chem. Mater.* **2017**, *29* , 7961–7968.

(77) Li, Y.; Chen, X.; Dolocan, A.; Cui, Z.; Xin, S.; Xue, L.; Xu, H.; Park, K.; Goodenough, J. B. Garnet Electrolyte with an Ultralow Interfacial Resistance for Li-Metal Batteries. *J. Am. Chem. Soc.* **2018**, *140*, 6448–6455.

(78) Li, Y.; Xu, B.; Xu, H.; Duan, H.; Lü, X.; Xin, S.; Zhou, W.; Xue, L.; Fu, G.; Manthiram, A.; Goodenough, J. B. Hybrid Polymer/Garnet Electrolyte with a

Small Interfacial Resistance for Lithium-Ion Batteries. *Angew. Chemie - Int. Ed.* **2017**, *56* , 753–756.

(79) Wu, J.-F.; Pu, B.-W.; Wang, D.; Shi, S.-Q.; Zhao, N.; Guo, X.; Guo, X. In Situ Formed Shields Enabling Li_2CO_3 -Free Solid Electrolytes: A New Route to Uncover the Intrinsic Lithiophilicity of Garnet Electrolytes for Dendrite-Free Li-Metal Batteries. *ACS Appl. Mater. Interfaces* **2019**, *11*, 898–905.

(80) Huo, H.; Chen, Y.; Zhao, N.; Lin, X.; Luo, J.; Yang, X.; Liu, Y.; Guo, X.; Sun, X. In-Situ Formed Li_2CO_3-Free Garnet/Li Interface by Rapid Acid Treatment for Dendrite-Free Solid-State Batteries. *Nano Energy* **2019**, *61*, 119–125.

(81) Xu, J.; Tian, W.; Lu, K.; Shan, S.; Zhang, J.; Wu, Y.; Wu, M.; Tang, W. Effect of Acid Treatment of $Li_7La_3Zr_2O_{12}$ on Ionic Conductivity of Composite Solid Electrolytes. *IOP Conf. Ser. Earth Environ. Sci.* **2020**, *512*, 012110.

(82) Motoyama, M.; Tanaka, Y.; Yamamoto, T.; Tsuchimine, N.; Kobayashi, S.; Iriyama, Y. The Active Interface of Ta-Doped $Li_7La_3Zr_2O_{12}$ for Li Plating/Stripping Revealed by Acid Aqueous Etching. *ACS Appl. Energy Mater.* **2019**, *2*, 6720–6731.

(83) Shao, Y.; Wang, H.; Gong, Z.; Wang, D.; Zheng, B.; Zhu, J.; Lu, Y.; Hu, Y.-S.; Guo, X.; Li, H.; Huang, X.; Yang, Y.; Nan, C.-W.; Chen, L. Drawing a Soft Interface: An Effective Interfacial Modification Strategy for Garnet-Type Solid-State Li Batteries. *ACS Energy Lett.* **2018**, *3*, 1212–1218.

(84) Han, X.; Gong, Y.; Fu, K.; He, X.; Hitz, G. T.; Dai, J.; Pearse, A.; Liu, B.; Wang, H.; Rubloff, G.; Mo, Y.; Thangadurai, V.; Wachsman, E. D.; Hu, L. Negating Interfacial Impedance in Garnet-Based Solid-State Li Metal Batteries. *Nat. Mater.* **2017**, *16*, 572–579.

(85) Sharafi, A.; Meyer, H. M.; Nanda, J.; Wolfenstine, J.; Sakamoto, J. Characterizing the Li–$Li_7La_3Zr_2O_{12}$ Interface Stability and Kinetics as a Function of Temperature and Current Density. *J. Power Sources* **2016**, *302*, 135–139.

(86) Wang, M. J.; Choudhury, R.; Sakamoto, J. Characterizing the Li-Solid-Electrolyte Interface Dynamics as a Function of Stack Pressure and Current Density. *Joule* **2019**, *3*, 2165–2178.

(87) Duan, J.; Wu, W.; Nolan, A. M.; Wang, T.; Wen, J.; Hu, C.; Mo, Y.; Luo, W.; Huang, Y. Lithium-Graphite Paste: An Interface Compatible Anode for Solid-State Batteries. *Adv. Mater.* **2019**, *31*, 1807243.

(88) He, M.; Cui, Z.; Chen, C.; Li, Y.; Guo, X. Formation of Self-Limited, Stable and Conductive Interfaces between Garnet Electrolytes and Lithium Anodes for Reversible Lithium Cycling in Solid-State Batteries. *J. Mater. Chem. A* **2018**, *6*, 11463–11470.

(89) Fu, K. K.; Gong, Y.; Fu, Z.; Xie, H.; Yao, Y.; Liu, B.; Carter, M.; Wachsman, E.; Hu, L. Transient Behavior of the Metal Interface in Lithium Metal-Garnet Batteries. *Angew. Chemie Int. Ed.* **2017**, *56*, 14942–14947.

(90) HighScore Plus | XRD Analysis Software | Malvern Panalytical https://www.malvernpanalytical.com/en/products/category/software/x-ray-diffraction-software/highscore-with-plus-option (accessed Aug 8, 2021).

(91) Scanning Electron Microscopy (SEM) https://serc.carleton.edu/research_education/geochemsheets/techniques/SEM.html (accessed Jul 27, 2021).

(92) Smetaczek, S.; Bonta, M.; Wachter-Welzl, A.; Taibl, S.; Wagner, R.; Rettenwander, D.; Fleig, J.; Limbeck, A. Spatially Resolved Stoichiometry Determination of $Li_7La_3Zr_2O_{12}$ Solid-State Electrolytes Using LA-ICP-OES. *J. Anal. At. Spectrom.* **2020**, *35*, 972–983.

(93) Chen, Q.; Liu, W.; Wang, W. J.; Thomas, J. C.; Shen, J. Particle Sizing by the Fraunhofer Diffraction Method Based on an Approximate Non-Negatively Constrained Chin-Shifrin Algorithm. *Powder Technol.* **2017**, *317*, 95–103.

(94) Zhang, Y.; Zuo, T.-T.; Popovic, J.; Lim, K.; Yin, Y.-X.; Maier, J.; Guo, Y.-G. Towards Better Li Metal Anodes: Challenges and Strategies. *Mater. Today* **2020**, *33*, 56–74.

(95) Krasnikova, I. V; Pogosova, M. A.; Sanin, A. O.; Stevenson, K. J. Toward Standardization of Electrochemical Impedance Spectroscopy Studies of Li-Ion Conductive Ceramics. **2020**.

(96) Jin, Y.; McGinn, P. J. Al-Doped $Li_7La_3Zr_2O_{12}$ Synthesized by a Polymerized Complex Method. *J. Power Sources* **2011**, *196*, 8683–8687.

(97) Kakihana, M. Synthesis of High-Performance Ceramics Based on Polymerizable Complex Method. *Journal of the Ceramic Society of Japan*, **2009**, 117, 857-862.

(98) Afyon, S.; Krumeich, F.; Rupp, J. L. M. A Shortcut to Garnet-Type Fast Li-Ion Conductors for All-Solid State Batteries. *J. Mater. Chem. A* **2015**, *3*, 18636–18648.

(99) Afanasiev, P.; Geantet, C. Synthesis of Solid Materials in Molten Nitrates. *Coord. Chem. Rev.* **1998**, *178–180*, 1725–1752.

(100) Weller, J. M.; Whetten, J. A.; Chan, C. K. Synthesis of Fine Cubic $Li_7La_3Zr_2O_{12}$ Powders in Molten LiCl-KCl Eutectic and Facile Densification by Reversal of Li^+/H^+ Exchange. *ACS Appl. Energy Mater.* **2018**, *1*, 552–560.

(101) Liu, X.; Fechler, N.; Antonietti, M. Salt Melt Synthesis of Ceramics, Semiconductors and Carbon Nanostructures. *Chem. Soc. Rev.* **2013**, *42*, 8237–8265.

(102) ZView® For Windows - Scribner Associates https://www.scribner.com/software/68-general-electrochemistr376-zview-for-windows/ (accessed Jul 31, 2021).

(103) Ren, Y.; Deng, H.; Chen, R.; Shen, Y.; Lin, Y.; Nan, C. W. Effects of Li Source on Microstructure and Ionic Conductivity of Al-Contained $Li_{6.75}La_3Zr_{1.75}Ta_{0.25}O_{12}$

Ceramics. *J. Eur. Ceram. Soc.* **2015**, *35*, 561–572.

(104) Yi, E.; Wang, W.; Kieffer, J.; Laine, R. M. Flame Made Nanoparticles Permit Processing of Dense, Flexible, Li^+ Conducting Ceramic Electrolyte Thin Films of Cubic-$Li_7La_3Zr_2O_{12}$ (c-LLZO). *J. Mater. Chem. A* **2016**, *4*, 12947–12954.

(105) Tsai, C.-L.; Roddatis, V.; Chandran, C. V.; Ma, Q.; Uhlenbruck, S.; Bram, M.; Heitjans, P.; Guillon, O. $Li_7La_3Zr_2O_{12}$ Interface Modification for Li Dendrite Prevention. *ACS Appl. Mater. Interfaces* **2016**, *8* , 10617–10626.

(106) Hongahally Basappa, R.; Ito, T.; Morimura, T.; Bekarevich, R.; Mitsuishi, K.; Yamada, H. Grain Boundary Modification to Suppress Lithium Penetration through Garnet-Type Solid Electrolyte. *J. Power Sources* **2017**, *363*, 145–152.

(107) Kulkarni, N. S.; Besmann, T. M.; Spear, K. E. Thermodynamic Optimization of Lithia–Alumina. *J. Am. Ceram. Soc.* **2008**, *91*, 4074–4083.

(108) Yow, Z. F.; Oh, Y. L.; Gu, W.; Rao, R. P.; Adams, S. Effect of Li^+ / H^+ Exchange in Water Treated Ta-Doped $Li_7La_3Zr_2O_{12}$. *Solid State Ionics* **2016**, *292*, 122–129.

(109) Hubaud, A. A.; Schroeder, D. J.; Key, B.; Ingram, B. J.; Dogan, F.; Vaughey, J. T. Low Temperature Stabilization of Cubic $(Li_{7-X}Al_{x/3})La_3Zr_2O_{12}$: Role of Aluminum during Formation. *J. Mater. Chem. A* **2013**, *1*, 8813–8818.

(110) Düvel, A.; Kuhn, A.; Robben, L.; Wilkening, M.; Heitjans, P. Mechanosynthesis of Solid Electrolytes: Preparation, Characterization, and Li Ion Transport Properties of Garnet-Type Al-Doped $Li_7La_3Zr_2O_{12}$ Crystallizing with Cubic Symmetry. *J. Phys. Chem. C* **2012**, *116* , 15192–15202.

(111) German, R. M. Sintering: From Empirical Observations to Scientific Principles , 1. **2014**, 2014.

(112) Huang, X.; Lu, Y.; Song, Z.; Rui, K.; Wang, Q.; Xiu, T.; Badding, M. E.; Wen, Z. Manipulating Li2O Atmosphere for Sintering Dense $Li_7La_3Zr_2O_{12}$ Solid Electrolyte. *Energy Storage Mater.* **2019**, *22*, 207–217.

(113) Ahn, J. H.; Park, S.-Y.; Lee, J.-M.; Park, Y.; Lee, J.-H. Local Impedance Spectroscopic and Microstructural Analyses of Al-in-Diffused $Li_7La_3Zr_2O1_2$. *J. Power Sources* **2014**, *254*, 287–292.

(114) Huang, X.; Lu, Y.; Guo, H.; Song, Z.; Xiu, T.; Badding, M. E.; Wen, Z. None-Mother-Powder Method to Prepare Dense Li-Garnet Solid Electrolytes with High Critical Current Density. *ACS Appl. Energy Mater.* **2018**, *1*, 5355–5365.

(115) La, H. L.; Garnet, Z. O.; Tenhaeff, W. E.; Rangasamy, E.; Wang, Y.; Sokolov, A. P.; Wolfenstine, J.; Sakamoto, J.; Dudney, N. J. Resolving the Grain Boundary and Lattice Impedance Of. **2014**, 375–378.

(116) Irvine, J. T. S.; Sinclair, D. C.; West, A. R. Electroceramics: Characterization by Impedance Spectroscopy. *Adv. Mater.* **1990**, *2*, 132–138.

(117) Kotobuki, M.; Kanamura, K.; Sato, Y.; Yoshida, T. Fabrication of All-Solid-State

Lithium Battery with Lithium Metal Anode Using Al_2O_3-Added $Li_7La_3Zr_2O_{12}$ Solid Electrolyte. *J. Power Sources* **2011**, *196* , 7750–7754.

(118) Rettenwander, D.; Redhammer, G.; Preishuber-Pflügl, F.; Cheng, L.; Miara, L.; Wagner, R.; Welzl, A.; Suard, E.; Doeff, M. M.; Wilkening, M.; Fleig, J.; Amthauer, G. Structural and Electrochemical Consequences of Al and Ga Cosubstitution in $Li_7La_3Zr_2O_{12}$ Solid Electrolytes. Chem. Mater. 2016, 28, 2384–2392

(119) Du, F.; Zhao, N.; Li, Y.; Chen, C.; Liu, Z.; Guo, X. All Solid State Lithium Batteries Based on Lamellar Garnet-Type Ceramic Electrolytes. *J. Power Sources* **2015**, *300*, 24–28.

(120) Wang, Y.; Yan, P.; Xiao, J.; Lu, X.; Zhang, J.; Sprenkle, V. L. Effect of Al_2O_3 on the Sintering of Garnet-Type $Li_{6.5}La_3Zr_{1.5}Ta_{0.5}O_{12}$. *Solid State Ionics,* 2016, 294, 108–115.

(121) Yamada, H.; Ito, T.; Hongahally Basappa, R. Sintering Mechanisms of High-Performance Garnet-Type Solid Electrolyte Densified by Spark Plasma Sintering. *Electrochim. Acta* **2016**, *222*, 648–656.

(122) Thompson, T.; Sharafi, A.; Johannes, M. D.; Huq, A.; Allen, J. L.; Wolfenstine, J.; Sakamoto, J. A Tale of Two Sites : On Defining the Carrier Concentration in Garnet-Based Ionic Conductors for Advanced Li Batteries. *Advanced Energy Materials*, **2015**,1500096

(123) Varma, A.; Mukasyan, A. S.; Rogachev, A. S.; Manukyan, K. V. Solution Combustion Synthesis of Nanoscale Materials. *Chem. Rev.* **2016**, *116*, 14493–14586.

(124) Pratsinis, S. E. Flame Aerosol Synthesis of Ceramic Powders. *Prog. Energy Combust. Sci.* **1998**, *24*, 197–219.

(125) Koirala, R.; Pratsinis, S. E.; Baiker, A. Synthesis of Catalytic Materials in Flames: Opportunities and Challenges. *Chem. Soc. Rev* **2016**, *45*, 3053.

(126) Jain, S. R.; Adiga, K. C.; Pai Verneker, V. R. A New Approach to Thermochemical Calculations of Condensed Fuel-Oxidizer Mixtures. *Combust. Flame* **1981**, *40* (C), 71–79.

(127) Li, F. T.; Ran, J.; Jaroniec, M.; Qiao, S. Z. Solution Combustion Synthesis of Metal Oxide Nanomaterials for Energy Storage and Conversion. *Nanoscale* **2015**, *7* (42), 17590–17610.

(128) Aruna, S. T.; Patil, K. C. Combustion Synthesis and Properties of Nanostructured Ceria-Zirconia Solid Solutions. *Nanostructured Mater.* **1998**, *10*, 955–964.

(129) Mimani, T. Instant Synthesis of Nanoscale Spinel Aluminates. *J. Alloys Compd.* **2001**, *315* , 123–128.

(130) Rao, G. R.; Mishra, B. G.; Sahu, H. R. Synthesis of CuO, Cu and CuNi Alloy Particles by Solution Combustion Using Carbohydrazide and N-Tertiarybutoxy-

Carbonylpiperazine Fuels. *Mater. Lett.* **2004**, *58*, 3523–3527.

(131) González-Cortés, S. L.; Imbert, F. E. Fundamentals, Properties and Applications of Solid Catalysts Prepared by Solution Combustion Synthesis (SCS). *Appl. Catal. A Gen.* **2013**, *452*, 117–131.

(132) Sutka, A.; Mezinskis, G. Sol-Gel Auto-Combustion Synthesis of Spinel-Type Ferrite Nanomaterials. *Front. Mater. Sci.* **2012**, *6*, 128–141.

(133) Salunkhe, A. B.; Khot, V. M.; Phadatare, M. R.; Pawar, S. H. Combustion Synthesis of Cobalt Ferrite Nanoparticles - Influence of Fuel to Oxidizer Ratio. *J. Alloys Compd.* **2012**, *514*, 91–96.

(134) Schmidt, R. D.; Sakamoto, J. In-Situ, Non-Destructive Acoustic Characterization of Solid State Electrolyte Cells. *J. Power Sources* **2016**, *324*, 126–133.

(135) Hwang, B. J.; Santhanam, R.; Liu, D. G. Effect of Various Synthetic Parameters on Purity of $LiMn_2O_4$ Spinel Synthesized by a Sol-Gel Method at Low Temperature. *J. Power Sources* **2001**, *101*, 86–89.

(136) Deraz, N. M. Glycine-Assisted Fabrication of Nanocrystalline Cobalt Ferrite System. *J. Anal. Appl. Pyrolysis* **2010**, *88* , 103–109.

(137) Xia, W.; Xu, B.; Duan, H.; Guo, Y.; Kang, H.; Li, H.; Liu, H. Ionic Conductivity and Air Stability of Al-Doped $Li_7La_3Zr_2O_{12}$ Sintered in Alumina and Pt Crucibles. *ACS Appl. Mater. Interfaces* **2016**, *8*, 5335–5342.

(138) Cheng, L.; Park, J. S.; Hou, H.; Zorba, V.; Chen, G.; Richardson, T.; Cabana, J.; Russo, R.; Doeff, M. Effect of Microstructure and Surface Impurity Segregation on the Electrical and Electrochemical Properties of Dense Al-Substituted $Li_7La_3Zr_2O_{12}$. *J. Mater. Chem. A* **2014**, *2*, 172–181.

(139) Yi, E.; Wang, W.; Kieffer, J.; Laine, R. M. Key Parameters Governing the Densification of Cubic-$Li_7La_3Zr_2O_{12}$ Li^+ Conductors. *J. Power Sources* **2017**, *352*, 156–164.

(140) Cheng, L.; Chen, W.; Kunz, M.; Persson, K.; Tamura, N.; Chen, G.; Doeff, M. Effect of Surface Microstructure on Electrochemical Performance of Garnet Solid Electrolytes. *ACS Appl. Mater. Interfaces* **2015**, *7*, 2073–2081.

(141) Badami, P.; Weller, J. M.; Wahab, A.; Redhammer, G.; Ladenstein, L.; Rettenwander, D.; Wilkening, M.; Chan, C. K.; Kannan, A. N. M. Highly Conductive Garnet-Type Electrolytes: Access to $Li_{6.5}La_3Zr_{1.5}Ta_{0.5}O_{12}$ Prepared by Molten Salt and Solid-State Methods. *ACS Appl. Mater. Interfaces* **2020**, *12*, 48580–48590.

(142) El-Shinawi, H.; Paterson, G. W.; MacLaren, D. A.; Cussen, E. J.; Corr, S. A. Low-Temperature Densification of Al-Doped $Li_7La_3Zr_2O_{12}$: A Reliable and Controllable Synthesis of Fast-Ion Conducting Garnets. *J. Mater. Chem. A* **2017**, *5*, 319–329.

(143) Chen, C.; Sun, Y.; He, L.; Kotobuki, M.; Hanc, E.; Chen, Y.; Zeng, K.; Lu, L.

Microstructural and Electrochemical Properties of Al- And Ga-Doped $Li_7La_3Zr_2O_{12}$ Garnet Solid Electrolytes. *ACS Appl. Energy Mater.* **2020**, *3*, 4708–4719.

(144) Vardar, G.; Bowman, W.J.; Lu, Q.; Wang, J.; Chater, R.J.; Aguadero, A.; Seibert, R., Terry; J., Hunt; A., Waluyo; I. Fong, D.D. Structure, chemistry, and charge transfer resistance of the interface between $Li_7La_3Zr_2O_{12}$ electrolyte and $LiCoO_2$ cathode. *Chemistry of Materials*. **2018**, 30, 6259-6276.

(145) Avila, V.; Yoon, B.; Ghose, S.; Raj, R.; Jesus, L. M. Phase Evolution during Reactive Flash Sintering of $Li_{6.25}Al_{0.25}La_3Zr_2O_{12}$ Starting from a Chemically Prepared Powder. *J. Eur. Ceram. Soc.* **2021**, 2–7.

(146) Zhang, Y.; Cai, J.; Chen, F.; Tu, R.; Shen, Q.; Zhang, X.; Zhang, L. Preparation of Cubic $Li_7La_3Zr_2O_{12}$ Solid Electrolyte Using a Nano-Sized Core-Shell Structured Precursor. *J. Alloys Compd.* **2015**, *644*, 793–798.

(147) Flatscher, F.; Philipp, M.; Ganschow, S.; Wilkening, H. M. R.; Rettenwander, D. The Natural Critical Current Density Limit for $Li_7La_3Zr_2O_{12}$ Garnets. *J. Mater. Chem. A* **2020**, *8*, 15782–15788.

(148) Chih-Long Tsai; Qianli Ma; Christian Dellen; Sandra Lobe; Frank Vondahlen; Anna Windmüller; Daniel Grüner; Hao Zheng; Sven Uhlenbruck; Martin Finsterbusch; Frank Tietz; Dina Fattakhova-Rohlfing; Peter Buchkremer, H.; Olivier Guillon. A Garnet Structure-Based All-Solid-State Li Battery without Interface Modification: Resolving Incompatibility Issues on Positive Electrodes. *Sustain. Energy Fuels* **2018**, *3,* 280–291.

(149) Ruan, Y.; Lu, Y.; Huang, X.; Su, J.; Sun, C.; Jin, J.; Wen, Z. Acid Induced Conversion towards a Robust and Lithiophilic Interface for Li–$Li_7La_3Zr_2O_{12}$ Solid-State Batteries. *J. Mater. Chem. A* **2019**, *7*, 14565–14574.

(150) Kasemchainan, J.; Zekoll, S.; Spencer Jolly, D.; Ning, Z.; Hartley, G. O.; Marrow, J.; Bruce, P. G. Critical Stripping Current Leads to Dendrite Formation on Plating in Lithium Anode Solid Electrolyte Cells. *Nat. Mater.* **2019**, *18*, 1105–1111.

(151) Porz, L.; Swamy, T.; Sheldon, B. W.; Rettenwander, D.; Frömling, T.; Thaman, H. L.; Berendts, S.; Uecker, R.; Carter, W. C.; Chiang, Y. M. Mechanism of Lithium Metal Penetration through Inorganic Solid Electrolytes. *Adv. Energy Mater.* **2017**, *7,* 1701003.

(152) Krauskopf, T.; Hartmann, H.; Zeier, W. G.; Janek, J. Toward a Fundamental Understanding of the Lithium Metal Anode in Solid-State Batteries—An Electrochemo-Mechanical Study on the Garnet-Type Solid Electrolyte $Li_{6.25}Al_{0.25}La_3Zr_2O_{12}$. *ACS Appl. Mater. Interfaces* **2019**, *11,* 14463–14477.

(153) Sakamoto, J. More Pressure Needed. *Nat. Energy* **2019**, *4* , 827–828.

(154) Hamao, N.; Hamamoto, K.; Taguchi, N.; Tanaka, S.; Akimoto, J. Synthesis and Crystal Structure of Fluorite-Type $La_{2.4}Zr_{1.2}Ta_{0.4}O_7$: A Precursor Oxide for Low Temperature Formation of Garnet-Type $Li_{6.5}La_3Zr_{1.5}Ta_{0.5}O_{12}$. *Solid State Ionics*

2020, *357*, 115460.

(155) Mark Weller, J.; K. Chan, C. Pyrochlore Nanocrystals as Versatile Quasi-Single-Source Precursors to Lithium Conducting Garnets. *J. Mater. Chem. A* **2020**, *8*, 17405–17410.

(156) Sacci, R. L.; McAuliffe, R. D.; Malkowski, T. F.; Kidder, N.; Chen, X. C.; Huq, A.; Kirkham, M.; Armstrong, B. L.; Daemen, L. L.; Veith, G. M. $La_2Zr_2O_7$ Nanoparticle-Mediated Synthesis of Porous Al-Doped $Li_7La_3Zr_2O_{12}$ Garnet. *Inorg. Chem.* **2021**, 10012.

APPENDIX A

SUPPORTING INFORMATION FOR CHAPTER 4

A.1. SUPPORTING TABLES

Table A1. Optimization study of various calcination conditions and additive used for sintering the LLZTO pellets prepared by MSS and SSR routes for attaining optimized relative density values.

Runs		Additive	Temperature (˚C)	Duration (h)	Relative density (%) of pellets		Phases
SSR-Pellets	MSS-Pellets				SSR	MSS	
S1	M1	None	1100	10	56	50	c-LLZTO
S2	M2	None	1100	16	61	55	c-LLZTO
S3	M3	None	1300	2	92	86	LZO
S4	M4	**None**	**1140**	**16**	**94**	80	**c-LLZTO**
S5	M5	None	1150	16	96	83	*LZO and c-LLZTO
-	**M6**	**None**	**1200**	**16**		**93**	**c-LLZTO**
S6	-	10wt%. LiOH+ 1wt.% γ-Al_2O_3	1140	16	70	-	c-LLZTO
S7	-	5wt%. LiOH+ 1wt.% γ-Al_2O_3	1140	16	75	-	c-LLZTO
-	M7	10wt%. LiOH+ 1wt.% γ-Al_2O_3	1200	16	-	73	c-LLZTO
-	M8	5wt%. LiOH+ 1wt.% γ-Al_2O_3	1200	16	-	76	c-LLZTO
S8	M9	1wt.% γ-Al_2O_3	1100	16	87	75	c-LLZTO
S9	M10	1wt.% γ-Al_2O_3	1140	16	90	80	c-LLZTO
S10	M11	1wt.% γ-Al_2O_3	1200	16	-	90	c-LLZTO^a

A.2. SUPPORTING FIGURES

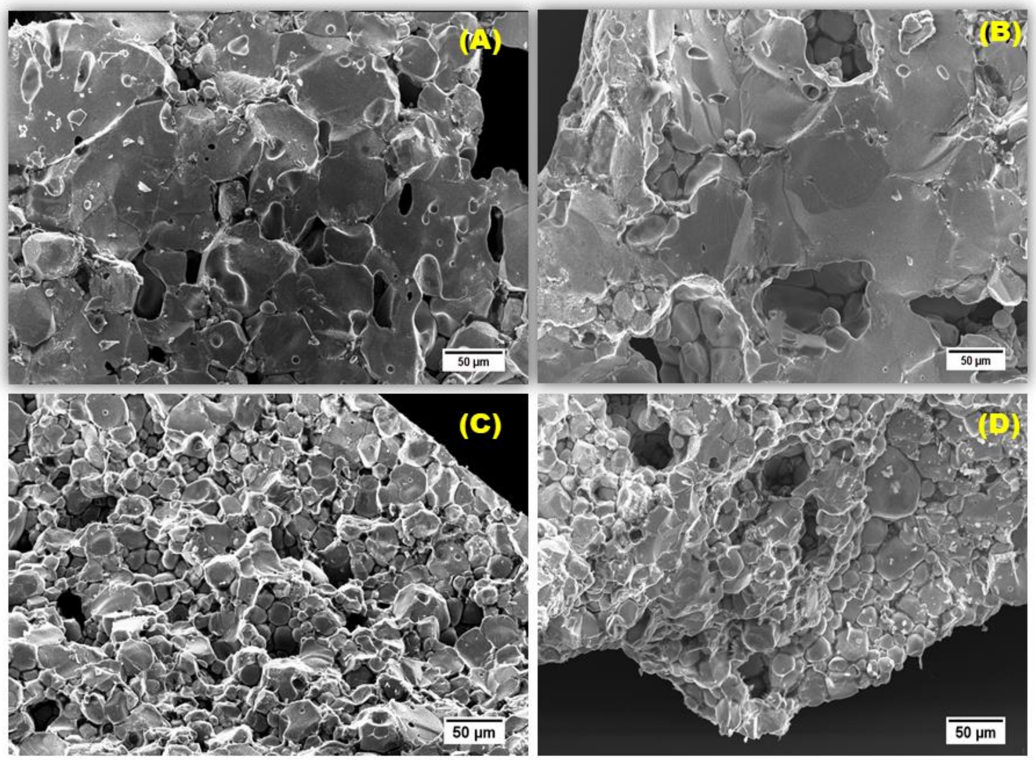

Figure A1. SEM images of the fractured SSR (A, B) and MSS (C, D) sintered pellets with 1wt.% γ-Al_2O_3 sintering additives along with additional 5 wt.% LiOH (A, C) and 10 wt.% LiOH (B, D).

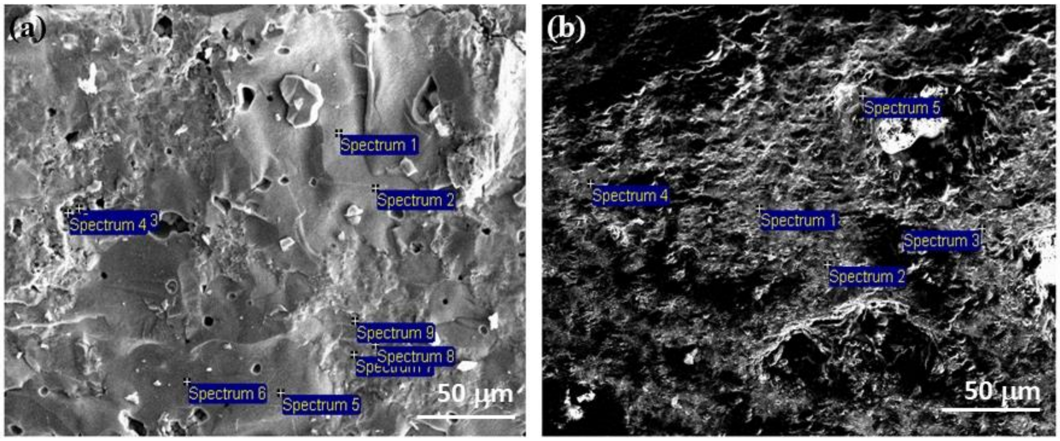

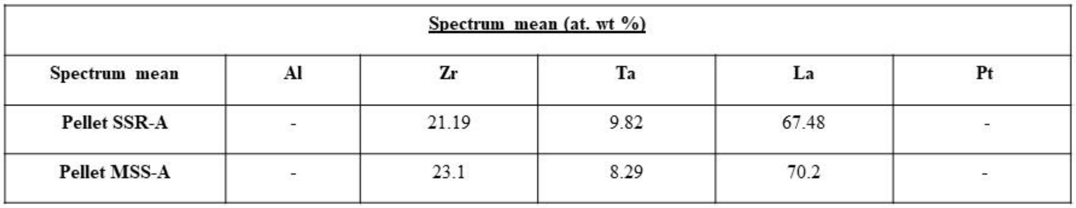

Spectrum mean (at. wt %)					
Spectrum mean	**Al**	**Zr**	**Ta**	**La**	**Pt**
Pellet SSR-A	-	21.19	9.82	67.48	-
Pellet MSS-A	-	23.1	8.29	70.2	-

Figure A2. EDX mapping for the LLZTO pellets sintered in Pt crucible, samples prepared by (a) the SSR route and (b) the MSS procedure.

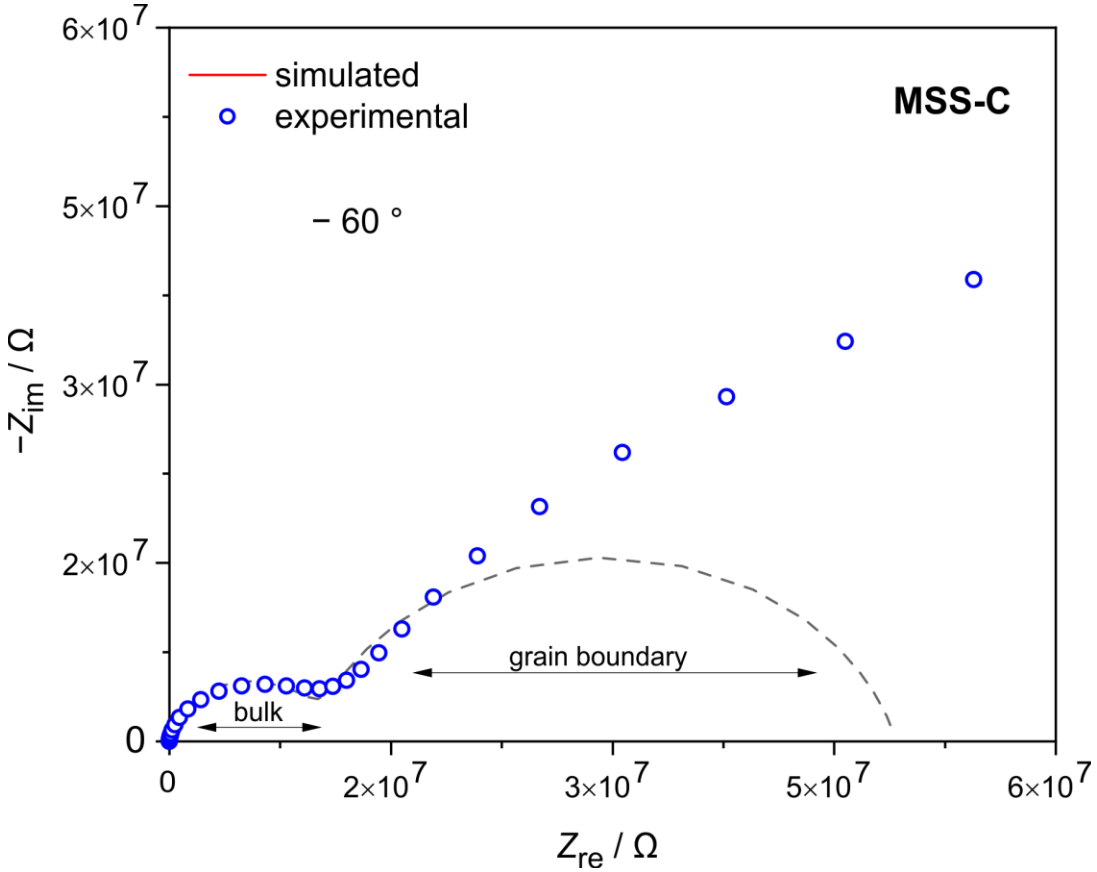

Figure A3. Impedance data recorded at − 60 ^{o}C for the MSS-C pellet (LLZTO with 1 wt. % Al_2O_3 additive, sintered in alumina crucible).

8/1/2021 Rightslink® by Copyright Clearance Center

Highly Conductive Garnet-Type Electrolytes: Access to Li6.5La3Zr1.5Ta0.5O12 Prepared by Molten Salt and Solid-State Methods

Author: Pavan Badami, J. Mark Weller, Abdul Wahab, et al

Publication: Applied Materials

Publisher: American Chemical Society

Date: Oct 1, 2020

Copyright © 2020, American Chemical Society

PERMISSION/LICENSE IS GRANTED FOR YOUR ORDER AT NO CHARGE

This type of permission/license, instead of the standard Terms and Conditions, is sent to you because no fee is being charged for your order. Please note the following:

- Permission is granted for your request in both print and electronic formats, and translations.
- If figures and/or tables were requested, they may be adapted or used in part.
- Please print this page for your records and send a copy of it to your publisher/graduate school.
- Appropriate credit for the requested material should be given as follows: "Reprinted (adapted) with permission from {COMPLETE REFERENCE CITATION}. Copyright {YEAR} American Chemical Society." Insert appropriate information in place of the capitalized words.
- One-time permission is granted only for the use specified in your RightsLink request. No additional uses are granted (such as derivative works or other editions). For any uses, please submit a new request.

If credit is given to another source for the material you requested from RightsLink, permission must be obtained from that source.

Contents in **Chapter** 4 is partially/completely reprinted (adapted) with permission from

Badami, P.; Weller, J. M.; Wahab, A.; Redhammer, G.; Ladenstein, L.; Rettenwander, D.; Wilkening, M.; Chan, C. K.; Kannan, A. N. M. Highly Conductive Garnet-Type Electrolytes: Access to Li6.5La3Zr1.5Ta0.5O12 Prepared by Molten Salt and Solid-State Methods. *ACS Appl. Mater. Interfaces* **2020**, *12* (43), 48580–48590. https://doi.org/10.1021/acsami.0c14056.

Copyright 2020, American Chemical Society

APPENDIX B

SUPPORTING INFORMATION FOR CHAPTER 5

B.1 EXPERIMENTAL

Calculation and Other synthesis details to prepare Al-LLZO and Ga-LLZO using solution-combustion route.

For preparing Al-LLZO precursor solution, stoichiometric amounts of the (Li, La, Al) nitrate and Zr-oxynitrate in a molar ratio ~ 6.6 (5-10 % excess Li by moles): 3: 0.24: 2 were dissolved in DI-water (amount of water required to dissolve nitrate precursor is tabulated in **Table B1**) and held under constant stirring at 80 °C until clear solution is observed. The molecular weight of ZrO (NO_3) was considered 285.23 g/mol based on hydration of the level of the precursor (~ 3 H_2O). Later, for preparing carbohydrazide (CH_6N_4O) fuel solution, amount of fuel required was determined based the combustion index of the individual precursor elements established by Jain *et al*[126]. The combustion index is defined as a measure of the tendency of an element for combustion, which is same as its valence state. Reducing (+) and oxidizing (-) valences of the elements were used as follows to evaluate combustion index of the precursors and fuel used during the synthesis as listed below.

Reducing elements	Li, (+1), C (+4), H (+1), Al (+3), Ga (+3), La (+3), Zr (+4)
Oxidizing elements	O (-2), N (0)

Table B1. Combustion index of the precursors and fuel based on its valence state.

Precursors	**Combustion index**
6.6 {$LiNO_3$} = 6.6 (1+ 0 + 3 x (-2))	-32.5
3 {La $(NO_3)_3 \cdot 6H_2O$}	-45
2 {ZrO $(NO_3)_2 \cdot 3H_2O$}	-20
0.24 {Al $(NO_3)_3 \cdot 9H_2O$}	-3.6
m * CH_6N_4O	8

A representative calculation to arrive at Fuel to Oxidizer ratio

$$\textbf{\textit{Oxidizers}}\ \{(Li_{6.5}Al_{0.24}La_3Zr_2O_{12})\} + \textbf{\textit{Fuel}}\ \{\mathbf{m}^* (CH_6N_4O)\} = 0$$

Required **m moles** of carbohydrazide under stoichiometric condition (*i.e.* F/O =1) is calculated by balancing combustion index. From the above equation (1) we arrive at 0.079 moles of fuel. Typical amounts of fuel (at F/O value = 4) and precursors amounts required to synthesize for example 3 g of Al-LLZO powders are listed in **Table S2.** Based on the fuel/oxidizer ratio, amount of fuel is dissolved in minimum amount of DI water held at 80 °C with constant stirring until clear solution was observed. Later, nitrate precursor solution and fuel solution are mixed and held at 80 °C under constant stirring for about 10 mins until gel is formed. Borax beaker (100 ml) containing dehydrated gel is introduced in a preheated muffle furnace **(placed inside the fume hood, away from flammable chemicals)** held at 500 °C with furnace door was intentionally kept partially open (to prevent buildup of gases during the combustion reaction which occurs under < 3 mins). Post-combustion of the gel, as combusted powders were taken out and later crushed using an agate mortar and calcinated further using MgO crucible with closed lids between (600-900°C) for 4 h with ramp rate 5 °C/ min.

Table B2. Tabulated amounts of precursor and DI-water required to dissolve precursors and fuel to prepare for example 3 g of Al-LLZO powders at F/O- 4.

Precursors	Amounts (g)	Amount of DI water (ml)
$LiNO_3$	0.6	1.0
$La(NO_3)_3 \cdot 6H_2O$	1.6	1.02
$ZrO(NO_3)_2 \cdot 3H_2O$	0.70	10
$Al(NO_3)_3 \cdot 9H_2O$	0.117	0.2
CH_6N_4O	0.44	2

B.2. SUPPORTING TABLES

Table B3. Effects of fuel to oxidizer ratios on nature of combustion and phase purity of Al- LLZO on calcining at 900 °C, 4 h.

F/O ratio	Combustion nature	Phases
0.5	sluggish	c-LLZO**,** $Li_{0.5}La_2Al_{0.5}O_4$
1	flame	c-LLZO, $Li_{0.5}La_2Al_{0.5}O_4$
2	smolder	c-LLZO, $Li_{0.5}La_2Al_{0.5}O_4$
4	smolder	c-LLZO

Table B4. Summary of phases and lattice constant of Al-LLZO calcined at various temperatures set to F/O = 4.

Calcination temperatures (°C), 4h	Phases	Lattice constant (Å)
600	c-LLZO, $La_2Li_{0.5}O_4$	13.087
700	c-LLZO, $La_2Li_{0.5}O_4$	13.046
800	c-LLZO	12.98
900	c-LLZO	12.97

Table B5. ICP-OES analysis of cubic Al-LLZO powder calcined at 800 °C / 4h and pellet sintered 1100 °C / 6 h.

	Elements	Al-LLZO powder	Al-LLZO Pellet
Mass % (MV ± SD; n=3)	Al	0.59 ± 0.03	0.59 ± 0.02
	La	39.9 ± 0.7	43.4 ± 0.7
	Li	4.51 ± 0.03	4.68 ± 0.05
	Zr	18.0 ± 0.3	19.7 ± 0.3
Atomic ratio (MV ± SD; n=3)	Al/Zr	0.11 ± 0.006	0.101 ± 0.003
	Li/Zr	3.29 ± 0.005	3.12 ± 0.002
	La/Zr	1.453 ± 0.003	1.448 ± 0.004
Formula[1]		$\mathbf{Li_{6.58}\,Al_{0.22}\,La_{2.91}\,Zr_2O_{12.0}}$	$\mathbf{Li_{6.24}\,Al_{0.20}\,La_{2.89}Zr_2O_{11.8}}$

B.3. SUPPORTING FIGURES

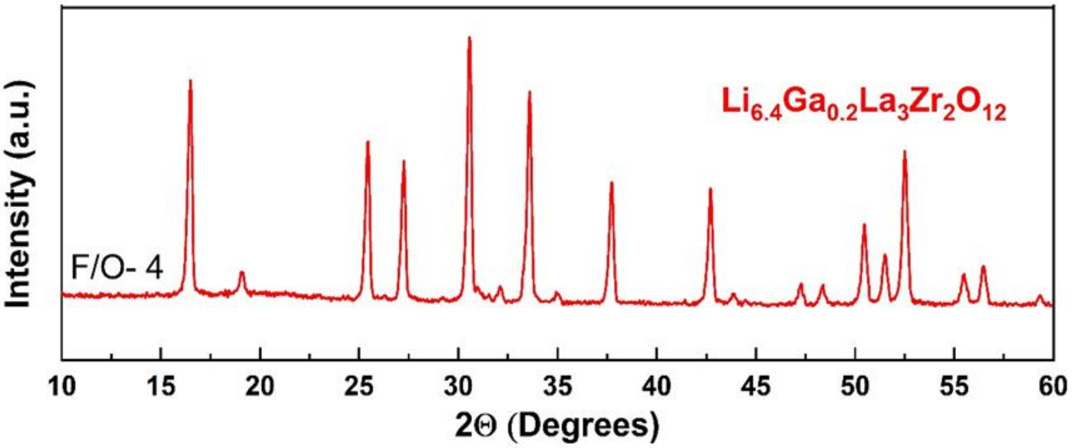

Figure B1. XRD powder patterns of Ga-doped LLZO prepared using solution combustion method on calcining as-synthesized powders at 800 °C for 4 h showing reflexes of cubic phase LLZO matched to reference pattern (ICSD data base-422259).

Figure B2. Transformation of gel to foamy powders on introducing into a preheated furnace held at 500 °C.

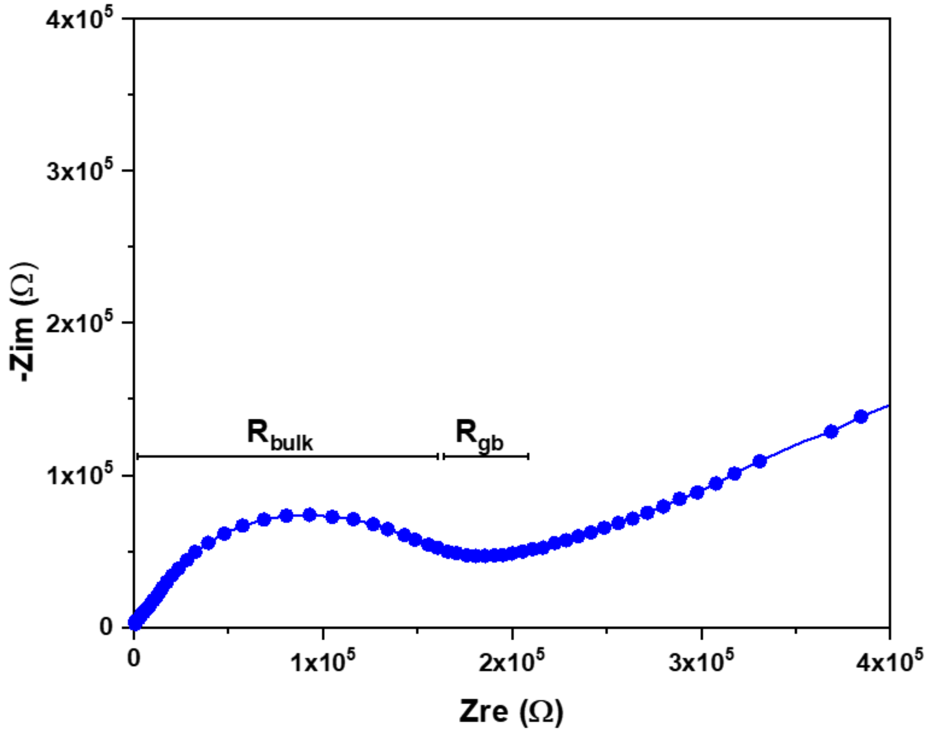

Figure B3. Nyquist plot of pellet sintered at 900 °C / 6 h representing high bulk and grain boundary resistance caused due to poor densification.

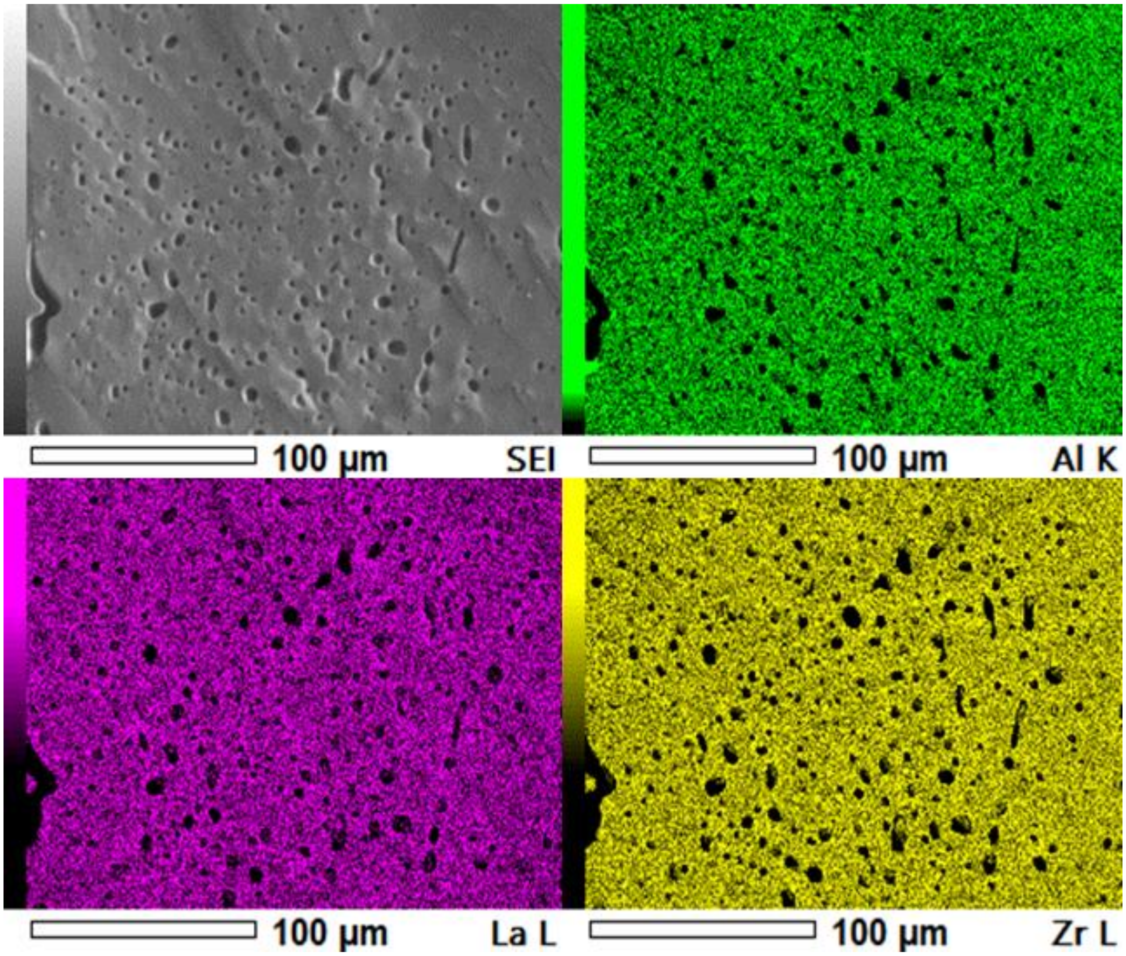

Figure B4. EDS spectral imaging of pellet sintered at 1100 ºC for 6 h showing uniform distribution of Al, La, Zr across the grain boundaries.

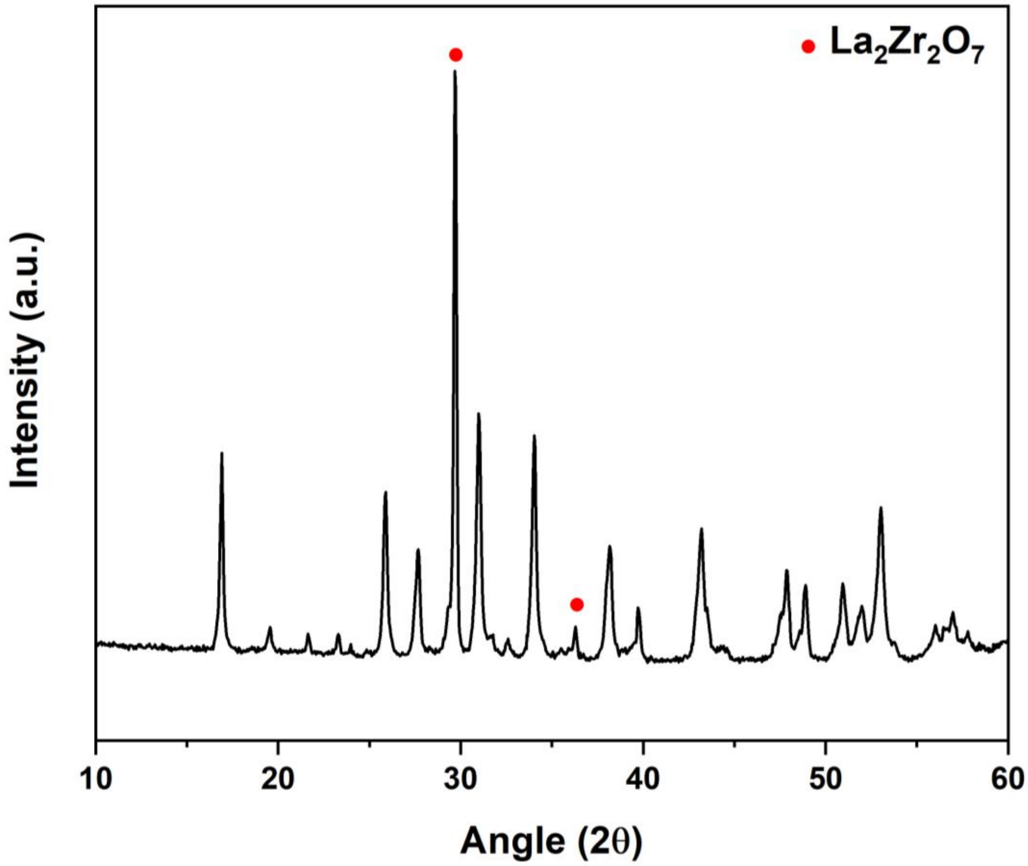

Figure B5. X-ray diffraction scan of Al-LLZO pellet sintered at 1200 °C / 6 h representing formation secondary $La_2Zr_2O_7$: (PDF card number # 00-017-0450) due to Li_2O volatilization during sintering

Contents in **Chapter** 5 is partially/completely reprinted (adapted) with permission from

Pavan Badami; Stefan Smetaczek; Andreas Limbeck; Daniel Rettenwander; K. Chan, C.; Mada Kannan, A. N. Facile Synthesis of Al-Stabilized Lithium Garnets by a Solution-Combustion Technique for All Solid-State Batteries. *Mater. Adv.* **2021**. https://doi.org/10.1039/D1MA00393C- Published by The Royal Society of Chemistry.

APPENDIX C

LIST OF PEER REVIEWED PUBLICATIONS DURING PH.D. PROGRAM

2020

Badami, P.; Weller, J. M.; Wahab, A.; Redhammer, G.; Ladenstein, L.; Rettenwander, D.; Wilkening, M.; Chan, C. K.; Kannan, A. N. M. Highly Conductive Garnet-Type Electrolytes: Access to Li6.5La3Zr1.5Ta0.5O12 Prepared by Molten Salt and Solid-State Methods. *ACS Appl. Mater. Interfaces* **2020**, *12* (43), 48580–48590. https://doi.org/10.1021/acsami.0c14056.

2021

Redhammer, G. J.; Badami, P.; Meven, M.; Ganschow, S.; Berendts, S.; Tippelt, G.; Rettenwander, D. Wet-Environment-Induced Structural Alterations in Single- And Polycrystalline LLZTO Solid Electrolytes Studied by Diffraction Techniques. *ACS Appl. Mater. Interfaces* **2021**. https://doi.org/10.1021/acsami.0c16016.

Badami, P.; Smetaczek, S.; Limbeck, A.; Rettenwander, D.; Chan, C. K.; Kannan, A. N. M. Facile Synthesis of Al-Stabilized Lithium Garnets by a Solution-Combustion Technique for All Solid-State Batteries. *Mater. Adv.* **2021**. https://doi.org/10.1039/D1MA00393C.